Geophysical Journal International

Spatio-temporal Analysis of Seismic Anisotropy Associated with the Cook Strait and Kaikoura Earthquake Sequences in New Zealand

Journal:	*Geophysical Journal International*
Manuscript ID	Draft
Manuscript Type:	Research Paper
Date Submitted by the Author:	n/a
Complete List of Authors:	Graham, Kenny; Victoria University of Wellington Faculty of Science, Institute of Geophysics Savage, Martha; Victoria University of Wellington, Institute of Geophysics Arnold, Richard; Victoria University of Wellington Faculty of Science, School of Mathematics and Statistics Zal, Hubert; Victoria University of Wellington Faculty of Science, Institute of Geophysics Okada, Tomomi; Tohoku University Graduate School of Science Faculty of Science Iio, Yoshihisa; Kyoto University Disaster Prevention Research Institute, Disaster Prevention Research Institute Matsumoto, Satoshi; Kyushu University, Institute of Seismology and Volcanologh
Keywords:	Seismic anisotropy < SEISMOLOGY, Fractures, faults, and high strain deformation zones < TECTONOPHYSICS, Dynamics: gravity and tectonics < TECTONOPHYSICS, Continental tectonics: strike-slip and transform < TECTONOPHYSICS, Spatial analysis < GEOPHYSICAL METHODS

manuscript to be submitted to *Geophysical Journal International*

Spatio-temporal Analysis of Seismic Anisotropy Associated with the Cook Strait and Kaikōura Earthquake Sequences in New Zealand

Kenny M. Graham[1], Martha K. Savage[1], Richard Arnold[2], Hubert J. Zal[1], Tomomi Okada[3], Yoshihisa Iio[4], Satoshi Matsumoto[5]

[1]Institute of Geophysics, SGEES, VUW, New Zealand
[2]School of Mathematics and Statistics, VUW, New Zealand
[3]Graduate School of Science, Tohoku University, Sendai, Japan
[4]Disaster Prevention Research Institute, Kyoto University, Uji, Japan
[5]Faculty of Sciences, Kyushu University, Shimabara, Japan

Keywords

- Shear wave splitting
- Crustal seismic anisotropy
- Kaikōura and Cook Strait earthquake sequence
- Gravitational stress
- Maximum shear plane
- Structurally controlled anisotropy

Corresponding author: Kenny M. Graham, Kenny.Graham@vuw.ac.nz

Abstract

Large earthquakes can diminish and redistribute stress, which can change the stress field in the Earth's crust. Seismic anisotropy, measured through shear-wave splitting (SWS), is often considered to be an indicator of stress in the crust because the closure of cracks due to differential stress leads to waves polarized parallel to the cracks traveling faster than in the orthogonal direction. We examine spatial and temporal variations in SWS measurements and the V_p/V_s ratio associated with the 2013 Cook Strait (Seddon, Grassmere) and 2016 Kaikōura earthquakes in New Zealand. These earthquake sequences provide a unique dataset, where clusters of closely-spaced earthquakes occurred. We use an automatic, objective splitting analysis algorithm and automatic local S-phase pickers to expedite the processing and to minimize observer bias. We present SWS and V_p/V_s measurements for over 40,000 crustal earthquakes across 36 stations spanning close to $5\frac{1}{2}$ years between 2013 and 2018. We obtain a total of 102,260 (out of 398,169) high-quality measurements. We observe significant spatial variations in the fast polarization orientation, ϕ. The orientation of gravitational stresses is consistent with most of the observed anisotropy. However, multiple mechanisms (such as structural, tectonic stresses and gravitational stresses) may control some of the observed crustal anisotropy in the study area. Systematic analysis of SWS parameters and V_p/V_s ratio revealed that apparent temporal variations are caused by variation in earthquake path through spatially varying media.

1 Introduction

Stress in the Earth is an important factor in earthquake genesis. Earthquakes are caused by the sudden rupture of rocks along faults exposed to differential stress in the Earth's crust. Earthquakes occur when the accumulated shear stress exceeds the strength of faults or fractures in rock. Thus, crustal stresses are the immediate driving forces of earthquakes (Zoback & Zoback, 2002). A variety of techniques have been devised to measure crustal stresses. The most direct technique to determine crustal stresses is through strain measurements in boreholes, where both stress magnitudes and orientations can be determined. However, drilling boreholes to seismogenic depths is a difficult and expensive enterprise (Townend & Zoback, 2000; Zoback & Zoback, 2002). Another well-established method is the inversion of earthquake focal mechanisms to determine the stress orientations in the region where the earthquake occurred (Michael, 1984; Hardebeck & Michael, 2006; Arnold & Townend, 2007). Geodetic techniques such as using GNSS (Global Navigation Satellite System) and InSAR (Interferometric Synthetic Aperture Radar) measurements, which can be used to infer strain rates, can also be interpreted as changes in stress (Hardebeck & Michael, 2006; Hardebeck & Okada, 2018). In most regions, shear wave splitting (SWS) parameters can also serve to estimate the orientation of the principal horizontal stresses. Thus, stress orientations can be inferred from measuring crustal seismic anisotropy through SWS (Crampin, 1984; Savage et al., 2016; Cochran & Kroll, 2015) and changes in SWS parameters can also be interpreted as changes in the state of stress.

Seismic anisotropy is the dependence of seismic velocity on direction, as caused by the elastic properties of rocks. The estimation of the geometry and strength of seismic anisotropy is often measured through shear wave splitting (SWS). SWS is a phenomenon that is observed when shear waves propagating through an anisotropic medium split into two nearly perpendicular phases that travel with different velocities. In the crust anisotropy is often considered to be controlled by either stresses (stress induced anisotropy) or geological structures (structurally induced anisotropy) (Crampin, 1984; Babuska & Cara, 1991; Zinke, 2000; Boness & Zoback, 2006; Crampin et al., 2015; Savage et al., 2016)). In the case of stress induced anisotropy, we assume that cracks or micro cracks are randomly distributed. Differential stress will close cracks perpendicular to the maximum horizontal stress (S_{Hmax}), leaving open cracks only parallel to S_{Hmax}. In the case of structurally induced anisotropy, the fast wave is oriented parallel to structural fabric or the orientation of the residual features of paleostress (Savage, 1999; Cochran et al., 2006). SWS can be characterized by

two parameters, the fast orientation (ϕ) and the delay time (δt). ϕ is the bearing of the polarization of the faster wave (also referred to as fast orientations) and δt is the time lag between the two split waveforms. δt depends on both the degree of anisotropy and the path length through the anisotropic medium. Although early studies concluded that stress–induced crack alignment is the principal cause of crustal anisotropy (Crampin, 1984; Babuska & Cara, 1991), several recent SWS studies, close to and away from the vicinity of major faults, have concluded that other possible causes of crustal anisotropy exist (Zinke, 2000; Matcham et al., 2000; Balfour et al., 2005; Boness & Zoback, 2006). A consistent pattern where ϕ measurements in close proximity to faults show fault-parallel orientations and ϕ measurements further away from faults are parallel to the principal horizontal stress (orientations) has been reported around the San Andreas Fault of California, (Zinke, 2000; Boness & Zoback, 2006), Wellington region and Marlborough Fault System (MFS) of New Zealand (Gledhill, 1991; Audoine et al., 2000; Matcham et al., 2000; Balfour et al., 2005; Karalliyadda & Savage, 2013).

Several researchers have used SWS to measure spatial and temporal variations in seismic anisotropy. Miller & Savage (2001) observed changes in fast polarization orientations before and after an eruption at Mt. Ruapehu volcano, New Zealand. They interpreted this as a variation in principal stress orientation, which they related to an increase in stress related to magmatic intrusion or inflation. Roman et al. (2011) observed rotations of fast orientations that correlated with rotating fault plane solutions for earthquakes associated with volcanic activity at Soufrière Hills volcano in Montserrat. Bianco et al. (2006) observed variations in fast orientation and delay times before the 2001 eruption on Mt Etna. They observed delay times exhibiting a sudden decrease shortly before the start of the eruption and variations in the fast orientation five days before the onset of the eruption. Zheng et al. (2008) also studied the temporal variations of shear-save splitting in the aftershock region of 1999 Chichi Earthquake, Taiwan. They also observed a decrease in delay times shortly before the Chichi main shock and two Chiayi earthquakes.

The relation between the ratio of body-wave (P-wave and S-wave) velocities, V_p/V_s, fluid content and pore pressure are well established (e.g. Wadati & Oki, 1933; Nur, 1971; Ito et al., 1979; Dvorkin et al., 1999, and references therein). The V_p/V_s ratio is one of the best parameters to indirectly identify fluid and crack migration within the crust, since pore fluid properties produce variations in seismic velocities (Dvorkin et al., 1999). In fluid-saturated rocks, high V_p/V_s anomalies may indicate high pore pressure (e.g. Dvorkin et al., 1999; Nur,

1971). Variations in the V_p/V_s ratio have been interpreted qualitatively by several studies to be related to the movement of fluids in the crust. Li & Vidale (2001) observed an increase in shear velocity of the fault zone rock around Johnson Valley, after the 1992 M_w7.5 Landers, California, earthquake (from 1994 to 1998). They interpreted the trend as an indication of fault healing by strengthening after the mainshock, which is most likely due to the closure of cracks that opened during the 1992 earthquake. They also observed that the fault-zone strength recovery is consistent with a decrease in the apparent crack density within the fault zone. Moreover, they observed a decrease in the ratio of travel time for P to S waves, which they explained as cracks near the fault zone being partially fluid-filled and becoming more fluid saturated with time (Li & Vidale, 2001). Chiarabba et al. (2009), using S- and P-wave arrival times, observed an increase in V_p/V_s before the M_w5.3 1997 Umbria-Marche earthquake in central Italy and attributed the trend to a pore-pressure increase in fluid-filled cracks in the volume around the fault. The combination of variations in seismic anisotropy, V_p/V_s ratio and geodetic data has been reported by recent studies in volcanic areas and slow-slip region (Savage et al., 2010b; Unglert et al., 2011; Zal et al., 2020).

Around the Wellington region of New Zealand, Gledhill (1991) and Matcham et al. (2000) used local earthquakes to study the anisotropic structure. Audoine et al. (2000) also characterized the crustal anisotropy around the transition between the subduction and the oblique transform faulting boundaries. In central MFS, they observed that fast polarization orientations were subparallel to the major faults and geological features, and attributed the observation to the presence of metamorphosed schist beneath the MFS. At the eastern edges of the MFS, they observed that fast orientations were parallel to the orientation of the maximum horizontal compressive stress, S_{Hmax} which is consistent with crack induced anisotropy in the crust. In the North Island, their fast polarization orientations were parallel to the strike of the Hikurangi subduction zone as well as to the major geological features (Audoine et al., 2000). Balfour et al. (2005) described the upper plate stress regime above the Southern end of the Hikurangi subduction zone, where the dextral MFS accommodates more than 80% of the relative plate motion (Townend et al., 2012). They examined the relationship between the S_{Hmax} orientations and the average fast orientations, and concluded that both stress and structural anisotropy exist around the MFS, but the dominant structural fabric of the MFS controls the seismic anisotropy measurement rather than S_{Hmax} (Balfour et al., 2005). Regional stress studies by Townend et al. (2012) and Balfour et al. (2005) around the study area revealed a uniform S_{Hmax} of 115°±16° upper-plate extend-

ing across the northern South Island. Recently, Evanzia et al. (2017) tried to distinguish between stresses around Southern Hikurangi Margin, New Zealand, using SWS and focal mechanism measurements. They suggested that stresses in the overriding plate are likely related to bending stresses, gravitational stresses, and tectonic loading.

In this study we perform a systematic analysis of SWS parameters to investigate the physical mechanisms causing crustal anisotropy around the Marlborough and Wellington region, and to explore possible temporal variations in SWS measurements. The 2013 Cook Strait and 2016 Kaikōura earthquake sequences provide a rare dataset, where clusters of closely-spaced earthquakes with full azimuthal coverage occurred. We use this dataset to examine the hypotheses of structure and stress induced anisotropy that are often used to explain anisotropy in the crust. The stress–induced hypothesis suggests that cracks aligned with the maximum horizontal compressive stress direction, S_{Hmax}, remain open with a preferred orientation (Crampin & Booth, 1989; Savage, 1999) and thus induce anisotropy. The stresses acting on crustal tectonic settings can be characterized into two categories; (i) topographical stresses acting on the shallow crust (often referred to as gravitational stresses) and (ii) stresses driven by the relative plate motions or geodynamic processes (referred as tectonic stresses). Often, crustal anisotropy studies use S_{Hmax} from focal mechanism inversions to explain the stress hypothesis with little focus on S_{Hmax} from gravitational stresses. Araragi et al. (2015) and Illsley-Kemp et al. (2017) are two of the few studies that suggested gravitational stress as a possible explanation for crustal seismic anisotropy around Mt. Fuji (Japan) and the Northern Afar region (East Africa) respectively. In theory, the orientation of gravitationally induced horizontal stresses, $S^{Grav}_{H_{max}}$, have different orientations at the peak of the mountains, as opposed to the slope. At the peak $S^{Grav}_{H_{max}}$ is parallel to the strike of the mountain ridge, where as, at the slope it is perpendicular (Flesch et al., 2001; Hirschberg et al., 2018). In basins of two mountains ridges, the expected $S^{Grav}_{H_{max}}$ are often perpendicular to the strike of the ridges due to the compressional stresses on the slopes on either side of the basin (Hirschberg et al., 2018). Here, we examine how well both stresses explain the crustal anisotropy in central New Zealand (southern North Island and northwestern south island; see Figure 1) by comparing the splitting measurements with S_{Hmax} from both gravitational stresses and tectonic stress (stresses at depth from focal mechanism inversion).

The structural-control hypothesis suggests that the orientation of the anisotropic medium is associated with the orientation of the geological structures (such as fault orientations,

shear planes sub–parallel to faults) (Zinke, 2000; Boness & Zoback, 2006; Cochran et al., 2006; Okaya et al., 2016). Mineral alignment, associated with shearing in fault zones, or foliation in metamorphosed rocks has been one of the hypotheses used to explain structural-control anisotropy in the crust. Around central New Zealand, Audoine et al. (2000) attributed the observed anisotropy to the metamorphosed schist in the crust because recrystallization during metamorphism may form schistosity or a pervasive foliation. Okaya et al. (1995) also observed a high degree (up to 20 %) of anisotropy associated with the Haast Schist of the South Island, New Zealand. Okaya et al. (2016) explained the crustal anisotropy in the Taiwan collision zone by deformation–related (due to pervasive shearing in strike-slip fault zones) mineral preferred orientation in the metamorphic rocks (e.g. schist fabric). In this paper we examine these various hypotheses by comparing our splitting measurements with active fault orientations, orientations of horizontal principal stress (both tectonic and gravitational) and maximum shear plane orientations from the strain rate field (relation to crustal deformation).

2 Tectonic Setting and Seismicity

New Zealand's tectonic setting is characterized by two subduction systems of opposite polarity, connected by an area of oblique continental convergence (inset in Figure 1). Westward subduction (and intra-arc rifting) in the North Island at the Hikurangi subduction zone changes to strike-slip at the Marlborough Fault Zone, transpressional collision along the Alpine Fault and finally back to (eastward) subduction at the Puysegur Trench (inset in Figure 1) offshore (Mortimer, 2004).

The study area (red box on inset in Figure 1), central New Zealand, covers the southern end of the Hikurangi subduction zone and the north eastern part of New Zealand's South Island, which is dominated by the MFS. The MFS marks the transition from a subduction plate boundary in the north to a transpressive plate boundary (the Alpine Fault) in the south. The faults in the MFS are predominantly strike-slip (trending NE-SW parallel to the strike of the Pacific-Australia plate motion), with a relatively small component of reverse motion (Van Dissen & Yeats, 1991). The average regional strike of the faults is 55° and their near-surface dips vary from 60° to near-vertical (Van Dissen & Yeats, 1991; Anderson et al., 1993). Major geological structures around the southern end of the Hikurangi subduction zone strike in the NE-SW direction with active faulting also following this NE-SW trend (Mortimer, 2004; Litchfield et al., 2017). Southwest from Kaikōura lies the North Can-

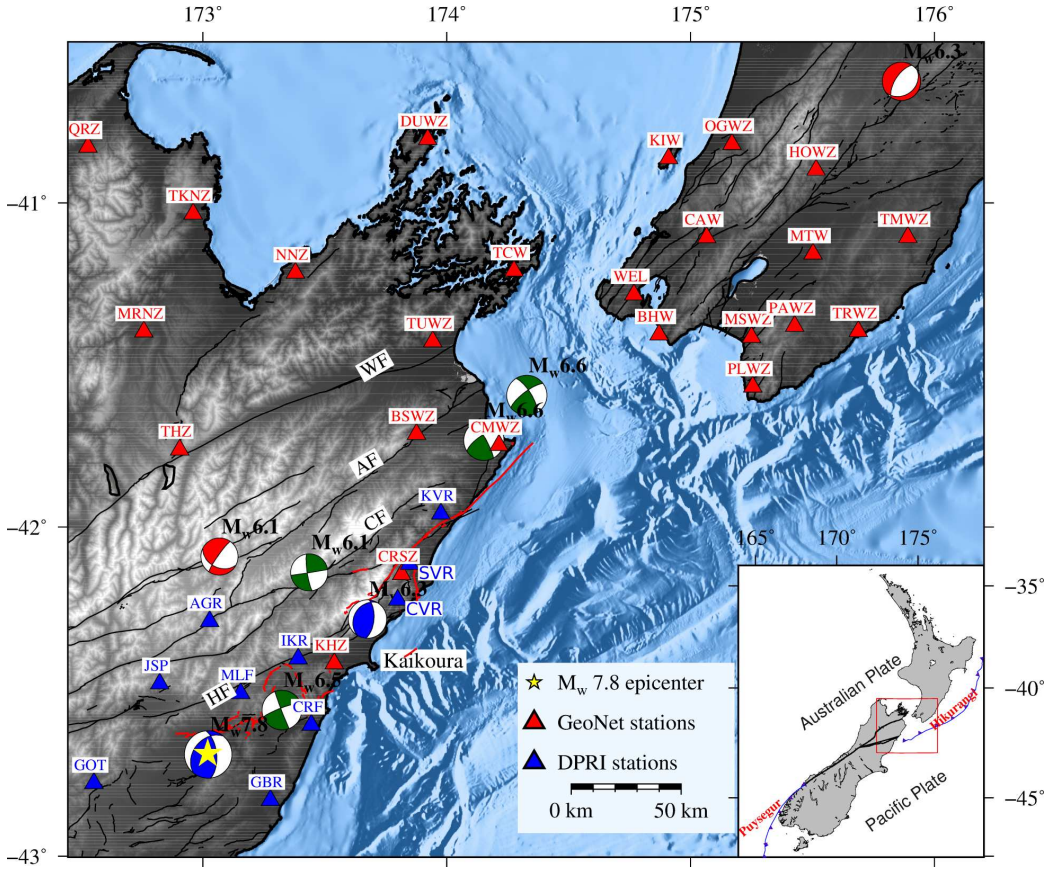

Figure 1. Map showing the tectonic setting of the study area with the stations used (red and blue triangles) plotted on a basemap of the digital topography and bathymetry (Mitchell et al., 2012). GeoNet CMT solutions of $M_w > 6$ earthquakes from 2013 to 2018 are shown; blue focal mechanism plots (beach balls) represent reverse mechanisms, with the red representing normal faulting with some dip slip motion, and green represents a strike-slip mechanism. Major faults marked include the Wairau (WF), Awatere (AF), Clarence (CF) and Hope (HF) faults. The red lines denote the surface rupture of faults during Kaikōura mainshock (Langridge et al., 2016). The yellow star indicates the epicenter of the M_w7.8 Kaikōura earthquake. Inset: The study region (red frame): the blue line is the plate boundary fault showing the Hikurangi and Puysegur trenches.

terbury fold and thrust belt (Reyners & Cowan, 1993; Pettinga et al., 2001). The NE-SW trend of the thrust fault extends through the northeastern part of the Canterbury region. In response to the transition from the subduction related tectonics in the north, thrust faults are evolving (Pettinga et al., 2001). The thrust faults are expressed as topographical ridges with NE-SW strike extending close to the Hope fault (Reyners & Cowan, 1993; Pettinga et al., 2001). Nearly two-thirds of the Marlborough region is underlain by greywacke of the Torlesse Supergroup, a laterally uniform wave-speed structure (Reyners & Cowan, 1993; Mortimer, 2004). The Marlborough Schist found north of the Wairau fault, which is part

of the Haast Schist of South Island, is commonly considered to be strongly metamorphosed (Mortimer, 1993).

The 2013 Cook Strait earthquake sequence started in July 2013 with two foreshocks of M_w 5.7 and M_w 5.8 and climaxed in the July, 21^{st} 2013, M_w 6.5 Seddon earthquake and the August, 16^{th} 2013, M_w 6.6 Lake Grassmere earthquake (Figure 1). These large earthquakes, located ∼50 km south of Wellington, New Zealand's capital, generated significant ground shaking in the Wellington and Marlborough regions (Holden et al., 2013; Hamling et al., 2014). Both earthquakes were strike-slip events with similar magnitudes and characteristics and they were considered to be a 'doublet' (Holden et al., 2013). The seismicity in the Cook Strait sequence region is still above the background levels that existed prior to 2013, with more than 16,000 earthquakes ($M_L \geq 1$) within a 4 year period from January, 2013 to November, 2017 (Holden et al., 2013; GeoNet, 2019, accessed February 2, 2019). Seismicity in Marlborough (before the 2016 Kaikōura earthquake) was mainly concentrated in the region above the subduction interface and around the north-eastern part of the MFS (Holden et al., 2013). The area was the location of a swarm of $M > 4$ earthquakes in 2005 and before that, it was the location to the 1977 M 6 Cape Campbell earthquake and the 1966 M 5.8 Seddon earthquake (Holden et al., 2013).

The M_w 7.8, 14 November 2016, Kaikōura earthquake, is the largest and most complex earthquake recorded on land in New Zealand (Clark et al., 2017; Hamling et al., 2017). The earthquake initiated near the North Canterbury region at a depth of 15 km with an oblique thrust faulting mechanism (Hamling et al., 2017, Figure 1). The rupture propagated from South-West towards the North-East for about 120 s, with an unusual source process, starting with weak radiation and releasing more energy while propagating towards the North-East over a distance of ∼150 km and terminating offshore in the Cook Strait region (Duputel & Rivera, 2017; Holden et al., 2017; Hamling et al., 2017; Cesca et al., 2017). A remarkable number (> 20) of shallow crustal fault segments (involving a combination of reverse and dextral strike-slip faulting; Figure 1) ruptured, including vertical motions of more than 10 m and horizontal displacements over 11 m (Clark et al., 2017; Hamling et al., 2017; Cesca et al., 2017). Most of the faults that ruptured have a general NE-SW trend (red lines in Figure 1), but some have NW-SE orientation, revealing a complex and heterogeneous slip pattern (Clark et al., 2017; Hamling et al., 2017; Kaiser et al., 2017). Surface rupture was mostly associated with known onshore faults. However, some surface traces were produced by faults that had not been previously mapped. Also some faults ruptured offshore, causing

a small tsunami (Clark et al., 2017; Wallace et al., 2017). The 2016 Kaikōura earthquake was followed by more than 25,000 local and regional aftershocks (GeoNet catalogue), clustered in three unique spatial patterns (Kaiser et al., 2017). More than 100,000 landslides were triggered by the earthquake and subsequent aftershocks, with 50 of them yielding significant landslide dams (Litchfield et al., 2017; Dellow et al., 2017). Another unusual aspect of the Kaikōura earthquake was the occurrence of large-scale (>15,000 km^2) slow slip events triggered on the central and northern Hikurangi subduction interface (250 and 600 km away from the epicenter respectively) due to dynamic-stress changes from passing seismic waves (Wallace et al., 2017).

3 Data and Methodology

3.1 Data

We determine SWS measurements for over 40,000 local crustal earthquakes that were located around the region of the 2013 Cook Strait earthquake sequence (Figure 2). Our earthquake catalog consists of GeoNet detection and locations (Petersen et al., 2011) and spans more than 5 years: from January 2013 to June 2018. Although Lanza et al. (2019) relocated some of the events used here, we used the GeoNet catalog to ensure continuity. The GeoNet catalog used here has a good azimuthal coverage of events before and after the 2016 Kaikōura main-shock (see supplementary Figure S1). This enables us to search for temporal variations in SWS parameters and V_p/V_s ratios.

We use 36 stations deployed around the Wellington and Marlborough region. These stations include 24 permanent seismic stations (combination of broadband and short period instruments; red triangles on Figure 1) operated by GeoNet (the Geological hazard information for New Zealand) and 12 temporary short-period stations installed and operated by DPRI (Disaster Prevention Research Institute, Kyoto University, Japan) (Okada et al., 2019) at different time periods between 2009 and 2018 (blue triangles on Figure 1). Plots of data continuity for all stations are shown in supplementary Figure S2. All the stations were sampled with a common sampling frequency of 100 Hz. Since the objective was to study crustal anisotropy, the hypocentral depths were limited to less than 35 km to include only earthquakes whose ray paths travel wholly through the crust. Moreover, we limited events magnitudes to M_w 1.5 and above to remove any poor-quality waveforms.

manuscript to be submitted to *Geophysical Journal International*

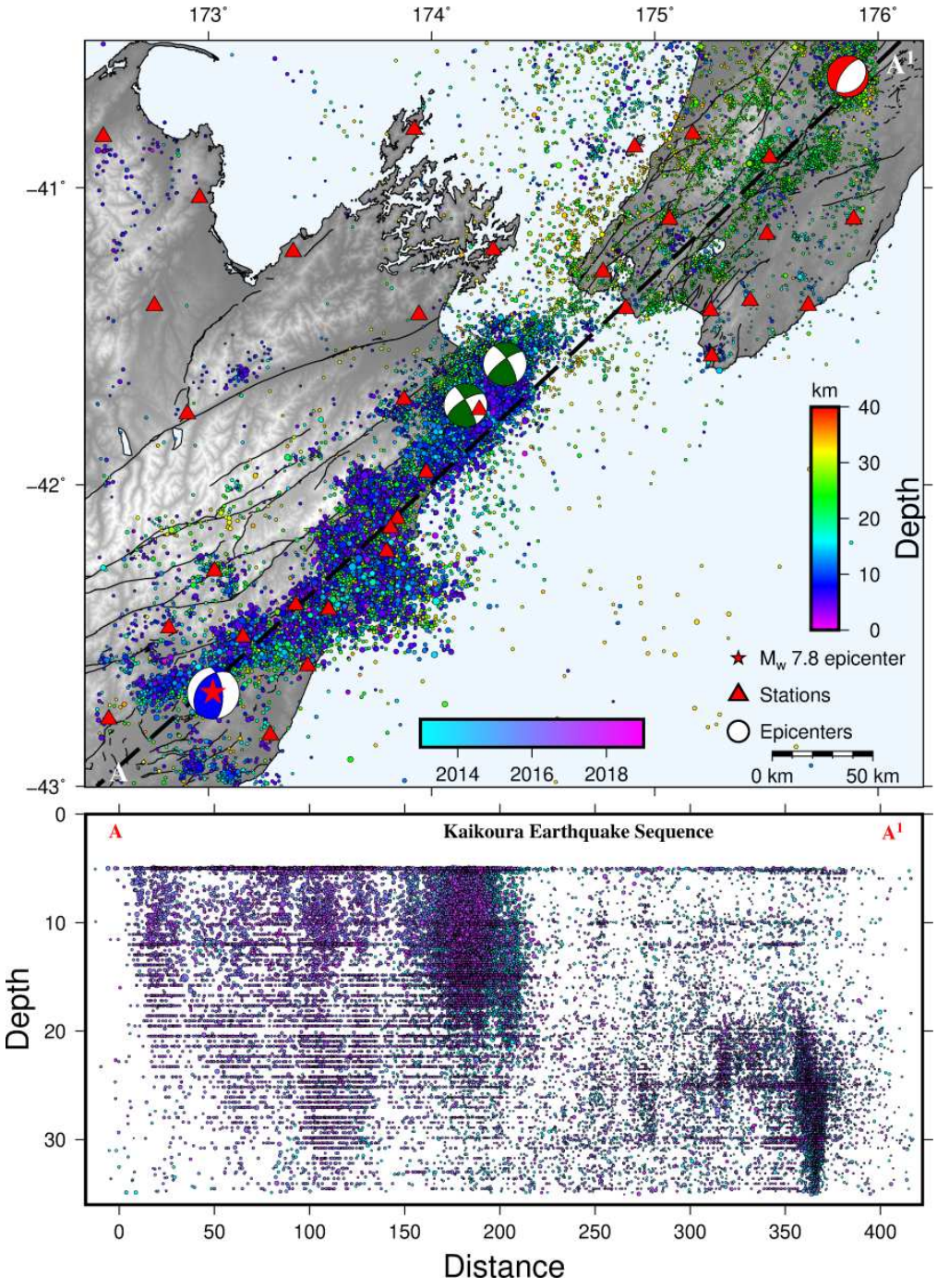

Figure 2. Map of earthquake epicenters used for analysis. Red triangles are the locations of GeoNet stations used. Events are colour-coded by the hypocentral depths. Blue focal mechanism solution (beach ball) represents the Kaikōura earthquake faulting mechanism; red beach ball represents the Eketahuna earthquake faulting mechanism, and green beach balls represent the two Cook Strait earthquake faulting mechanisms (Ristau, 2013). Focal mechanisms solutions were obtained from the GeoNet regional moment tensor solution catalog. A cross-section from A to A^1 shows the projected depth distributions, colored by time (time scale on main Figure).

3.2 Method

To estimate SWS parameters for thousands of waveforms, a fully automated and systematic technique was implemented. Here, we used the automatic splitting analysis code; Multiple Filter Automatic Splitting Technique, MFAST (Andreas, 2010; Savage et al., 2010a), which is designed to handle large volumes of data. MFAST is based on the eigenvalue-minimization method of Silver & Chan (1991) and the clustering method of Teanby et al. (2004a). MFAST uses an automated workflow to estimate the splitting parameters with an objective grading of measurements (Walsh et al., 2013). A concise description for MFAST is presented in Section 3.2.2 and a detailed description of the method is presented by (Savage et al., 2010a; Andreas, 2010; Walsh, 2012).

We used P-wave arrival times and origin times, t_o determined by GeoNet (Petersen et al., 2011). We used an automatic algorithm (Section 3.2.1) to estimate local shear wave arrival times for seismographs with good signal to noise ratio, SNR (SNR>3). All SWS measurements were made within the "shear wave window" (incidence angles less than a chosen critical angle, defined below). We used 1-D synthetic analysis (determining the effect of angle of incidence on splitting measurements) to resolve the ultimate critical angle for our analysis. This was necessary because, outside the shear wave window, the shear waveforms are susceptible to S to P conversions and scattering at the surface causing non-linear particle motion (Nuttli, 1961; Crampin & Gao, 2006; Savage et al., 2016). Neuberg & Pointer (2000) showed that waveforms outside the shear wave window generate elliptical particle motion even without the presence of anisotropy, especially when recording shallow local earthquakes in the vicinity of strong topography. We simulated waveforms in a 1-D anisotropic medium using the Levin & Park (1997) 1-D reflectivity code (which was subsequently modified by Castellazzi et al. (2015) and Walsh (2012)) and estimated the apparent splitting parameters using MFAST (Andreas, 2010; Savage et al., 2010a). Supplementary Figure S3 shows the 1-D model used for analysis. The effect of angle of incidence on splitting analysis was tested by varying angle of incidence with back azimuth. As shown in supplementary Figure S4, we observed a strong back azimuthal variation of δt and ϕ as angle of incidence is increased (here vertical incidence is 0°). At higher angle of incidence $> 30°$, we observe significant variations of splitting parameters with back azimuth. Since we observed less variations of splitting parameters with back azimuth at an incidence angle of 35° compared to higher incidence angle, we selected a maximum angle of 35° as the best shear wave window for our analysis. We estimated angles of incidence using the TauP toolkit (Crotwell et al., 1999)

and a 1D velocity model extracted from the Eberhart-Phillips & Fry (2018) 3-D velocity model.

3.2.1 Local phase arrival picking

Determination of S-wave arrival times is necessary to estimate SWS measurements. Due to the large volume of our data set, manually picking the S-phase arrival times would have been too time consuming. We therefore used two automatic picking techniques. First, local S-phase arrival times (S-picks) for GeoNet stations were automatically picked using the technique of Diehl et al. (2009) modified by Castellazzi et al. (2015), hereafter called Spicker. For stable and reliable S-wave picking, the Spicker technique combines three different detection and picking methods. The STA/LTA detector (e.g. Allen, 1978) and polarization detector (e.g. Flinn, 1965) are used to identify the first arriving S-phase. The information provided by the detectors is then used to set up the search windows of the autoregressive picker using the Akaike Information Criterion (AR-AIC) as outlined by Takanami & Kitagawa (1988). Finally, all three methods are combined to yield the best arrival-time of the first arriving S-phase and its corresponding uncertainty. The Spicker makes use of all the three component seismogram to estimate the S-phase arrival. See Diehl et al. (2009) and Castellazzi et al. (2015) for further details on the algorithm.

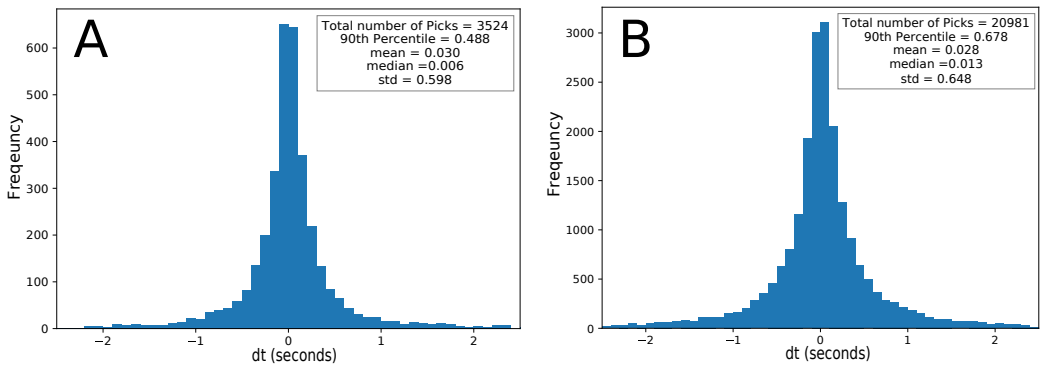

Figure 3. Distributions of local S-phase picking errors relative to analyst pick. A: Time difference between Spicker picks and manually picked S-phase arrival times. B: Time difference between GeoNet manual picks and Spicker picks.

We calibrated the picking algorithm with over 3,500 manually picked S-phases. These S-phases were randomly selected to obtain a uniform station, magnitude and depth distribution. The time difference between manual and Spicker picks revealed a symmetrical uni-modal distribution with a mean of 0.029 s and a standard deviation of 0.59 s. In addition, 90% percent of the Spicker picks were within ±0.484 of the manual S-picks (Figure 3A). This picking accuracy is adequate for our studies, because MFAST uses multiple windows for its analyses. The best parameters (Table S1) that yielded more picks and small time difference between manual and Spicker picks were used for the final picking. We compared the common S-picks (∼21,000) between GeoNet manual S-picks and Spicker picks across all stations. The time difference between GeoNet manual S-picks and Spicker picks revealed a symmetric unimodal distribution with mean 0.028, standard deviation 0.648 and 90% of the picks were within ±0.678 (Figure 3B). Over 200,000 S-phases were obtained, representing about 23% of the expected (event-station pair) arrivals. Moreover, to assess the quality of the S-picks across our dataset, we randomly selected approximately 5% of the S-picks across all stations. The selected events were manually inspected and approximately 15% of S-picks were unreliable and were either revised or discarded. Based on this analysis we estimate approximately 85% of the S-picks are reliable.

Some of components of the short period stations operated by DPRI were intermittently missing components. We could not apply the Spicker technique to estimate the S-phase arrival, since the technique required all three components for the estimation. Instead we used the Generalized Seismic Phase Detection, GPD, technique developed by Ross et al. (2018) for estimating phase arrivals for the DPRI stations. This technique trained a Convolutional Neural Network (a deep learning framework) to learn the features of seismic waveforms. An already trained model can be applied to waveforms that are not included in the training set, thus a trained model can be applied to different tectonic settings (Ross et al., 2018; Kong et al., 2018). We used the Ross et al. (2018) GPD-framework model which they trained and validated with a total of 4.5 million three-component waveforms across a range of magnitudes. With each component's time series, the model predicts the probability that a phase arrival is either a P or S arrival. We set the minimum probability for phase detection to 95%. An example of a pick example is shown in supplementary Figure S5. To gain confidence in the GDP picks, we estimated arrival times for events with GeoNet manual S-picks (more-than 40,000 picks across the 24 permanent GeoNet stations) and compared the time difference between the GDP S-picks and GeoNet manually S-picks. The

time difference shows a concentrated symmetric uni-modal distribution with mean -0.072 s, standard deviation 0.774 s and 90% percent of the picks were within ±0.261 s (See supplementary Figure S6).

3.2.2 Measuring splitting parameters

SWS parameters were estimated using the MFAST code (Andreas, 2010; Savage et al., 2010a). This procedure finds the inverse splitting operator that best removes the splitting. The waveforms are filtered with a series of band-pass filters, and the product of the bandwidth and the signal-to-noise ratio of the filtered waveform is used to determine the best three filters. Splitting measurements for all three filtered waveforms are estimated using the Silver & Chan (1991) and Teanby et al. (2004b) method with modification by (Walsh et al., 2013). The splitting parameters are estimated using the eigenvalue minimisation method repeated over multiple time windows around the S-phase. The splitting parameter pair (ϕ, δt) that best removes the splitting as measured by the smallest eigenvalue of the corrected covariance matrix, is chosen as the best measurement for the given time window (Savage et al., 2010a).

This procedure is then repeated for 75 windows covering slightly different time spans around the S-phase. The windows are automatically selected based on the dominant period around the filtered shear wave (Savage et al., 2010a). Cluster analysis over the 75 window measurements is used to select the final splitting parameter for the filter under consideration and to calculate the uncertainty associated with the measurements (Teanby et al., 2004a). Measurements are graded from A to D depending on the consistency between the (ϕ, δt) and measurements in the different windows. MFAST also provides a measure of the incoming polarization orientation (ϕ_{in}) by estimating the eigenvalues of the corrected components after splitting is removed (Silver & Chan, 1991; Savage et al., 2010a). ϕ_{in} corresponds to the polarization orientation of the shear wave before it enters the anisotropic layer responsible for the measured splitting parameters. As a quality control, we removed all null graded measurements (events for which no measurable splitting occurs or event for which ϕ is within 20° of parallel or perpendicular to ϕ_{in}) and also kept only A and B graded measurements. We also limited maximum delay times, δt to 0.4 s since local crustal events are often not expected to have larger delay times (Balfour et al., 2005; Cochran & Kroll, 2015). Following the quality control, a total of 102,260 (out of 398,169) high quality measurements were

obtained. Andreas (2010), Savage et al. (2010a) and Walsh et al. (2013) give a detailed description of the MFAST method.

We estimated V_p/V_s ratios along the ray path of each event that yielded high quality SWS measurements to each station using the approach of Wadati & Oki (1933) and Nur (1971). We assumed a linear ray path and that the V_p/V_s ratio is homogeneous along the seismic wave's path (Kisslinger & Engdahl, 1973). The V_p/V_s ratio of each event station pair was calculated using $V_p/V_s = (t_s - t_o)/(t_p - t_o)$, where t_s and t_p are the arrival times of the S and P waves, respectively and t_o is the event origin time (from the GeoNet catalog). Only V_p/V_s values between 1.5 and 2.3 were used because values outside of this range are not expected around the study region (Eberhart-Phillips & Fry, 2018) and would probably be due to inaccurate arrival time picks.

We also estimated the percent anisotropy, κ, following the approach of Babuska & Cara (1991) and Savage (1999). Here we define $\kappa = (v_{max} - v_{min})/\bar{v}$. Where v_{max} is velocity of the shear wave along the fast orientation v_{min} velocity of the shear wave along the slow orientation and $\bar{v}$ is an average of v_{max} and v_{min}. Assuming both fast and slow waves travel with the same path length, κ can be related to δt as: $\kappa = 200 * \delta t/(2t_s + \delta t)$. We use κ as well as δt, to characterize the anisotropy structure.

3.2.3 Spatial averaging

SWS measurements provide an estimate of the anisotropy along the ray propagation path between the source and station. However, it can be difficult to determine exactly where along the ray propagation path the anisotropy originates. With measurements from several stations and a dense cluster of events, one can probe the spatial variation of ϕ and δt using a spatial averaging technique. We used the TESSA (Tomography Estimate and Shear wave splitting Spatial Average) technique by Johnson et al. (2011) to estimate the spatial averages of ϕ.

For the spatial averaging technique, the study area is divided into cells or blocks using the recursive quadtree clustering algorithm described by Townend & Zoback (2001). We set the minimum block size to 5 km^2 and the minimum and maximum number of raypaths to be 20 and 80, respectively. The quad-tree gridding algorithm works in an iterative process. Cells with less than 20 rays passing through are not used for analysis and those with more than 80 rays passing through are subdivided until a minimum of block size of 5 km^2 or

until a minimum number of 20 events is attained. These criteria were chosen to ensure that each block contained enough data to give a reliable average measurement. To take into account variations due to heterogeneous anisotropic structure along the raypath (e.g. Johnson et al., 2011; Rümpker & Silver, 1998), rays in each grid cell are weighted by the inverse of the distance squared ($1/d^2$) (where d is the distance from the station to the grid cell in question). This weight scheme is used because we expect splitting to occur later in the ray-path and we did not observe a strong correlation between δt and hypocentral depth (Johnson et al., 2011). For comparisons with time, we used the regular gridding to ensure that the data points are always at the same locations. The spatial averages of ϕ are computed using a circular statistics approach (Berens, 2009) and are estimated only when the standard deviation of fast orientations in each grid is less than 30° and the standard error of the mean is less than 10°.

3.2.4 Quantitative comparison of ϕ measurements

We made quantitative comparisons of our spatially averaged ϕ measurement with GNSS derived principal contraction axes, average fault orientations, gravitational stress and focal mechanism inversion measurements. We also quantitatively compared averaged ϕ measurements between events before and after the 2016 Kaikōura earthquake to observe any spatio-temporal variation associated with the 2016 Kaikōura mainshock. For our quantitative comparison, we estimate a test statistic, F, the absolute value of the cosine of the difference between the two angles ($F = |\cos(\psi_1 - \psi_2)|$) where ψ_1 is the mean ϕ measurement and ψ_2 is the comparison angle. Since we do not have an identical set of locations at which mean ϕ has been estimated, we use locations that are closest together, and < 10 km to estimate the residual. Values of F range from 0 to 1, where 1 represents parallel orientation and 0 represents perpendicular orientation between ψ_1 and ψ_2. We contour the residual using the GMT functions grdsample and grdimage (Wessel et al., 2013). We also estimate the mean and median of the F to give an indication of how well the two angles are correlated.

3.2.5 Averaging for time variations

To examine variations we employed an averaging technique for values of δt to smooth and minimize the scatter as much as possible. We use a simple moving median as the smoothing function that reduces the noise in the measurement. We used a 20 day moving

median filter on the individual results with the aim of removing the scattered values from the data set. We estimate the 95% confidence intervals by using the non-parametric bootstrap approach. In this approach, we randomly sample with replacement from the original sample a dataset of the same size as the original sample. We repeat this for 1000 replicates and for each replicate dataset we estimate the median value. The 2.5th and 97.5th percentile of the replicate dataset is estimated as the respective lower and upper values of the 95% confidence interval for the median.

4 Results

We determined SWS measurements for more than 40,000 waveforms recorded on at least one of the 36 stations within the study region (Figure 1). Table 1 & 2 give a summary of fast orientations, delay times, percentage of anisotropy and V_p/V_s ratio as well as associated descriptive statistics for each station. Out of ∼102,000 high quality SWS parameters we estimated, the delay times vary between near zero to 0.372 s with an average of 0.157±0.001 s. The V_p/V_s ratio varies from 1.58 to 2.22 with an average of 1.741±0.001. Percent anisotropy varies from 0 to 5.186% with an average of 0.922±0.004%.

Rose diagrams of ϕ orientations recorded at each station, overlain on a basemap of the digital topography, are shown in Figure 4. S_{Hmax} orientations from Townend et al. (2012) and Balfour et al. (2005) are also shown as green bow-ties with wedges showing the 95% confidence interval. ϕ orientations for most of the stations show a dominant NE-SW orientation, which is parallel to the strike of the geological structures in the region. A few stations have NW-SE orientations.

Around the MFS, ϕ orientations are generally parallel to the strike of the active faults. The consistent trend suggests a relation between ϕ and the structural trend around the central and western MFS. Yet, some stations, KHZ, IKR, CRF and GBR, at the eastern coastal edge of the MFS yield NW-SE orientations of ϕ, which is perpendicular to the structural trend and sub-parallel to the crustal S_{Hmax} orientations. At station CMWZ and KVR, we observe a bi-modal distribution of ϕ orientations, with one subset sub-parallel to the S_{Hmax} orientation and the other subset sub-parallel to the strike of the faults. At stations BSWZ and TUWZ, ϕ orientations are sub-parallel to the orientation of the nearby Awatere and Wairau Faults respectively and perpendicular to the nearby S_{Hmax} orientation.

Table 1. Summary statistics of fast orientation (ϕ), delay time (δt), V_p/Vs ratio and percent anisotropy (% Aniso) with their 95% confidence interval for GeoNet permanent stations

Station	Events	Mean $\phi(^\circ)$	SD ϕ	Mean δt(s)	SD δt	Mean V_p/Vs	SD V_p/Vs	Mean %Aniso	%Aniso SD
BHW	3515	81.14 ±7.40	62.82	0.136±0.002	0.066	1.724±0.002	0.066	0.759±0.015	0.424
BSWZ	4781	52.82 ±1.76	43.38	0.181±0.002	0.076	1.743±0.002	0.084	1.453±0.023	0.801
CAW	6499	17.05 ±3.29	55.91	0.171±0.002	0.081	1.744±0.001	0.051	0.683±0.009	0.342
CMWZ	2162	-82.10±10.43	64.11	0.173±0.003	0.072	1.819±0.008	0.181	2.371±0.065	1.534
CRSZ	1588	67.47 ±4.07	48.34	0.168±0.004	0.085	1.808±0.014	0.281	2.118±0.060	1.167
DUWZ	2639	28.60 ±3.68	50.79	0.203±0.003	0.086	1.738±0.002	0.044	0.623±0.011	0.262
HOWZ	2015	69.93 ±6.58	57.45	0.139±0.003	0.075	1.732±0.002	0.045	0.673±0.019	0.419
KHZ	6343	-32.95±2.89	53.83	0.149±0.002	0.073	1.736±0.001	0.055	0.713±0.011	0.421
KIW	5497	53.85 ±3.11	53.87	0.152±0.002	0.073	1.718±0.001	0.044	0.629±0.008	0.296
MRNZ	2375	52.98 ±3.78	50.37	0.205±0.003	0.081	1.741±0.001	0.030	0.535±0.009	0.214
MSWZ	3481	60.46 ±2.02	43.02	0.142±0.003	0.077	1.784±0.002	0.058	0.560±0.011	0.327
MTW	7300	61.60 ±3.03	55.57	0.150±0.002	0.071	1.771±0.001	0.039	0.625±0.008	0.330
NNZ	1832	50.30 ±10.84	63.55	0.206±0.004	0.082	1.729±0.002	0.040	0.684±0.015	0.298
OGWZ	4232	37.96 ±1.16	34.13	0.123±0.002	0.067	1.736±0.001	0.047	0.478±0.009	0.282
PAWZ	1908	75.94 ±7.12	58.17	0.188±0.004	0.078	1.774±0.002	0.052	0.691±0.015	0.329
PLWZ	1460	-22.50±6.66	55.31	0.166±0.004	0.077	1.780±0.003	0.050	0.700±0.019	0.351
QRZ	1632	46.28 ±4.34	49.59	0.205±0.004	0.077	1.733±0.001	0.025	0.395±0.008	0.156
TCW	9199	14.07 ±2.03	51.22	0.133±0.001	0.069	1.715±0.001	0.054	0.643±0.008	0.362
THZ	2676	26.09 ±4.69	54.62	0.163±0.003	0.078	1.695±0.002	0.044	0.611±0.011	0.281
TKNZ	1798	86.31 ±3.14	44.95	0.226±0.003	0.065	1.735±0.002	0.034	0.543±0.008	0.165
TMWZ	809	22.97 ±19.73	65.95	0.110±0.005	0.064	1.787±0.002	0.030	0.567±0.025	0.334
TRWZ	629	42.11 ±5.33	45.03	0.189±0.006	0.074	1.789±0.006	0.069	0.786±0.033	0.400
TUWZ	4648	51.77 ±1.37	38.43	0.165±0.002	0.074	1.719±0.001	0.045	0.957±0.016	0.528
WEL	4144	-81.07±2.53	48.37	0.144±0.003	0.082	1.747±0.002	0.065	0.711±0.013	0.414
Total	83183	47.59±1.05	57.85	0.158±0.001	0.077	1.744±0.001	0.079	0.847±0.004	0.645

Only high quality measurements (described in Section 3.2.2) are presented in the summary table. ± represents the 95% confidence intervals. SD shows the standard deviation of the measurements. Station averages and standard deviation for fast orientations were performed using circular statistics. Event represents the number of event–station pair used for analysis. Total shows the summary of all stations for GeoNet stations.

Table 2. Summary statistics of Fast orientation (ϕ), delay time (δt), V_p/Vs ratio and percent anisotropy (% Aniso) with their 95% confidence interval for DPRI temporary stations.

Station	Events	Mean ϕ(°)	SD ϕ	Mean δt(s)	SD δt	Mean V_p/Vs	SD V_p/Vs	Mean %Aniso	%Aniso SD
AGR	277	44.78 ±11.59	51.11	0.167±0.012	0.096	1.648±0.027	0.230	1.222±0.105	0.851
CRF	89	-54.36 ±16.48	47.61	0.033±0.008	0.037	1.650±0.053	0.243	0.456±0.120	0.556
CVR	1593	3.75 ±18.71	69.41	0.183±0.004	0.073	1.789±0.007	0.141	1.508±0.036	0.725
GBR	139	-51.61 ±15.37	50.12	0.137±0.013	0.074	1.739±0.013	0.073	1.572±0.141	0.827
IKR	33	-47.57 ±22.85	44.73	0.146±0.026	0.072	1.767±0.038	0.107	1.027±0.188	0.534
JSP	3726	65.59 ±1.67	40.11	0.155±0.003	0.088	1.641±0.007	0.211	1.407±0.030	0.898
KVR	638	84.34 ±13.42	59.38	0.131±0.006	0.070	1.769±0.012	0.153	1.631±0.071	0.874
MLF	4785	-2.43 ±1.71	42.91	0.117±0.002	0.069	1.697±0.009	0.308	1.053±0.018	0.616
MTV	7281	61.67 ±3.04	55.60	0.150±0.002	0.071	1.771±0.001	0.039	0.623±0.008	0.328
SJQ	2396	57.95 ±2.12	40.41	0.151±0.003	0.066	1.670±0.004	0.091	1.010±0.022	0.536
SVR	1789	49.70 ±5.45	53.85	0.164±0.004	0.084	1.822±0.006	0.126	1.270±0.034	0.712
WJM	1754	8.86 ±2.62	41.47	0.231±0.004	0.077	1.702±0.003	0.066	1.184±0.025	0.524
Total	19076	34.24 ±2.20	57.86	0.157±0.001	0.084	1.686±0.003	0.209	1.199±0.010	0.698
All	102260	45.15 ±0.97	58.09	0.157±0.001	0.079	1.741±0.001	0.088	0.922±0.004	0.688

Only high quality measurements (described in Section 3.2.2) are presented in the summary table. ± represents the 95% confidence intervals. SD shows the standard deviation of the measurements. Station averages and standard deviation for fast orientations were performed using circular statistics. Event represents the number of event–station pair used for analysis. Total represents the summary of all stations for DPRI stations. All shows the summary of all stations for both GeoNet and DPRI stations.

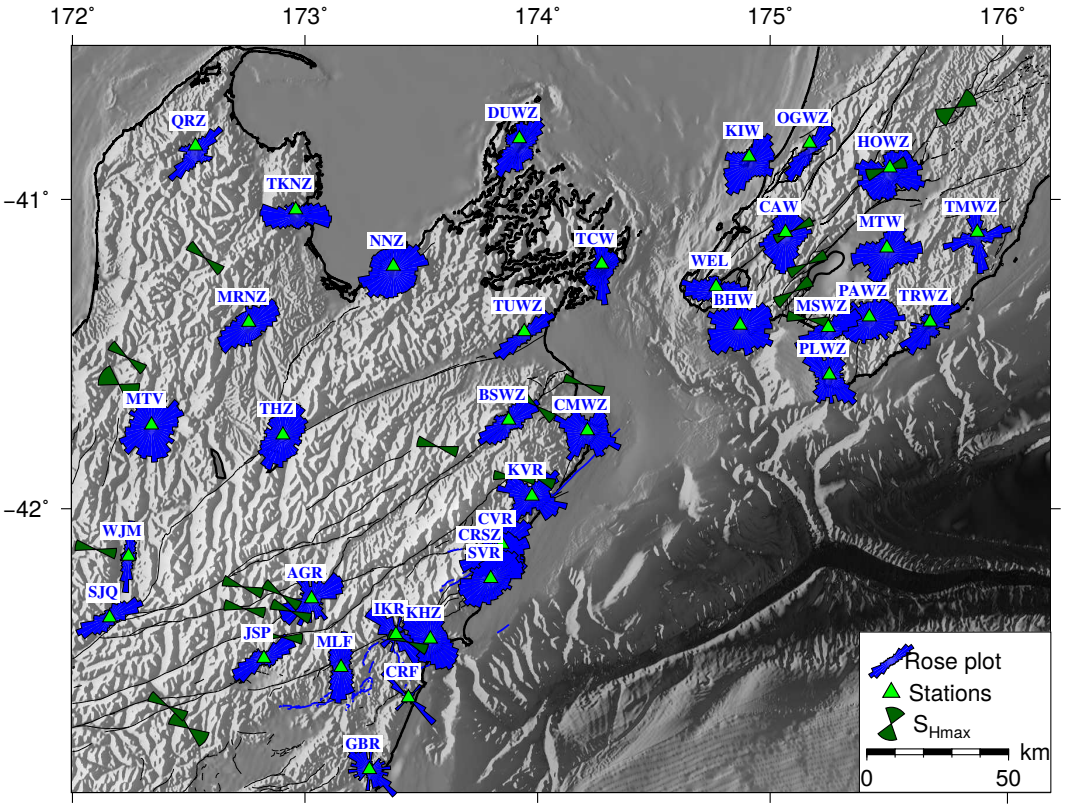

Figure 4. Rose diagrams (circular histograms) showing the ϕ orientation results from local S-phase events, ϕ. Rose diagrams are plotted on the stations at which measurements were made with a basemap of the digital topography and bathymetry. The green bow-ties shows the crustal S_{Hmax} orientations from Townend et al. (2012) and Balfour et al. (2005) with wedges showing the 95% confidence interval. The black lines are the active faults.

Around the southern end of the North island, the ϕ orientation at most stations exhibit significant variations from each other. Some stations exhibit a bi-modal distribution while others show a dominant NE-SW direction, with a few stations exhibiting trends that are neither parallel to S_{Hmax} nor to the strike the major faults. At stations TMWZ and MTW, a clear bi-modal distribution of fast polarization orientation is observed. One subset trends NE-SW and the other subset trends NW-SE (Figure 4).

To investigate temporal variations resulting from the 2016 Kaikōura mainshock, ϕ measurements were split into two subsets: before (from 01/01/13 to 13/11/16) and after (from 14/11/16 to 30/06/18) the Kaikōura mainshock. The 2013 Cook Strait earthquake sequence produced ample seismicity to determine the background ϕ orientation prior to the 2016 Kaikōura mainshock. Figure 5 shows rose diagrams of ϕ measurements before (Figure 5A) and after the 2016 Kaikōura mainshock (Figure 5B).

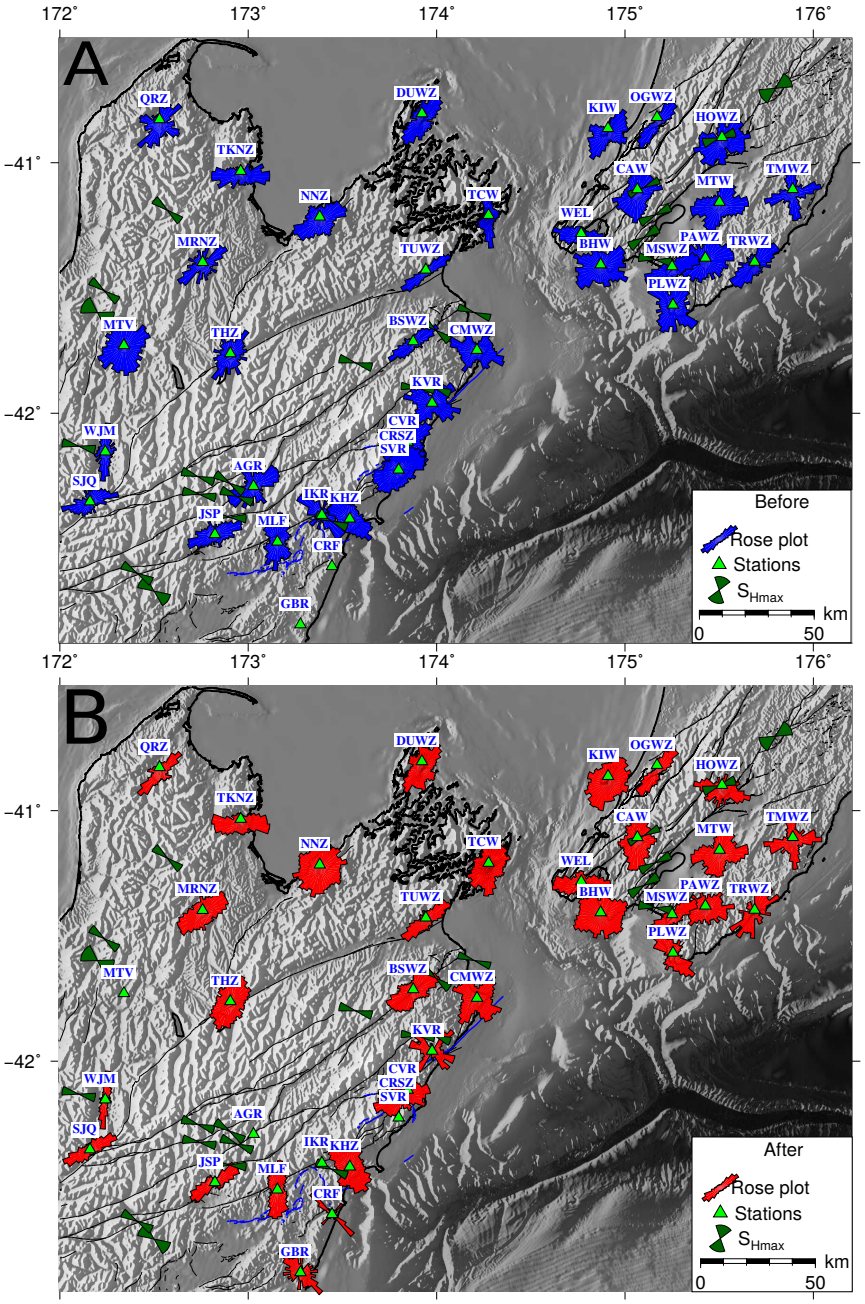

Figure 5. SWS fast orientation results from local S-phase events for before, A (from 01/01/13 to 13/11/16) and after, B (from 14/11/16 to 30/06/18) (bottom) Kaikōura mainshock. The ϕ orientation determined from events recorded at each station are represented as rose diagrams and plotted on a basemap of the digital topography. Rose diagrams are plotted on the stations at which measurements were made. The green bow-ties shows the S_{Hmax} orientations from Townend et al. (2012) and Balfour et al. (2005) with wedges showing the 95% confidence interval. The blue lines are the faults that ruptured during the Kaikōura Earthquake (Langridge et al., 2016).

4.1 Spatial Averaging

Using the technique described in Section 3.2.3, we performed spatial averaging analysis for more than 102,260 source-receiver ϕ measurements. Based on the criteria outlined in Section 3.2.3, 4579 out of 4720 grid elements created were used for analysis (see supplementary Figure S7). Circular averages of ϕ measurements in each grid square are represented by bar (colored by mean ϕ value) and plotted at the center of each grid square (Figure 6). The spatial averaging results shows a significant spatial variation. We observe a dominant NE-SW (see yellow bars on Figure 6) trend which is sub-parallel to the strike of the major active faults and also the topographic trends. We also note a clear contrast of perpendicular fast orientations (blue bars on Figure 6) around the eastern end of the MFS (the region that ruptured during the Kaikōura earthquake). This NW-SE feature existed before the 2016 Kaikōura sequence (see supplementary Figure S8).

To investigate the spatio-temporal variation of ϕ measurements associated with the 2016 Kaikōura mainshock we performed spatial averaging analysis for events before and after the earthquake. Using the method described in Section 3.2.4, we made quantitative comparisons of our spatially averaged ϕ measurements between events before and after the 2016 Kaikōura mainshock to search for potential spatio-temporal variations associated with the 2016 Kaikōura mainshock. The orientations of spatially averaged results for before (green bars) and after (blue bars) are shown in Figure 7. Generally, the orientations of the two angles are in agreement which indicates no significant spatial-temporal variation (in most cases the blue after bar is invisible under the exactly matching green before bar). The mean and median value of F (Section 3.2.4) is 0.92 ± 0.011 and 0.99 respectively (thus a mean and median difference of 23° and 10° respectively) indicates a strong agreement between the orientations before and after the mainshock. Out of the 898 co-located measurements, 88% of them had a test statistic value, F, above 0.8 (37°) with only 1% less than 0.2 (78°) (Figure 7B). The general agreement observed, also seen from the scatter plot (Figure 7C) of before and after measurements, suggests that there is no significant temporal variation associated with the 2016 Kaikōura earthquake. Although we observe a few patches of disagreement around the propagation path of the 2016 Kaikōura mainshock, we attribute this to spatial variation rather than temporal variation since ray paths for after measurements are slightly different from before measurements (see supplementary Figure S8). The red patch at the north-eastern edge of the study region may be due to an edge effect from the grid. Due to limited station coverage off-shore, we limit our discussion to onshore results.

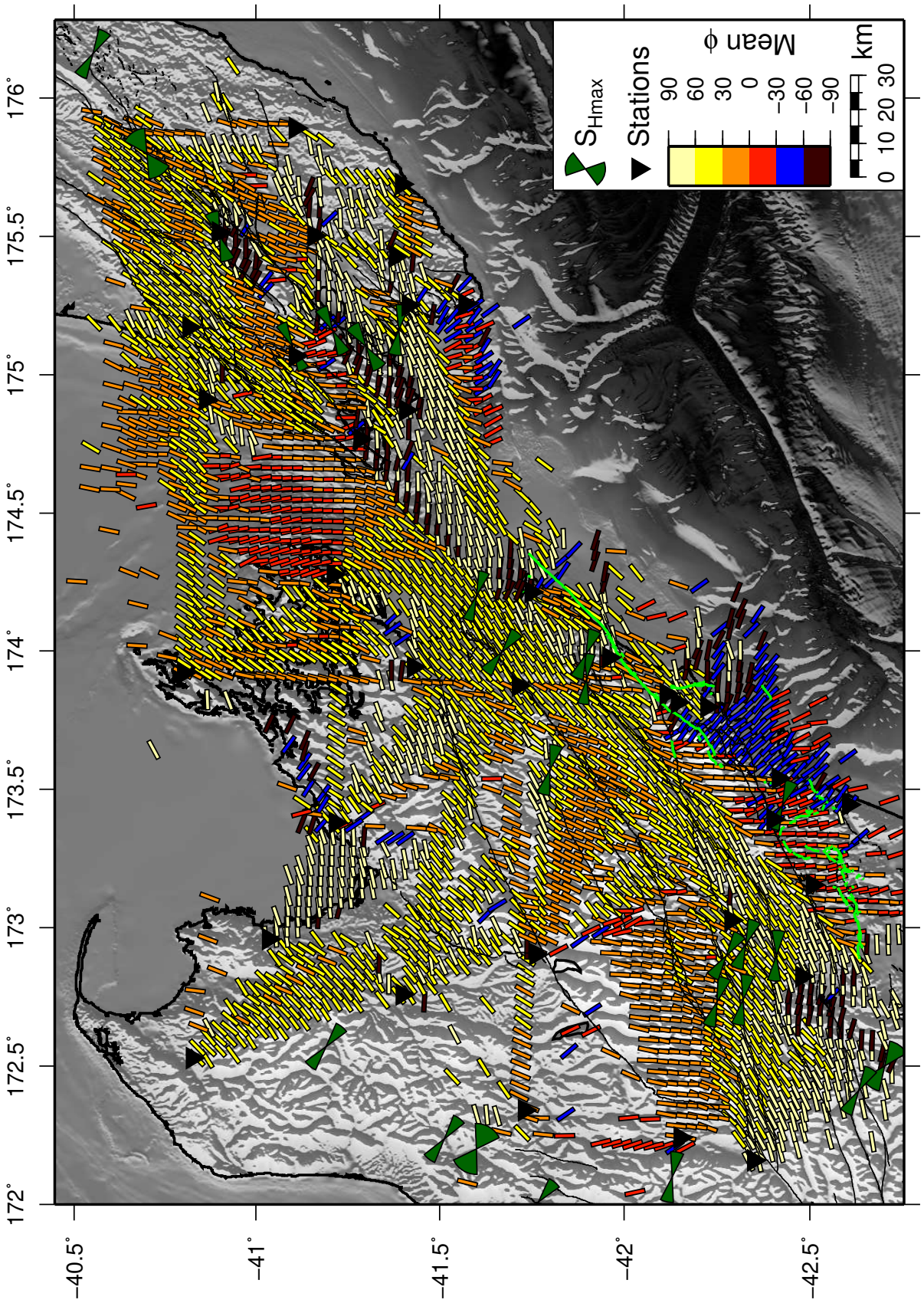

Figure 6. Spatial averages of fast polarization orientation with weighting inversely proportional to the square of the distance from the station. The bars are colored by the orientation of the mean ϕ. Black lines are known active faults from the NZ Active Faults Database and the green lines are the faults that ruptured during the 2016 Kaikōura main-shock (Litchfield et al., 2017).

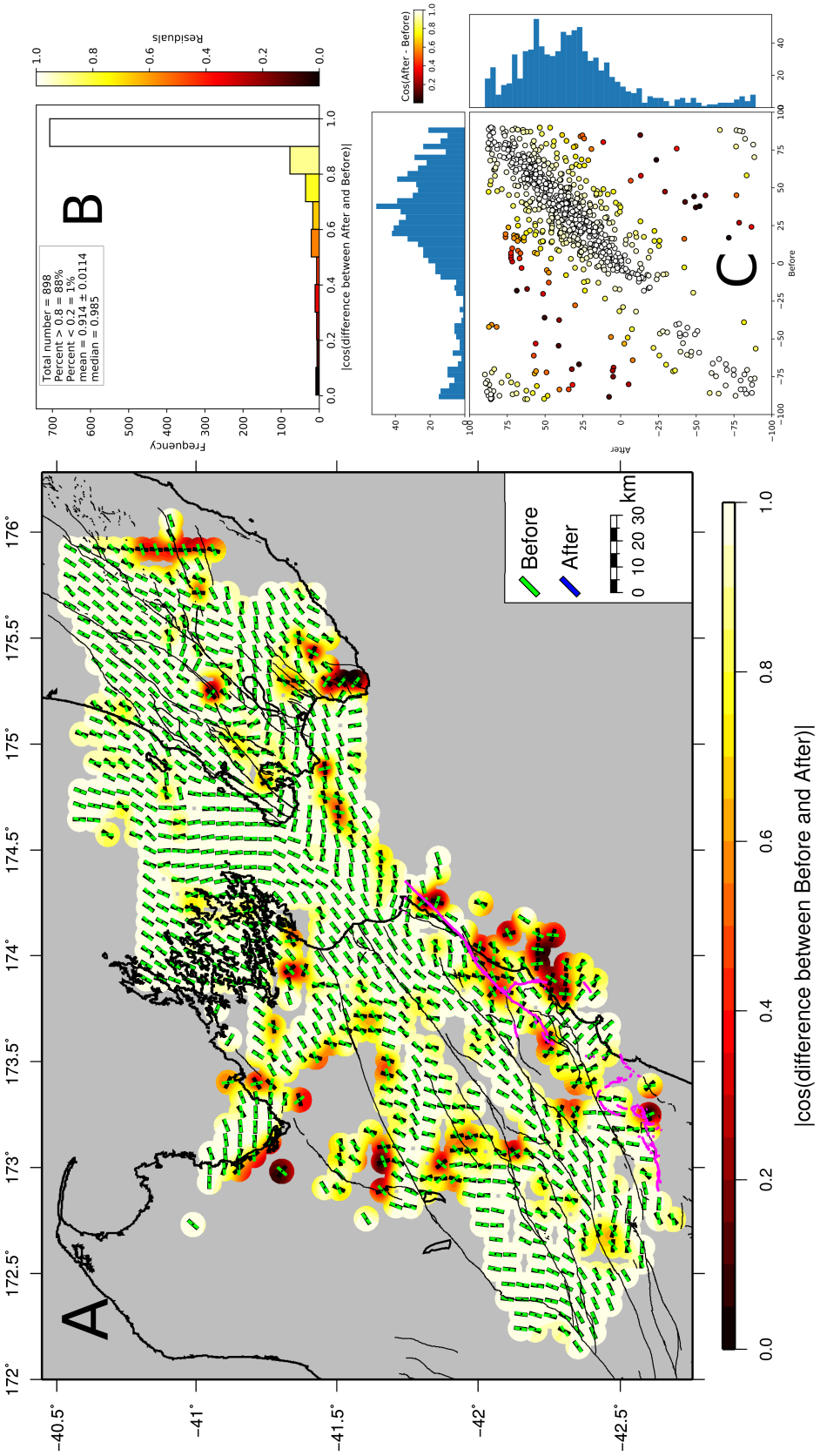

Figure 7. Quantitative comparison between splitting measurements for before and after the 2016 Kaikōura earthquake. The background colour is a contour of the absolute value of the cosine of the difference between the orientations, coloured by the scale at the bottom. Note that 1 represents no difference between the orientations. Before and after Kaikōura earthquake spatial averaging estimates are green and blue bars, respectively. The descriptive statistics of the difference between orientations at the closest grid points is displayed on the histogram in B. A scatter plot of the angles and histogram of each axis are shown in C.

5 Discussion

5.1 Overall station trends

The observed delay times, varying between near zero to 0.372 s, are in agreement with other SWS studies of crustal earthquakes (Audoine et al., 2000; Balfour et al., 2005; Crampin et al., 2015; Cochran & Kroll, 2015; Savage et al., 2016). V_p/V_s ratios varying from 1.58 to 2.22 with an average of 1.746±0.001, are also consistent with tomography results from Eberhart-Phillips & Fry (2018) and close to the global average of 1.76 for continental crust (Christensen, 1996). There is however substantial variability in ϕ measurements (the standard deviation of the ϕ measurements is greater than 30° at most stations). The observed large scatter of ϕ measurements suggests that the source of anisotropy may be a combination of more than one mechanism or that the mechanism varies rapidly spatially (Peng & Ben-Zion, 2004). The significant spatial variation we observe illustrates the complex regional tectonics and heterogeneous structures around central New Zealand.

The average δt we observed (Table 1 and 2) is about 6–14 percent of the values reported in SKS studies (∼1.6 sec) around New Zealand (Klosko et al., 1999; Zietlow et al., 2014). This small value in δt suggests that there is a deeper source of anisotropy beneath these stations that is measured by SKS and our measurement see shallow anisotropy. A similar conclusion has been reached by previous studies (Audoine et al., 2000; Karalliyadda & Savage, 2013) where they reported delay times for SKS measurement far greater than the observed local S-phase measurements. Similarly most studies of SKS waves assume the mantle is the main source of anisotropy (e.g. Savage, 1999).

The bi-modal distribution of fast orientation measurements observed at stations TMWZ and MTW on the North Island (Figure 4) reinforces previous observations. Audoine et al. (2000) reported a similar bi-modal distribution of ϕ measurements at stations LKER, LASH, LKIR, and SNZO, which were in close proximity to TMWZ and MTW. At stations HOWZ and BHW, the dominant ϕ orientation is parallel to faulting in the area and also sub-parallel to S_{Hmax}. The correlation between ϕ orientation and the active faults orientation at these stations suggests that the sources of anisotropy beneath them could be structurally controlled. However, the faults are also parallel to the strike of the topography, which is consistent with near surface gravitational stress. Fast orientations at stations WEL and TCW (on either side of the Cook Strait; Figure 4) are consistent with recent studies (Balfour et al., 2005; Evanzia et al., 2017) around the Marlborough and Wellington region. However,

they show neither an agreement with S_{Hmax} orientations, nor with tectonic structures in the region.

Around the Marlborough region, the faulting is mainly strike slip, thus based on Anderson's theory of faulting (Andersson, 1905; Healy et al., 2012), we expect the faults to generally strike at an angle of $\sim 30^{\circ}$ to the orientation of S_{Hmax}. Stations KHZ, IKR, CRF and GBR (and subset of ϕ measurements at stations KVR and CMWZ), located around the eastern end of the MFS have ϕ orientations that are sub-parallel to the orientation of S_{Hmax} rather than the fault fabric, suggesting stress-aligned micro-cracks (stress controlled anisotropy) exist (Figure 4 and 5). However, at these stations, the role of structural anisotropy cannot be completely ruled out since there are subsets of the ϕ measurements that are sub-parallel to the major structural features.

An abrupt change from NE-SW to a NW-SE trend of the averaged fast orientation (blue bars on Figure 6) is observed at the edge of the high irregular topography boundary around the eastern end of the MFS. This suggests that gravitational stresses could be contributing to the source of anisotropy around this region. In Section 5.5 we quantitively compare averaged ϕ to the orientation of $S^{Grav}_{H_{max}}$.

5.2 Search for temporal variation

The use of temporal variation in SWS measurements to monitor precursory changes preceeding major earthquakes is controversial (e.g. Aster et al., 1990; Crampin, 1990; Crampin et al., 2015). There have been studies that have used temporal variations to monitor coseismic stress changes (Saiga et al., 2003) and post-seismic fault healing after major earthquakes (Tadokoro et al., 1999; Tadokoro & Ando, 2002). Around the central Apennines of Italy, Piccinini et al. (2006) reported temporal variations in anisotropic parameters during the days before and after the occurrence of the 1997 Umbria-Marche seismic sequence. They suggested that the temporal variation is caused by the changes in local stress condition and fluid pressure. However, they concluded that spatial sampling of the selected ray paths may vary with time and the possible contribution of spatial variations of anisotropic parameters can not be excluded. Lucente et al. (2010) also observed a clear temporal variation of seismic anisotropy and velocities before the 2009 Mw 6.3 L'Aquila earthquake, Italy. They inferred that fluids, related to dilatancy-diffusion processes, played a key role in the fault failure process. In southern California, Yang et al. (2011) searched for possible temporal variations

of crustal anisotropy associated with big earthquakes, but they did not observe any clear temporal variations in delay times or fast orientation. In addition, studies by Liu (2004) of crustal anisotropy around the San Andreas Fault near Parkfield did not show systematic temporal variations. Moreover, a systematic analysis of crustal anisotropy associated with the 1999 Duzce main shock (Mw7.1) along the North Anatolian Fault by Peng & Ben-Zion (2004) also showed no temporal variations before, during or after the main shock.

One major issue with interpreting variations in observed SWS measurements is distinguishing temporal changes in anisotropy from spatial variations in anisotropy due to differing source locations (e.g. Peng & Ben-Zion, 2005). Since the propagation direction through the crust may be different for differing source locations, the wave is likely to sample different rock mass, resulting in different splitting parameters. In a complex setting, like the Marlborough and Wellington regions where the observed anisotropy may be controlled by different mechanisms, the determination of temporal variations is challenging, even if they exist. This is due to contamination associated with the variations of ray paths as a result of changes in source locations. However, clear temporal variation in stress have been observed for large earthquakes (Lucente et al., 2010; Holt et al., 2013).

5.2.1 Delay time and V_p/Vs ratios

We systematically searched for temporal variations in delay time and V_p/V_s associated with the 2013 Cook Strait and 2016 Kaikōura earthquakes. We applied the moving average technique described in Section 3.2.5 because our δt and V_p/Vs measurements exhibit large scatter without any clear trends. We tried a 10–, 20–, and 30– day moving window, and all showed similar results. A time series plot of δt and V_p/Vs measurements revealed apparent temporal variation at two stations (CAW and KIW, see supplementary Figure S9 A and B). We stacked measurement from all 36 station to enhance this variation observed in the individual stations (Figure 8A). To test whether the apparent variations originate from changes in the medium properties over time rather than changes in the source location or the propagation path, we selected a cluster of measurements within 20 km radius of station CMWZ (which is located in a region with a good number of measurements before and after both the 2013 and 2016 earthquakes sequence (Figure 8D). The apparent temporal variation of δt and V_p/V_s observed at individual stations with measurements from different locations was not seen when temporal analysis was done using only the small cluster of measurements (Figure S9 A[1] and B[1]). Similarly, the clear temporal variation observed with the stacked measure-

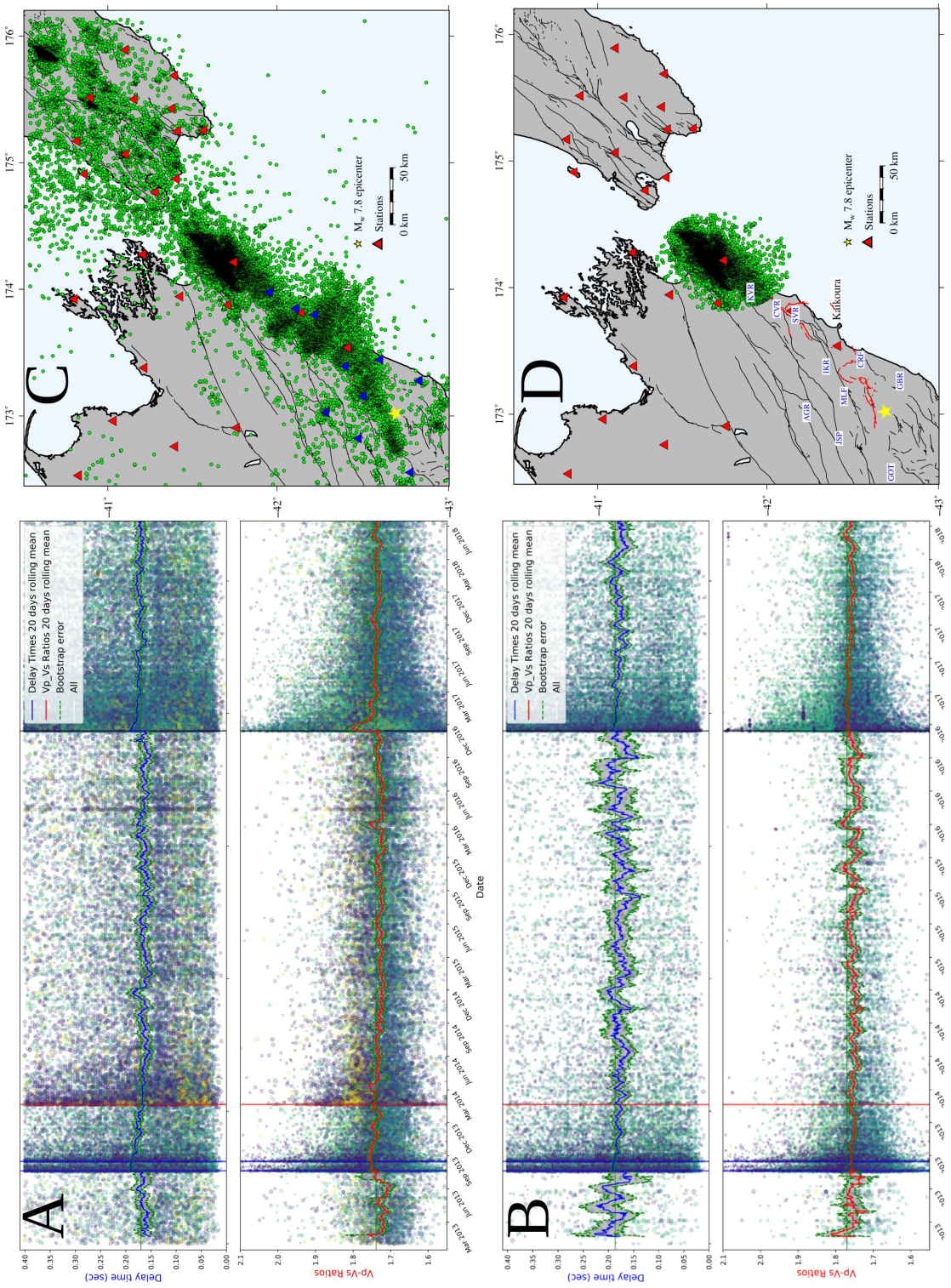

Figure 8. Time series of delay times, δt and V_p/V_s ratio for values from January, 2013 to June, 2018 are shown in panel A and B. A and B are plots for all measurements and the small cluster of measurements respectively for all stacked stations. C and D shows the event locations for all measurements and the small cluster of measurements respectively. Blue, red and orange vertical bars represent the mainshock of Seddon, Eketahuna and Kaikōura earthquake, respectively. Green horizontal line shows the median value. Green dashed line represents the estimated error using bootstrap. Red and blue lines are the 20 day moving median of V_p/V_s ratio and δt, respectively.

ment from different locations disappears when we stack individual stations measurements from earthquake with similar locations (Figure 8B). Moreover, analysis of measurements with similar back azimuths revealed no clear temporal variation. This indicates that spatial variations of parameters strongly affect the observed apparent temporal variations.

The absence of temporal variations in ϕ suggest that any change in the stress field around central New Zealand produced anisotropy changes that are small compared to structural anisotropy. Iidaka & Obara (2013) reported similar observation with the 2011 Tohuku earthquake. Their before and after analysis of fast polarization orientation revealed no changes and they suggested that the orientation of the maximum stress axis the region of increased seismicity did not change after the 2011 Tohoku earthquake (Iidaka & Obara, 2013). Focal mechanism inversion studies around central New Zealand following the 2016 Kaikōura earthquake (Okada et al., 2019, and personal communication with Tomomi Okada) also revealed no significant variation in the stress field. This corroborates our findings that the 2016 Kaikōura earthquake did not significantly alter the stress field around central New Zealand.

5.2.2 Fast orientations

To reveal the state of anisotropy over the $5\frac{1}{2}$ year period, we performed the spatial averaging analysis described in Section 3.2.3 with the same parameters for measurements within each year. As shown in Figure 9, there are significant spatial variations in the fast orientations but no systematic temporal variations. The general consistent spatial variations over the years demonstrate that neither the 2013 Cook Strait nor the 2016 Kaikōura earthquakes changed the stress directions significantly. Instead, we observe a consistent NE-SW trend (see yellow bars on Figure 9) that strikes sub-parallel to the active faulting around the study area. One remarkable feature is the consistent NW-SE orientation of fast orientation (blue bars) around Kaikōura region. This indicates that the NW-SE feature did not stem from the 2016 Kaikōura earthquake sequence.

5.3 Depth Extent of Anisotropy

Several studies have attempted to constrain the depth extent of anisotropy. Delay times observed by Audoine et al. (2000) showed no correlation with depth, which they attributed to the higher frequency phases used in their studies, thus sampling mainly the upper crustal anisotropy. In the Marlborough region, Balfour et al. (2005) also did not

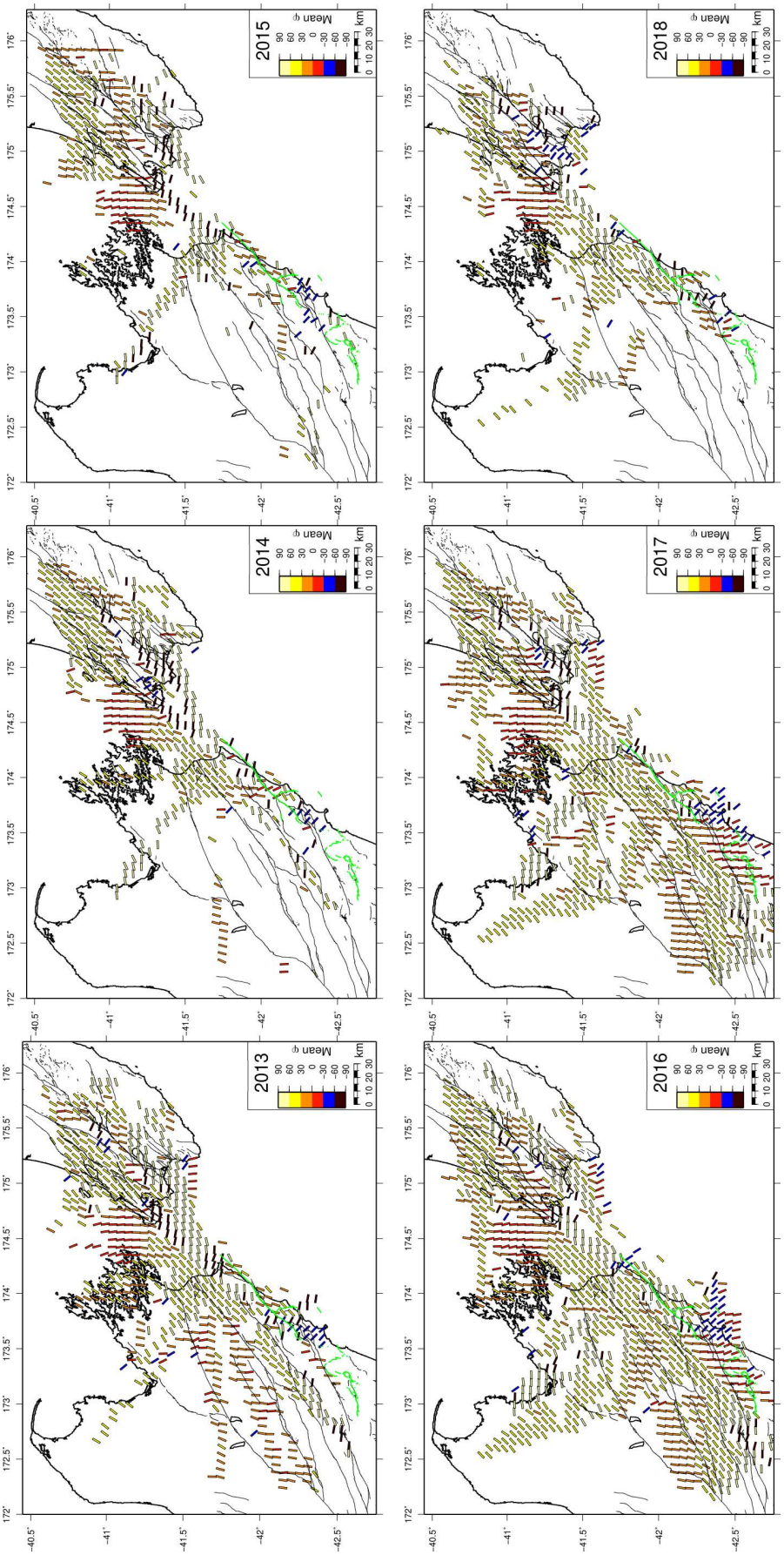

Figure 9. State of anisotropy over the $5\frac{1}{2}$ year period, The bars show the average fast orientation obtained at the each regular grid. We apply the same criteria as in Section 4.1. The green line are the fault lines the ruptured during the Kaikōura main-shock (Litchfield et al., 2017).

observe any systematic association between δt and depth and also suggested that the source of anisotropy may reside in the upper crust. Most of these studies conclude that anisotropy is confined to the upper few kilometers of the crust because their analysis often shows no clear correlation between delay time and hypocentral depth (Shih & Meyer, 1990; Audoine et al., 2000; Balfour et al., 2005, 2012; Gledhill, 1991).

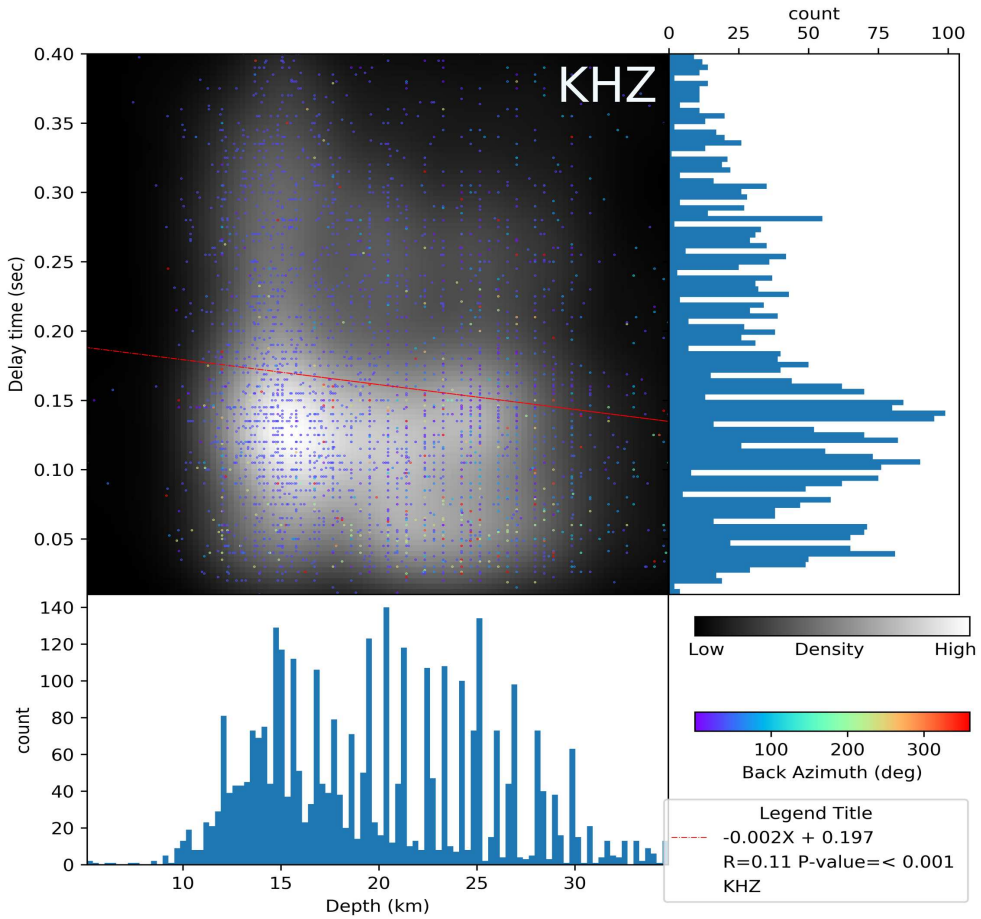

Figure 10. Delay times versus depth for station KHZ. Distribution of the delay time and depths are plotted on the right and bottom respectively. The scattered points are coloured by the depths and plotted on a basemap of the kernel density (effectively heatmap). High density regions are shaded white with low regions black. The red lines are the least square regression line with the equation and p-value displayed on the lower right corner of each plot.

We analysed the association between delay time and hypocentral depth and epicentral distance at individual stations (Figure 10 and supplementary Figure S10 respectively). The correlation coefficients at the analysed stations were less than 0.2, indicating a lack of clear correlation between delay time and hypocentral depth or epicental distance. This suggests

that we are mainly measuring anisotropy that resides only in the uppermost few kilometers of the crust (Shih & Meyer, 1990; Audoine et al., 2000; Balfour et al., 2005). Our results are also consistent with previous studies in this region and other tectonic regions (Gledhill, 1991; Audoine et al., 2000; Balfour et al., 2005; Zhang et al., 2007). The shallow sources of anisotropy observed may also suggest that topographic stresses (due to the difference in density between rock and air in the high topography areas) can contribute to the observed anisotropic pattern.

5.4 Discriminating between stress–induced and structural-control seismic anisotropy

Discriminating between stress–induced and structural-control seismic anisotropy in most tectonic settings is often challenging because S_{Hmax} is often sub-parallel to major structural features (Savage et al., 1989; Peng & Ben-Zion, 2004; Johnson et al., 2011). But in places where the S_{Hmax} orientation is at a high angle to the orientation of the major structural features (such as around the eastern end of the MFS near the Kaikōura region), it is possible to distinguish between stress–induced and structurally controlled anisotropy (Boness & Zoback, 2006; Zinke, 2000). Previous crustal anisotropy studies in central New Zealand have suggested that anisotropy in the region is controlled by a combination of both structures and stresses (e.g. Audoine et al., 2000; Balfour et al., 2005; Karalliyadda & Savage, 2013; Evanzia et al., 2017). Here we attempt to distinguish between stress–induced seismic anisotropy and structurally controlled seismic anisotropy. We quantitatively compared our spatially averaged ϕ measurements to the average orientation of the closest active fault segments following the method described in Section 3.2.4. Figure 11 indicates that our spatially averaged ϕ measurements, ϕ_{avg}, are overall oriented similar to the NE-SW strike of the active fault orientation. Out of 2297 measurements we compared, 70% of them had a test statistic value, F, above 0.8 with only 3% less than 0.2. The mean and median value of F was 0.81 $\pm$ 0.009 and 0.92 respectively (thus a mean and median difference of 35° and 23° respectively) indicating a strong agreement. The general agreement of average ϕ measurements with the orientation of active fault in polygon 1 (we exclude measurements in polygon 3 whose borders are contained within polygon 1) suggests that the observed anisotropy in polygon 1 may be controlled by structures. Around the eastern end of the MFS and part of the southern end of the North Island (polygon 2 and polygon 3 on Figure 11) the azimuth of ϕ_{avg} departs from the NE-SW trend to an almost E-W trend. This

departure shows a strong disagreement with the orientation of the active faults (red colour on Figure 11). This suggest that the anisotropy pattern observed within polygon 2 and polygon 3 is not structurally controlled. Agreement of the average ϕ with the orientation of active faults has also been reported elsewhere in areas of active transpression (Savage, 1999). However, the structural trends are also parallel to topographic trends. In the following sections we examine how both tectonic stresses (from focal mechanism inversion) and gravitational stresses may explain part of the observed anisotropic pattern.

5.5 Comparing spatially averaged ϕ with stress indicators

The gravitational forces exerted by dense material placed next to less dense material, such as high mountains next to air, can significantly contribute to the total stress field, which can result in variations in crustal differential stresses (Flesch et al., 2001). This induced stress is referred to as gravitationally induced stress, $S_{H_{max}}^{Grav}$ (Flesch et al., 2001; Hirschberg et al., 2018). The orientation and magnitude of gravitationally induced stresses can be modelled with a known crustal rock density, crustal thickness and surface topography. We used the Flesch et al. (2001) method implemented by Hirschberg et al. (2018) using finite difference methods to calculate the orientation and magnitude of gravitationally induced stresses. The implementation of the Flesch et al. (2001) method involves solving force balance equations, assuming an isotropic viscous medium. Following Hirschberg et al. (2018), we assume that the viscous medium is subjected to stresses and also assumed zero deviatoric stresses for the horizontal boundary condition. For our calculations, we used the 250 m gridded bathymetric dataset (Mitchell et al., 2012) around central New Zealand and assumed a crustal thickness and density of 30 km and 2850 kg/m^3, respectively. We modelled the orientation and magnitude of gravitationally induced stresses at a 30 km grid point spacing. At every grid point, we compared averaged ϕ to the orientation of the gravitationally induced stresses (Figure 12) following the method in Section 3.2.4.

Overall, we observe a general agreement between ϕ_{avg} and $S_{H_{max}}^{Grav}$, with the mean and median value of F of 0.77 $\pm$ 0.062 and 0.828 respectively (a mean and median difference of 39° and 34° respectively) (Figure 12B). Around the Marlborough region (Figure 12) the estimated $S_{H_{max}}^{Grav}$ is parallel to the ϕ_{avg} orientation. The NE-SW trend of $S_{H_{max}}^{Grav}$ is also in agreement with the trend of the structures. Combined with the results in Section 5.4, this suggests the anisotropy pattern observed in polygon 1 could be controlled by either gravitational stresses or structure or a combination of the two. In polygon 2, where

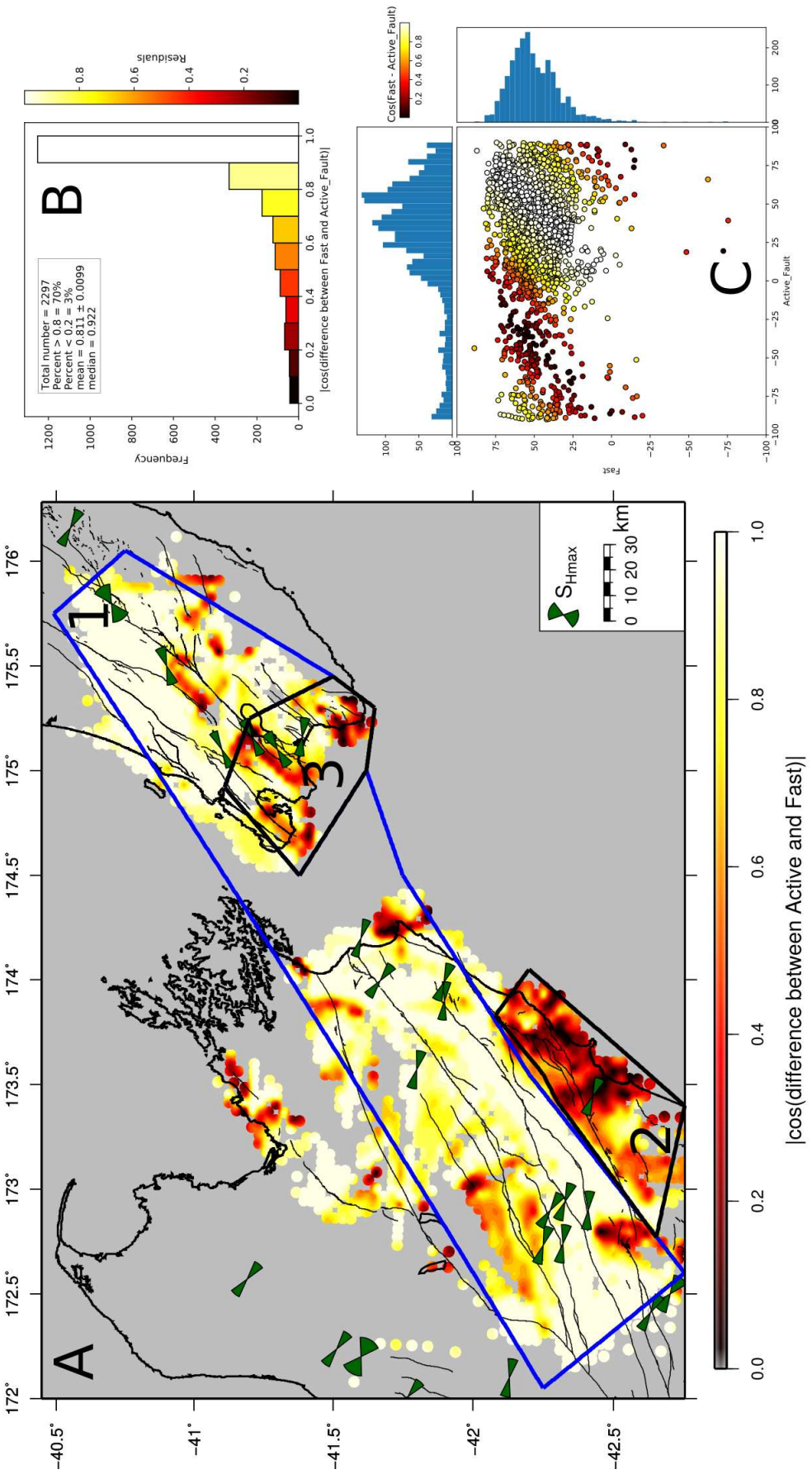

Figure 11. Quantitative comparison between spatially averaged ϕ measurements and average orientation of the closest active fault. The background colour is a contour of the absolute value of the cosine of the difference between the orientations, coloured by the scale at the bottom. Note that 1 represents no difference between the orientations. The descriptive statistics of the difference between orientations at the closest grid points is displayed on the histogram in B. S_{Hmax} are represented by dark green bow ties. A scatter plot of the angles and histogram of each axis are shown in C.

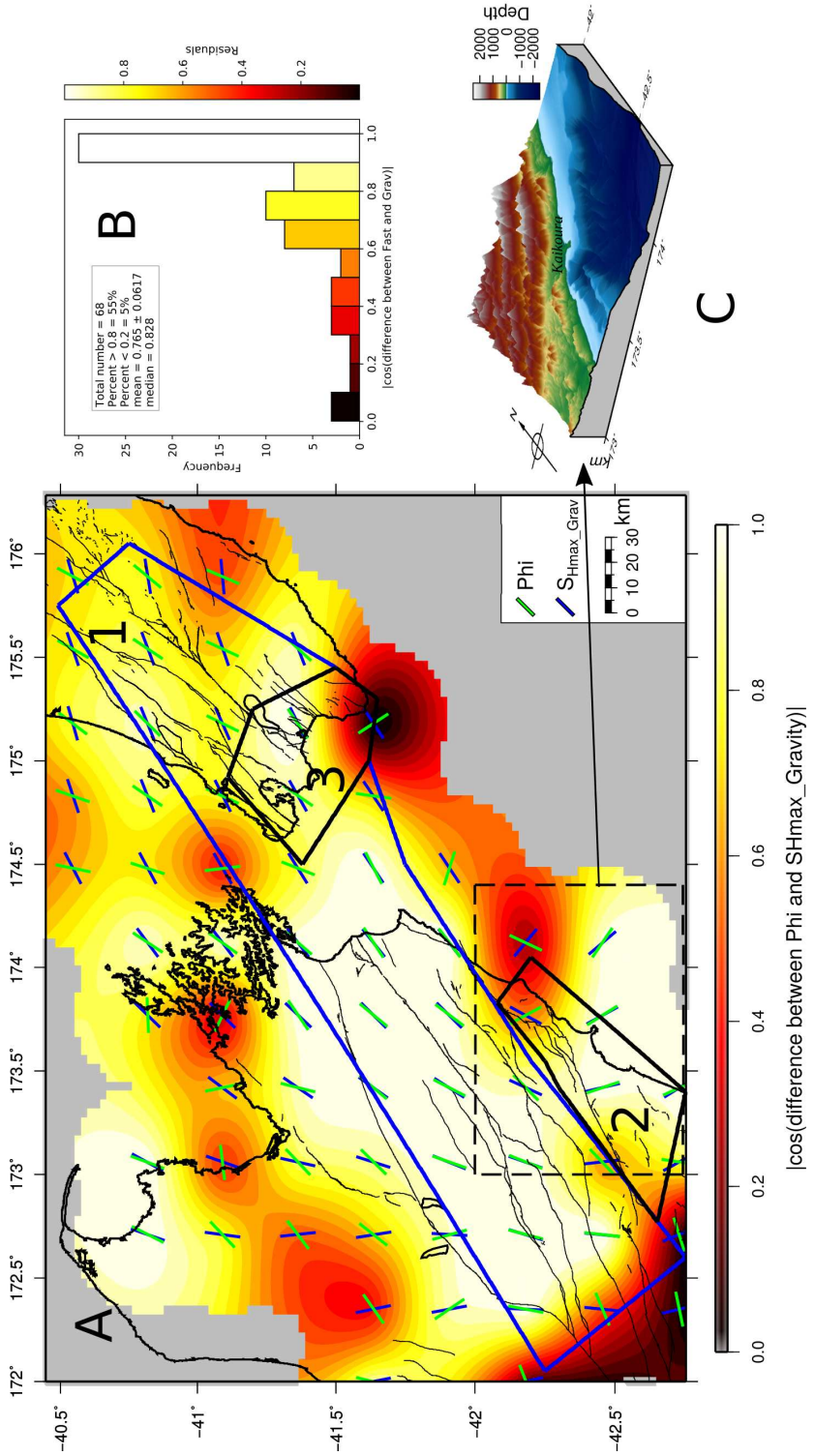

Figure 12. Quantitative comparison between spatially averaged ϕ measurements and orientation of gravitationally induced stress. The background colour is a contour of the absolute value of the cosine of the difference between the orientations, coloured according to the scale at the bottom. Note that 1 represents no difference between the orientations. The descriptive statistics of the difference between orientations at the closest grid points is displayed on the histogram in B. C is a 3-D perspective image of the topography and bathymetry map around Kaikōura region.

agreement between the ϕ_{avg} and the orientation of the active fault is poor (Figure 11), we observe a general agreement between ϕ_{avg} and $S^{Grav}_{H_{max}}$ (Figure 12). We infer that the observed seismic anisotropy in polygon 2 (Figure 11 and 12) is best explained by the gravitationally induced stress that originates from the variations in topography around the region (Figure 12C).

We also examine how tectonic stresses explain the observed anisotropic patterns by comparing ϕ orientation measurements to the orientation of S_{Hmax} from focal mechanisms. Figure S11, in the supplementary material, illustrates the comparison of ϕ orientations with the nearest S_{Hmax} following the quantitative analysis described in Section 3.2.4. Around the northern South Island, we observe a general disagreement between ϕ_{avg} and S_{Hmax} orientations (mean F of 0.47 $\pm$ 0.01, 62° angle difference; see supplementary Figure S11). The general disagreement observed in the South Island is an indication that a different source of anisotropy, other than tectonic stresses is needed to explain the anisotropic pattern. Since the mean depth distribution of the focal mechanism inversion used for comparison is about 16.12 $\pm$ 2.08 km (see supplementary Figure S11 C), we suggest that the tectonic stresses are acting on deeper structures than the measured anisotropic structure. Our results reinforce Balfour et al.'s observations that the tectonic stress field does not control the crustal anisotropy pattern around the Marlborough region. Conversely, in the North Island, the ϕ_{avg} orientations generally agree with S_{Hmax} orientations (mean F of 0.75 $\pm$ 0.02, 42° angle difference). This agreement is an indication that tectonic stresses may contribute to the observed anisotropic pattern, although as shown in Section 5.4 structure may also explain the anisotropy here. Evanzia et al. (2017) observed a similar agreement and suggested that stresses in the overriding plate and gravitational stresses control the anisotropic pattern in the Wellington region.

5.6 Comparing the geodetically determined plane of maximum shear stress with spatially averaged ϕ

In the Marlborough and Wellington regions, the tectonics are complicated by the locked part of the Hikurangi subduction zone and a series of parallel strike-slip faults (MFS). In Figure 13 spatial averaging of ϕ orientations is compared with the plane of maximum shear stress (we assume to be 45° to the principal axes (compressional and extensional plane) of the strain rate field (Ciucu, 2010)). We used the strain rate field result calculated by Lamb et al. (2018). The observed NE-SW trend of the ϕ orientation, which generally shows

good agreement with the plane of maximum shear stress (polygon 1 on Figure 13), probably reflects the effect of the shear deformation along the Australian/Pacific boundary.

Present deformation along the plate-boundary zone in north eastern South Island, New Zealand is expected to influence anisotropy (Wilson et al., 2004; Balfour et al., 2005; Karalliyadda & Savage, 2013; Chen et al., 2013). Okaya et al. (2016) suggested that the sub-horizontal foliations with lineations (e.g. schist fabric), developed due to pervasive shearing in strike-slip fault zones, are a possible source of anisotropy. We therefore infer that the margin-parallel orientation of ϕ observed could be caused either by gravitational stress or shear deformation across the Marlborough region as a result of shearing along the active faulting (MFS) or both. The general disagreement of the orientations observed in polygon 2 underpins our earlier interpretation (Section 5.4) that these regions are likely controlled by gravitational stresses.

5.7 What controls seismic anisotropy in central New Zealand

Several studies around the MFS and the Wellington region (e.g. Gledhill, 1991; Audoine et al., 2000; Matcham et al., 2000; Balfour et al., 2005; Karalliyadda & Savage, 2013; Evanzia et al., 2017) suggest that the anisotropy in the crust is either structural-control or stress–induced. Here, we try to delineate regions where the proposed source of anisotropy best explains our results by comparing the mean values on the F statistic in each polygon, both North and South Island, and the entire study region. We looked at how the structural-control hypothesis (using active fault and maximum shear plane orientations as a proxy) and stress induced hypothesis (relating to gravitational and tectonic stresses) explain the observed anisotropic pattern. In polygon 1 (Figure 14, and for regions see Figure 11), both gravitational stresses and structures can explain (with the mean F >0.8) the anisotropic pattern observed. This is because the active faults and foliation, or aligned minerals (due to shearing) in the area are oriented parallel to the strike of the topographic structures, which are also the ridges. Gravitational stresses is the hypothesis that best explains the anisotropic pattern in polygon 2 (with the mean F >0.8). This is likely due to the sharp topography contrast (Figure 12C) observed around the Kaikōura region. In polygon 3, no single hypothesis can explain the observation (with the mean F <0.7). In the North Island, overall either stresses (tectonic and gravitational) or structures or both explain our results. However, in the South Island gravitational stresses and structures best explain our results.

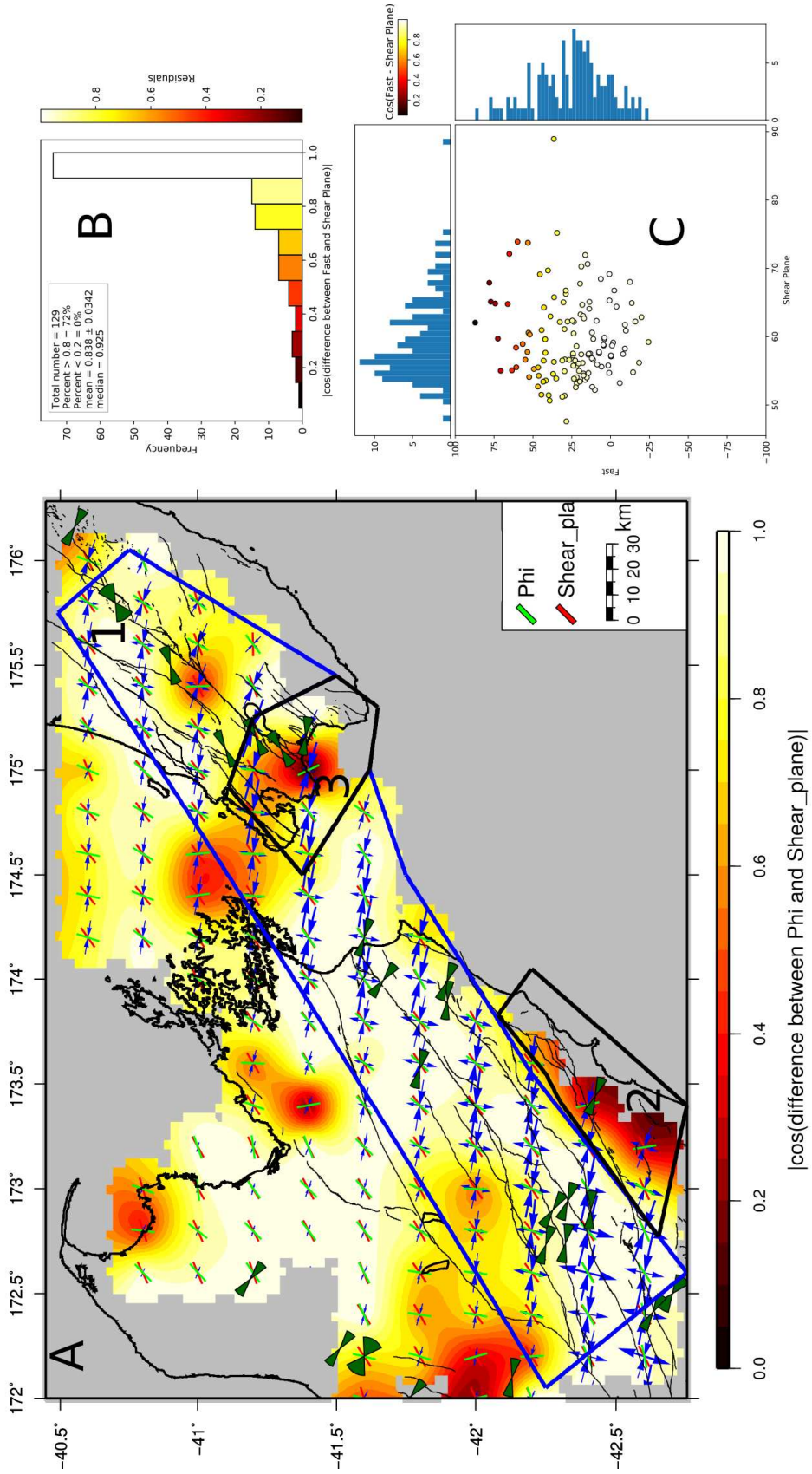

Figure 13. Quantitative comparison between spatially averaged ϕ measurements and the plane of maximum shear stress (from Lamb et al., 2018). The background colour is a contour of the absolute value of the cosine of the difference between the orientations, coloured by the scale at the bottom. Note that 1 represents no difference between the orientations. The descriptive statistics of the difference between orientations at the closest grid points is displayed on the histogram in B. Scatter plot of the angles in shown in C. S_{Hmax} are represented by dark green bow ties. The red and green bars illustrate the plane of maximum shear stress and mean ϕ orientation at each grid point respectively. The blues arrows indicate the principle axes strain rate, with compression pointing inwards and extension outwards.

Overall the gravitational stress induced hypothesis can explain most regions. However, structural controls cannot be ruled out for any region except polygon 2.

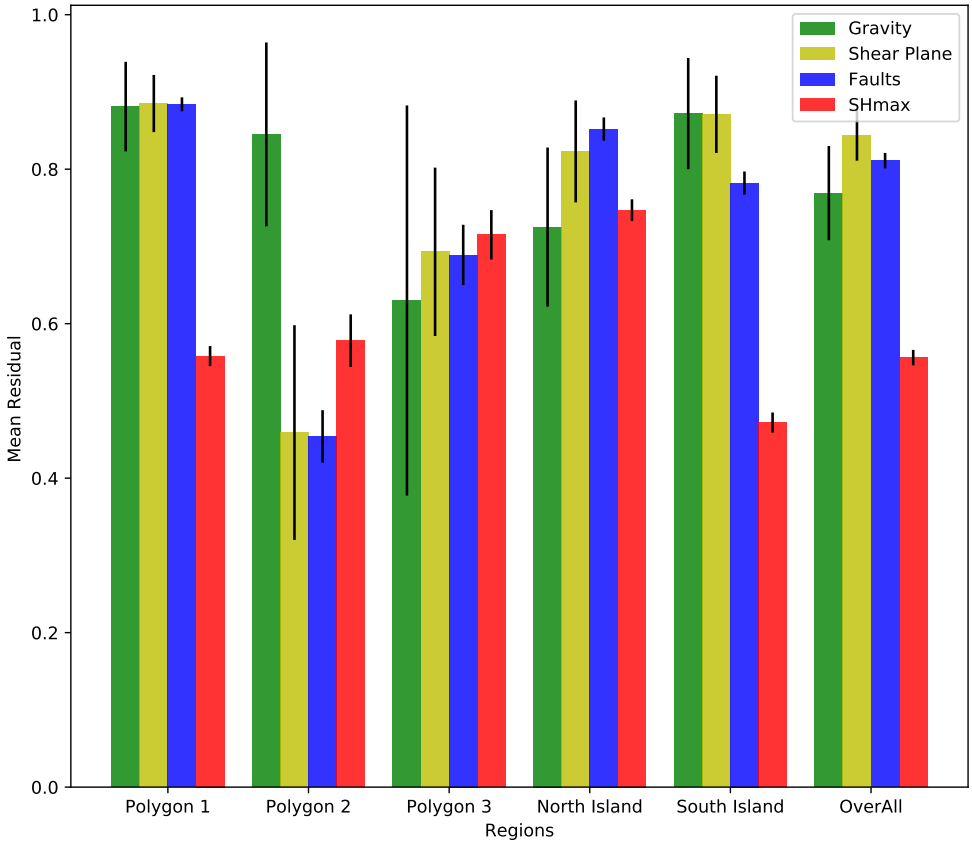

Figure 14. Qualitative comparison of the possible source of crustal anisotropy around the study area. The bar chart is grouped by the delineated regions and in each region the proposed sources of crustal anisotropy (color corded in the legend) is compared. Green, blue, red and yellow bars represent gravitational stresses, active fault orientation, S_{Hmax} orientation from focal mechanism and maximum shear plane orientation, respectively

6 Conclusions

We have presented the largest number of measurements of high-quality SWS parameters (~102,000) around the Marlborough and Wellington region with a detailed systematic analysis of crustal anisotropy using over 40,000 crustal earthquakes recorded on at least one of the 36 stations. The size of our data set has allowed us to show the detailed spatial and temporal variation of anisotropic structure around central New Zealand. We conclude that the crustal anisotropy around the study region is confined to the upper few kilome-

ters of the crust and can be controlled by either one mechanism or a combination of more than one. The high correspondence between S_{Hmax} calculated from gravitational potential energy from topography and average fast polarization orientation around the Marlborough and Kaikōura region suggest that gravitationally induced stresses contribute to the crustal anisotropy around the region. In the North Island tectonic stresses inferred from focal mechanisms as well as geological structures could contribute to the observed anisotropy. In the South Island gravitational potential energy gives the best overall match, but inherited geological structures could contribute and control some regions. We suggest that examining the effect of gravitational stresses on crustal seismic anisotropy should not be neglected in future studies. We do not observe any spatiotemporal variation of the state of anisotropy over the $5\frac{1}{2}$ year period. Apparent temporal variations of δt and V_P/V_S are mainly due to spatial variations of anisotropy combined with temporal varying paths of seismic waves.

Acknowledgments

This work is supported by funding from Victoria University of Wellington (PhD scholarship) and the Earthquake commission (EQC Grant number: 18/755). We are grateful to Simon Lamb, Carolyn Boulton, Katrina Jacobs and Hamish Hirschberg for their discussions and helpful feedback. Waveform data and earthquake catalogs used for this study were provided by New Zealand GeoNet and are available from https://quakesearch.geonet.org.nz/. Most figures were prepared using the Generic Mapping Tools (Wessel et al., 2013). A table of our shear wave splitting measurements can be found at https://zenodo.org/record/3738129. Codes used to estimate the orientation and magnitude of gravitationally induced stresses can be found at https://github.com/hamishhirschberg/stress-modelling.

References

Allen, R. V. (1978). Automatic earthquake recognition and timing from single traces. *Bulletin of the Seismological Society of America*, *68*(5), 1521-1532.

Anderson, H., Webb, T., & Jackson, J. (1993). Focal mechanisms of large earthquakes in the South Island of New Zealand: implications for the accommodation of Pacific-Australia plate motion. *Geophysical Journal International*, *115*(3), 1032–1054. doi: 10.1111/j.1365-246x.1993.tb01508.x

Andersson, E. M. (1905). The dynamics of faulting. *Transactions of the Edinburgh Geological Society*, *8*(3), 387–402. doi: 10.1144/transed.8.3.387

Andreas, W. (2010). *Automatic shear wave splitting measurements at Mt. Ruapehu volcano, New Zealand* (Unpublished master's thesis). Victoria University of Wellington.

Araragi, K. R., Savage, M. K., Ohminato, T., & Aoki, Y. (2015). Seismic anisotropy of the upper crust around Mount Fuji, Japan. *Journal of Geophysical Research: Solid Earth*, *120*(4), 2739–2751. doi: 10.1002/2014jb011554

Arnold, R., & Townend, J. (2007). A Bayesian approach to estimating tectonic stress from seismological data. *Geophysical Journal International*, *170*(3), 1336-1356. doi: 10.1111/j.1365-246X.2007.03485.x

Aster, R. C., Shearer, P. M., & Berger, J. (1990). Quantitative measurements of shear wave polarizations at the Anza Seismic Network, southern California: Implications for shear wave splitting and earthquake prediction. *Journal of Geophysical Research: Solid Earth*, *95*(B8), 12449-12473. doi: 10.1029/JB095iB08p12449

Audoine, E., Savage, M. K., & Gledhill, K. (2000). Seismic anisotropy from local earth-

quakes in the transition region from a subduction to a strike-slip plate boundary, New Zealand. *Journal of Geophysical Research: Solid Earth*, *105*(B4), 8013-8033. doi: 10.1029/1999JB900444

Babuska, V., & Cara, M. (1991). *Seismic anisotropy in the Earth* (Vol. 10). Springer Science & Business Media.

Balfour, N., Cassidy, J. F., & Dosso, S. E. (2012). Crustal anisotropy in the forearc of the Northern Cascadia Subduction Zone, British Columbia. *Geophysical Journal International*, *188*(1), 165–176. doi: 10.1111/j.1365-246X.2011.05231.x

Balfour, N., Savage, M., & Townend, J. (2005). Stress and crustal anisotropy in Marlborough, New Zealand: evidence for low fault strength and structure-controlled anisotropy. *Geophysical Journal International*, *163*(3), 1073–1086.

Berens, P. (2009). CircStat: A MATLAB Toolbox for circular statistics. *Journal of Statistical Software*, *31*(10). doi: 10.18637/jss.v031.i10

Bianco, F., Scarfi, L., Pezzo, E. D., & Patanè, D. (2006). Shear wave splitting changes associated with the 2001 volcanic eruption on Mt Etna. *Geophysical Journal International*, *167*(2), 959–967. doi: 10.1111/j.1365-246x.2006.03152.x

Boness, N., & Zoback, M. (2006). Mapping stress and structurally controlled crustal shear velocity anisotropy in California. *Geology*, *34*(10), 825–828.

Castellazzi, C., Savage, M., Walsh, E., & Arnold, R. (2015). Shear wave automatic picking and splitting measurements at Ruapehu volcano, New Zealand. *Journal of Geophysical Research: Solid Earth*, *120*, 3363–3384.

Cesca, S., Zhang, Y., Mouslopoulou, V., Wang, R., Saul, J., Savage, M., ... Dahm, T. (2017). Complex rupture process of the Mw 7.8, 2016, Kaikōura earthquake, New Zealand, and its aftershock sequence. *Earth and Planetary Science Letters*, *478*, 110–120. doi: 10.1016/j.epsl.2017.08.024

Chen, Y., Zhang, Z., Sun, C., & Badal, J. (2013). Crustal anisotropy from Moho converted Ps wave splitting analysis and geodynamic implications beneath the eastern margin of Tibet and surrounding regions. *Gondwana Research*, *24*(3-4), 946–957. doi: 10.1016/j.gr.2012.04.003

Chiarabba, C., Gori, P. D., & Boschi, E. (2009). Pore-pressure migration along a normal-fault system resolved by time-repeated seismic tomography. *Geology*, *37*(1), 67–70. doi: 10.1130/g25220a.1

Christensen, N. I. (1996). Poisson's ratio and crustal seismology. *Journal of Geophysical*

Research: Solid Earth, *101*(B2), 3139–3156. doi: 10.1029/95jb03446

Ciucu, C. (2010). Maximum Stress at a Tectonic Fault Plane. Coulomb Law. *Romanian Reports in Physics*, *62*(2), 414–421.

Clark, K., Nissen, E., Howarth, J., Hamling, I., Mountjoy, J., Ries, W., ... Strong, D. (2017). Highly variable coastal deformation in the 2016 Mw 7.8 Kaikōura earthquake reflects rupture complexity along a transpressional plate boundary. *Earth and Planetary Science Letters*, *474*, 334–344. doi: 10.1016/j.epsl.2017.06.048

Cochran, E., & Kroll, K. (2015). Stress- and structure-controlled anisotropy in a region of complex faulting—Yuha Desert, California. *Geophysical Journal International*, *202*(2), 1109–1121. doi: 10.1093/gji/ggv191

Cochran, E., Li, Y.-G., & Vidale, J. (2006). Anisotropy in the shallow crust observed around the San Andreas fault before and after the 2004 M 6.0 Parkfield earthquake. *Bulletin of the Seismological Society of America*, *96*(4B), S364–S375.

Crampin, S. (1984). An introduction to wave propagation in anisotropic media. *Geophysical Journal International*, *76*(1), 17–28. doi: 10.1111/j.1365-246X.1984.tb05018.x

Crampin, S. (1990). The scattering of shear-waves in the crust. *Pure and Applied Geophysics PAGEOPH*, *132*(1-2), 67–91. doi: 10.1007/bf00874358

Crampin, S., & Booth, D. C. (1989). Shear-wave splitting showing hydraulic dilation of pre-existing joints in granite. *Scientific Drilling*, *1*(1), 21–26.

Crampin, S., & Gao, Y. (2006). A review of techniques for measuring shear-wave splitting above small earthquakes. *Physics of the Earth and Planetary Interiors*, *159*(1-2), 1–14. doi: 10.1016/j.pepi.2006.06.002

Crampin, S., Gao, Y., & Bukits, J. (2015). A review of retrospective stress-forecasts of earthquakes and eruptions. *Physics of the Earth and Planetary Interiors*, *245*, 76–87. doi: 10.1016/j.pepi.2015.05.008

Crotwell, H. P., Owens, T. J., & Ritsema, J. (1999). The TauP Toolkit: Flexible Seismic Travel-time and Ray-path Utilities. *Seismological Research Letters*, *70*(2), 154–160. doi: 10.1785/gssrl.70.2.154

Dellow, S., Massey, C., Cox, S., Archibald, G., Begg, J., Bruce, Z., & et al. (2017). Landslides caused by the 14 November 2016 Mw7.8 Kaikōura earthquake and the immediate response. *Bulletin of the New Zealand Society for Earthquake Engineering*, *50*(2), 106–116.

Diehl, T., Deichmann, N., Kissling, E., & Husen, S. (2009). Automatic S-Wave Picker for Local Earthquake Tomography. *Bulletin of the Seismological Society of America*, *99*(3),

1906–1920. doi: 10.1785/0120080019

Duputel, Z., & Rivera, L. (2017). Long-period analysis of the 2016 Kaikōura earthquake. *Physics of the Earth and Planetary Interiors*, *265*, 62–66. doi: 10.1016/j.pepi.2017.02.004

Dvorkin, J., Mavko, G., & Nur, A. (1999). Overpressure detection from compressional- and shear-wave data. *Geophysical Research Letters*, *26*(22), 3417–3420. doi: 10.1029/1999gl008382

Eberhart-Phillips, D., & Fry, B. (2018). Joint local earthquake and teleseismic inversion for 3-D velocity and Q in New Zealand. *Physics of the Earth and Planetary Interiors*, *283*, 48–66. doi: 10.1016/j.pepi.2018.08.005

Evanzia, D., Wilson, T., Savage, M. K., Lamb, S., & Hirschberg, H. (2017). Stress Orientations in a Locked Subduction Zone at the Southern Hikurangi Margin, New Zealand. *Journal of Geophysical Research: Solid Earth*, *122*(10), 7895–7911. doi: 10.1002/2017jb013998

Flesch, L. M., Haines, A. J., & Holt, W. E. (2001). Dynamics of the India-Eurasia collision zone. *Journal of Geophysical Research: Solid Earth*, *106*(B8), 16435–16460. doi: 10.1029/2001jb000208

Flinn, E. (1965). Signal analysis using rectilinearity and direction of particle motion. *Proceedings of the IEEE*, *53*(12), 1874–1876. doi: 10.1109/proc.1965.4462

GeoNet. (2019, accessed February 2, 2019). Geonet quake search catalog [Computer software manual]. (`https://quakesearch.geonet.org.nz/`)

Gledhill, K. R. (1991). Evidence for shallow and pervasive seismic anisotropy in the Wellington Region, New Zealand. *Journal of Geophysical Research: Solid Earth*, *96*(B13), 21503-21516. doi: 10.1029/91JB02049

Hamling, I. J., D'Anastasio, E., Wallace, L. M., Ellis, S., Motagh, M., Samsonov, S., ... Hreinsdóttir, S. (2014). Crustal deformation and stress transfer during a propagating earthquake sequence: The 2013 Cook Strait sequence, central New Zealand. *Journal of Geophysical Research: Solid Earth*, *119*(7), 6080–6092. doi: 10.1002/2014jb011084

Hamling, I. J., Hreinsdóttir, S., Clark, K., Elliott, J., Liang, C., Fielding, E., ... Stirling, M. (2017). Complex multifault rupture during the 2016 Mw 7.8 Kaikōura earthquake, New Zealand. *Science*, *356*(6334), 1 – 10. doi: dio:10.1126/science.aam7194

Hardebeck, J. L., & Michael, A. J. (2006). Damped regional-scale stress inversions: Methodology and examples for southern California and the Coalinga aftershock sequence. *Journal*

of Geophysical Research: Solid Earth, *111*(B11). doi: 10.1029/2005jb004144

Hardebeck, J. L., & Okada, T. (2018). Temporal stress changes caused by earthquakes: A review. *Journal of Geophysical Research: Solid Earth*, *123*(2), 1350–1365. doi: 10.1002/2017jb014617

Healy, D., Sibson, R. H., Shipton, Z., & Butler, R. (2012). Stress, faulting, fracturing and seismicity: the legacy of ernest masson anderson. *Geological Society, London, Special Publications*, *367*(1), 1–6. Retrieved from `https://doi.org/10.1144/sp367.1` doi: 10.1144/sp367.1

Hirschberg, H. P., Lamb, S., & Savage, M. K. (2018). Strength of an obliquely convergent plate boundary: lithospheric stress magnitudes and viscosity in New Zealand. *Geophysical Journal International*, *216*(2), 1005–1024. doi: 10.1093/gji/ggy477

Holden, C., Kaiser, A., Van Dissen, R., & Jury, R. (2013). Sources, ground motion and structural response characteristics in Wellington of the 2013 Cook Strait earthquakes. *Bull. New Zeal. Soc. Earthq. Eng.*, *46*(4), 188–195.

Holden, C., Kaneko, Y., D'Anastasio, E., Benites, R., Fry, B., & Hamling, I. (2017). The 2016 Kaikōura Earthquake Revealed by Kinematic Source Inversion and Seismic Wavefield Simulations: Slow Rupture Propagation on a Geometrically Complex Crustal Fault Network. *Geophysical Research Letters*, *44*(22). doi: 10.1002/2017GL075301

Holt, R., Savage, M., Townend, J., Syracuse, E., & Thurber, C. (2013). Crustal stress and fault strength in the Canterbury Plains, New Zealand. *Earth and Planetary Science Letters*, *383*, 173–181. doi: 10.1016/j.epsl.2013.09.041

Iidaka, T., & Obara, K. (2013). Shear-wave splitting in a region with newly-activated seismicity after the 2011 tohoku earthquake. *Earth, Planets and Space*, *65*(9), 1059–1064. doi: 10.5047/eps.2013.02.003

Illsley-Kemp, F., Savage, M. K., Keir, D., Hirschberg, H. P., Bull, J. M., Gernon, T. M., ... Goitom, B. (2017). Extension and stress during continental breakup: Seismic anisotropy of the crust in Northern Afar. *Earth and Planetary Science Letters*, *477*, 41–51. doi: 10.1016/j.epsl.2017.08.014

Ito, H., DeVilbiss, J., & Nur, A. (1979). Compressional and shear waves in saturated rock during water-steam transition. *Journal of Geophysical Research*, *84*(B9), 4731. doi: 10.1029/jb084ib09p04731

Johnson, J. H., Savage, M. K., & Townend, J. (2011). Distinguishing between stress-induced and structural anisotropy at Mount Ruapehu volcano, New Zealand. *Journal of*

Geophysical Research, *116*. doi: 10.1029/2011JB008308

Kaiser, A., Balfour, N., Fry, B., Holden, C., Litchfield, N., Gerstenberger, M., & et al. (2017). The 2016 Kaikōura, New Zealand, Earthquake: Preliminary Seismological Report. *Seismological Research Letters*, *88*(3), 727–739. doi: 10.1785/0220170018

Karalliyadda, S. C., & Savage, M. K. (2013). Seismic anisotropy and lithospheric deformation of the plate-boundary zone in South Island, New Zealand: inferences from local S-wave splitting. *Geophysical Journal International*, *193*(2), 507-530. doi: 10.1093/gji/ggt022

Kisslinger, C., & Engdahl, E. (1973). The interpretation of the Wadati diagram with relaxed assumptions. *Bulletin of the Seismological Society of America*, *63*(5), 1723–1736.

Klosko, E. R., Wu, F. T., Anderson, H. J., Eberhart-Phillips, D., McEvilly, T. V., Audoine, E., ... Gledhill, K. R. (1999). Upper mantle anisotropy in the New Zealand Region. *Geophysical Research Letters*, *26*(10), 1497–1500. doi: 10.1029/1999gl900273

Kong, Q., Trugman, D. T., Ross, Z. E., Bianco, M. J., Meade, B. J., & Gerstoft, P. (2018). Machine Learning in Seismology: Turning Data into Insights. *Seismological Research Letters*, *90*(1), 3-14. doi: 10.1785/0220180259

Lamb, S., Arnold, R., & Moore, J. D. P. (2018). Locking on a megathrust as a cause of distributed faulting and fault-jumping earthquakes. *Nature Geoscience*, *11*(11), 871–875. doi: 10.1038/s41561-018-0230-5

Langridge, R., Ries, W., Litchfield, N., Villamor, P., Dissen, R. V., Barrell, D., ... Stirling, M. (2016). The New Zealand Active Faults Database. *New Zealand Journal of Geology and Geophysics*, *59*(1), 86–96. doi: 10.1080/00288306.2015.1112818

Lanza, F., Chamberlain, C. J., Jacobs, K., Warren-Smith, E., Godfrey, H. J., Kortink, M., ... Eberhart-Phillips, D. (2019). Crustal fault connectivity of the mw 7.8 2016 kaikōura earthquake constrained by aftershock relocations. *Geophysical Research Letters*, *46*(12), 6487-6496. doi: 10.1029/2019GL082780

Levin, V., & Park, J. (1997). P-SH conversions in a flat-layered medium with anisotropy of arbitrary orientation. *Geophysical Journal International*, 253–266.

Li, Y.-G., & Vidale, J. E. (2001). Healing of the shallow fault zone from 1994-1998 After the 1992 M7.5 Landers, California, Earthquake. *Geophysical Research Letters*, *28*(15), 2999–3002. doi: 10.1029/2001gl012922

Litchfield, N. J., Benson, A., Bischoff, A., Hatem, A., Wandres, A., & et. al. (2017). Multiple Fault Ground Surface Ruptures In The 14 November 2016 Kaikōura Earthquake, New

Zealand. *Seismological Research Letters*, *88*(2B), 624–626. doi: 10.1785/0220170035

Liu, Y. (2004). Systematic Analysis of Shear-Wave Splitting in the Aftershock Zone of the 1999 Chi-Chi, Taiwan, Earthquake: Shallow Crustal Anisotropy and Lack of Precursory Variations. *Bulletin of the Seismological Society of America*, *94*(6), 2330–2347. doi: 10.1785/0120030139

Lucente, F. P., Gori, P. D., Margheriti, L., Piccinini, D., Bona, M. D., Chiarabba, C., & Agostinetti, N. P. (2010). Temporal variation of seismic velocity and anisotropy before the 2009 MW6.3 L'Aquila earthquake, Italy. *Geology*, *38*(11), 1015–1018. doi: 10.1130/g31463.1

Matcham, I., Savage, M. K., & Gledhill, K. R. (2000). Distribution of seismic anisotropy in the subduction zone beneath the Wellington region, New Zealand. *Geophysical Journal International*, *140*(1), 1-10. doi: 10.1046/j.1365-246x.2000.00928.x

Michael, A. J. (1984). Determination of stress from slip data: Faults and folds. *Journal of Geophysical Research: Solid Earth*, *89*(B13), 11517-11526. doi: 10.1029/JB089iB13p11517

Miller, V., & Savage, M. (2001). Changes in seismic anisotropy after volcanic eruptions: evidence from Mount Ruapehu. *Science*, *293*(5538), 2231–2233.

Mitchell, J., Mackay, H. M. E. P. A., K.A.and Neil, & Notman, P. (2012). *New Zealand Region Bathymetry, 1:4,000000* (2nd Series No. 92 ed.). NIWA Chart.

Mortimer, N. (1993). Metamorphic zones, terranes, and Cenozoic faults in the Marlborough Schist, New Zealand. *New Zealand Journal of Geology and Geophysics*, *36*(3), 357–368. doi: 10.1080/00288306.1993.9514581

Mortimer, N. (2004). New Zealand's geological foundations. *Gondwana Research*, *7*(1), 261–272.

Neuberg, J., & Pointer, T. (2000). Effects of volcano topography on seismic broad-band waveforms. *Geophysical Journal International*, *143*(1), 239–248. doi: 10.1046/j.1365-246x.2000.00251.x

Nur, A. (1971). Effects of stress on velocity anisotropy in rocks with cracks. *Journal of Geophysical Research*, *76*(8), 2022–2034. doi: 10.1029/jb076i008p02022

Nuttli, O. (1961). The effect of the earth's surface on the S wave particle motion. *Bulletin of the Seismological Society of America*, *51*(2), 237.

Okada, T., Iio, Y., Matsumoto, S., Bannister, S., Ohmi, S., Horiuchi, S., ... Sibson, R. H. (2019). Comparative tomography of reverse-slip and strike-slip seismotectonic provinces

in the northern South Island, New Zealand. *Tectonophysics*, *765*, 172–186. doi: 10.1016/j.tecto.2019.03.016

Okaya, D., Christensen, N., Stanley, D., Stern, T., & (term), S. I. G. T. (1995). Crustal anisotropy in the vicinity of the Alpine Fault Zone, South Island, New Zealand. *New Zealand Journal of Geology and Geophysics*, *38*(4), 579–583. doi: 10.1080/00288306.1995.9514686

Okaya, D., Christensen, N. I., Ross, Z. E., & Wu, F. T. (2016). Terrane-controlled crustal shear wave splitting in Taiwan. *Geophysical Research Letters*, *43*(2), 556–563. doi: 10.1002/2015gl066446

Peng, Z., & Ben-Zion, Y. (2004). Systematic analysis of crustal anisotropy along the Karadere—Düzce branch of the North Anatolian fault. *Geophysical Journal International*, *159*(1), 253–274.

Peng, Z., & Ben-Zion, Y. (2005). Spatio-temporal variations of crustal anisotropy from similar events in aftershocks of the 1999 M7.4 Izmit and M7.1 Duzce, Turkey, earthquake sequences. *Geophys. J. Int.*, *160*, 1027–1043.

Petersen, T., Gledhill, K., Chadwick, M., Gale, N. H., & Ristau, J. (2011). The new zealand national seismograph network. *Seismological Research Letters*, *82*(1), 9–20. doi: 10.1785/gssrl.82.1.9

Pettinga, J., Yetton, M., Van Dissen, R., & Downes, G. (2001). Earthquake Source Identification and Characterisation for the Canterbury Region, South Island, New Zealand. *Bulletin of the New Zealand Society for Earthquake Engineering*, *34*(4), 282–317.

Piccinini, D., Margheriti, L., Chiaraluce, L., & Cocco, M. (2006). Space and time variations of crustal anisotropy during the 1997 Umbria-Marche, central Italy, seismic sequence. *Geophysical Journal International*, *167*(3), 1482–1490. doi: 10.1111/j.1365-246x.2006.03112.x

Reyners, M., & Cowan, H. (1993). The transition from subduction to continental collision: crustal structure in the North Canterbury region, New Zealand. *Geophysical Journal International*, *115*(3), 1124-1136. doi: 10.1111/j.1365-246X.1993.tb01514.x

Ristau, J. (2013). Update of Regional Moment Tensor Analysis for Earthquakes in New Zealand and Adjacent Offshore Regions. *Bulletin of the Seismological Society of America*, *103*(4), 2520–2533. doi: 10.1785/0120120339

Roman, D. C., Savage, M. K., Arnold, R., Latchman, J. L., & De Angelis, S. (2011). Analysis and forward modeling of seismic anisotropy during the ongoing eruption of the

Soufrière Hills Volcano, Montserrat, 1996–2007. *Journal of Geophysical Research: Solid Earth*, *116*(B3). doi: 10.1029/2010jb007667

Ross, Z. E., Meier, M., Hauksson, E., & Heaton, T. H. (2018). Generalized Seismic Phase Detection with Deep Learning. *Bulletin of the Seismological Society of America*, *108*(5A), 2894-2901. doi: 10.1785/0120180080

Rümpker, G., & Silver, P. G. (1998). Apparent shear-wave splitting parameters in the presence of vertically varying anisotropy. *Geophysical Journal International*, *135*(3), 790–800.

Saiga, A., Hiramatsu, Y., Ooida, T., & Yamaoka, K. (2003). Spatial variation in the crustal anisotropy and its temporal variation associated with a moderate-sized earthquake in the Tokai region, central Japan. *Geophysical Journal International*, *154*(3), 695–705. doi: 10.1046/j.1365-246x.2003.01998.x

Savage, M. (1999). Seismic anisotropy and mantle deformation: what have we learned from shear wave splitting? *Rev. Geophys.*, *37*, 65–106.

Savage, M., Aoki, Y., Unglert, K., Ohkura, T., Umakoshi, K., Shimizu, H., & et al. (2016). Stress, strain rate and anisotropy in Kyushu, Japan. *Earth and Planetary Science Letters*, *439*, 129–142. doi: 10.1016/j.epsl.2016.01.005

Savage, M., Ohminato, T., Aoki, Y., Tsuji, H., & Greve, S. M. (2010b). Stress magnitude and its temporal variation at Mt. Asama Volcano, Japan, from seismic anisotropy and GPS. *Earth and Planetary Science Letters*, *290*(3), 403 - 414. doi: 10.1016/j.epsl.2009.12.037

Savage, M., Shih, X., Meyer, R., & Aster, R. (1989). Shear-wave anisotropy of active tectonic regions via automated S-wave polarization analysis. *Tectonophysics*, *165*(1-4), 279–292. doi: 10.1016/0040-1951(89)90053-x

Savage, M., Wessell, A., Teanby, N., & Hurst, A. (2010a). Automatic measurement of shear wave splitting and applications to time varying anisotropy at Mount Ruapehu volcano, New Zealand. *Journal of Geophysical Research*, *115*, 115. doi: 10.1029/2010jb007722

Shih, X. R., & Meyer, R. P. (1990). Observation of shear wave splitting from natural events: South moat of long valley caldera, california, june 29 to august 12, 1982. *Journal of Geophysical Research: Solid Earth*, *95*(B7), 11179-11195. doi: 10.1029/JB095iB07p11179

Silver, P. G., & Chan, W. W. (1991). Shear wave splitting and subcontinental mantle deformation. *Journal of Geophysical Research: Solid Earth*, *96*(B10), 16429–16454.

Tadokoro, K., & Ando, M. (2002). Evidence for rapid fault healing derived from temporal

changes in S wave splitting. *Geophysical Research Letters*, *29*(4), 6-1-6-4. doi: 10.1029/2001gl013644

Tadokoro, K., Ando, M., & Umeda, Y. (1999). Swave splitting in the aftershock region of the 1995 Hyogo-ken Nanbu earthquake. *Journal of Geophysical Research: Solid Earth*, *104*(B1), 981–991. doi: 10.1029/1998jb900024

Takanami, T., & Kitagawa, G. (1988). A new efficient procedure for the estimation of onset times of seismic waves. *Journal of Physics of the Earth*, *36*(6), 267–290. doi: 10.4294/jpe1952.36.267

Teanby, N., Kendall, J.-M., Jones, R. H., & Barkved, O. (2004a). Stress-induced temporal variations in seismic anisotropy observed in microseismic data. *Geophysical Journal International*, *156*(3), 459–466. doi: 10.1111/j.1365-246x.2004.02212.x

Teanby, N., Kendall, J.-M., Jones, R. H., & Barkved, O. (2004b, April). Automation of Shear-Wave Splitting Measurements using Cluster Analysis. *Bulletin of the Seismological Society of America*, *94*(2), 453–463. doi: 10.1785/0120030123

Townend, J., Sherburn, S., Arnold, R., Boese, C., & Woods, L. (2012). Three-dimensional variations in present-day tectonic stress along the Australia–Pacific plate boundary in New Zealand. *Earth and Planetary Science Letters*, *353-354*, 47–59. doi: 10.1016/j.epsl.2012.08.003

Townend, J., & Zoback, M. D. (2000). How faulting keeps the crust strong. *Geology*, *28*(5), 399. doi: 10.1130/0091-7613(2000)28⟨399:hfktcs⟩2.0.co;2

Townend, J., & Zoback, M. D. (2001). Implications of earthquake focal mechanisms for the frictional strength of the San Andreas fault system. *Geological Society, London, Special Publications*, *186*(1), 13–21. doi: 10.1144/gsl.sp.2001.186.01.02

Unglert, K., Savage, M. K., Fournier, N., Ohkura, T., & Abe, Y. (2011). Shear wave splitting, Vp/Vs, and GPS during a time of enhanced activity at Aso caldera, Kyushu. *Journal of Geophysical Research: Solid Earth*, *116*(B11). doi: 10.1029/2011jb008520

Van Dissen, R., & Yeats, R. S. (1991). Hope fault, Jordan thrust, and uplift of the Seaward Kaikōura Range, New Zealand. *Geology*, *19*(4), 393. doi: 10.1130/0091-7613(1991)019⟨0393:HFJTAU⟩2.3.CO;2

Wadati, K., & Oki, S. (1933). On the Travel Time of Earthquake Waves. (Part II). *Journal of the Meteorological Society of Japan. Ser. II*, *11*(1), 14-28. doi: 10.2151/jmsj1923.11.1_14

Wallace, L. M., Kaneko, Y., Hreinsdóttir, S., Hamling, I., Peng, Z., & et al. (2017). Large-scale dynamic triggering of shallow slow slip enhanced by overlying sedimentary wedge.

Nature Geoscience, *10*(10), 765–770. doi: 10.1038/ngeo3021

Walsh, E. (2012). *Measuring shear wave splitting using the Silver and Chan method* (Unpublished master's thesis). Victoria University of Wellington.

Walsh, E., Arnold, R., & Savage, M. K. (2013). Silver and Chan revisited. *Journal of Geophysical Research: Solid Earth*, *118*(10), 5500–5515. doi: 10.1002/jgrb.50386

Wessel, P., Smith, W., Scharroo, R., Luis, J., & Wobbe, F. (2013). Generic Mapping Tools: Improved Version Released. *Eos, Transactions American Geophysical Union*, *94*(45), 409-410. doi: 10.1002/2013EO450001

Wilson, C. K., Jones, C. H., Molnar, P., Sheehan, A. F., & Boyd, O. S. (2004). Distributed deformation in the lower crust and upper mantle beneath a continental strike-slip fault zone: Marlborough fault system, south island, new zealand. *Geology*, *32*(10), 837. doi: 10.1130/g20657.1

Yang, Z., Sheehan, A., & Shearer, P. (2011). Stress-induced upper crustal anisotropy in southern California. *Journal of Geophysical Research: Solid Earth*, *116*(B2), 1–11. doi: 10.1029/2010JB007655

Zal, H. J., Jacobs, K., Savage, M. K., Yarce, J., Mroczek, S., Graham, K., ... Henrys, S. (2020). Temporal and spatial variations in seismic anisotropy and Vp/Vs ratios in a region of slow slip. *Earth and Planetary Science Letters*, *532*, 115970. doi: 10.1016/j.epsl.2019.115970

Zhang, H., Liu, Y., Thurber, C., & Roecker, S. (2007). Three-dimensional shear-wave splitting tomography in the Parkfield, California, region. *Geophysical Research Letters*, *34*(24). doi: 10.1029/2007GL031951

Zheng, X.-F., Chen, C.-H., & Zhang, C.-H. (2008). Study on Temporal Variations of Shear-Wave Splitting in the Chiayi Area, Aftershock Zone of 1999 Chichi Earthquake, Taiwan. *Chinese Journal of Geophysics*, *51*(1), 115–124. doi: 10.1002/cjg2.1200

Zietlow, D. W., Sheehan, A. F., Molnar, P. H., Savage, M. K., Hirth, G., Collins, J. A., & Hager, B. H. (2014). Upper mantle seismic anisotropy at a strike-slip boundary: South Island, New Zealand. *Journal of Geophysical Research: Solid Earth*, *119*(2), 1020–1040. doi: 10.1002/2013jb010676

Zinke, J. C. (2000). Structure-Related and Stress-Induced Shear-Wave Velocity Anisotropy: Observations from Microearthquakes near the Calaveras Fault in Central California. *Bulletin of the Seismological Society of America*, *90*(5), 1305–1312. doi: 10.1785/0119990099

Zoback, M. D., & Zoback, M. L. (2002). Stress in the earth's lithosphere. In *Encyclopedia*

of physical science and technology (3rd ed., Vol. 16, pp. 1221–1232). Kluwer Academic Publishers.

Supporting Information for "Spatio-temporal Analysis of Seismic Anisotropy Associated with the Cook Strait and Kaikōura Earthquake Sequences in New Zealand"

Kenny M. Graham[1], Martha K. Savage[1], Richard Arnold[2], Hubert J. Zal[1], Tomomi Okada[3], Yoshihisa Iio[4], Satoshi Matsumoto[5]

[1]Institute of Geophysics, SGEES, VUW, New Zealand
[2]School of Mathematics and Statistics, VUW, New Zealand
[3]Graduate School of Science, Tohoku University, Sendai, Japan
[4]Disaster Prevention Research Institute, Kyoto University, Uji, Japan
[5]Faculty of Sciences, Kyushu University, Shimabara, Japan

Contents

Table S1. Summary of adjusted parameters used for picking S-arrivals. Descriptions are after Castellazzi et al. (2015) and Diehl et al. (2009)

Parameter	Description	Value[1]	Value[2]
Common parameters			
Δ_{epi}^{max}	Maximum epicentral distance	250 km	150 km
Δ_{s_n}	Distance above which Sn is expected as first arrival	200 km	100 km
Δ_{V_p/V_s}	Expected V_p/V_s window (min, mean, max)	1.5, 1.8, 2.1	1.5, 1.73, 2.05
Filter	1: Wood-Anderson, 2: High-Pass 0.5 Hz, 3: 1&2	3	1
STA-LTA detector parameters			
Θ_{st}	Window length of short-term-average	0.15 (sec)	0.2 (sec)
Θ_{lt}	Window length of long-term-average	2 (sec)	2.5 (sec)
Θ_{thres}	Maximum post S-predicted time threshold	3 (sec)	4 (sec)
Parameters for AR–AIC Picker			
Δ_{AR-AIC}	Distance above which predicted S is used for configuration	150 km	100 km
Parameters for Quality Assessment			
$\Delta_{AIC_{pick}}$	Distance above which AR-AIC pick is considered quality	70 km	50 km
$SN_{min}^{0,0}$ (0)	Class 0 error classification (MaxErr, MinS2N, MaxS2N)	0.3, 3, 3	0.3, 3, 3
$SN_{min}^{1,1}$ (1)	Class 0 error classification (MaxErr, MinS2N, MaxS2N)	0.5, 3, 2	0.4, 3, 2

These Values[1] are calibrated parameters for Marlborough and Wellington regions that yielded more picks and small time differences between manual and Spicker picks. Value[2] are values used by Castellazzi et al. (2015) for Ruapehu region. S2N represents signal to noise ratio.

Corresponding author: Kenny M. Graham, Kenny.Graham@vuw.ac.nz

manuscript to be submitted to *Geophysical Journal International*

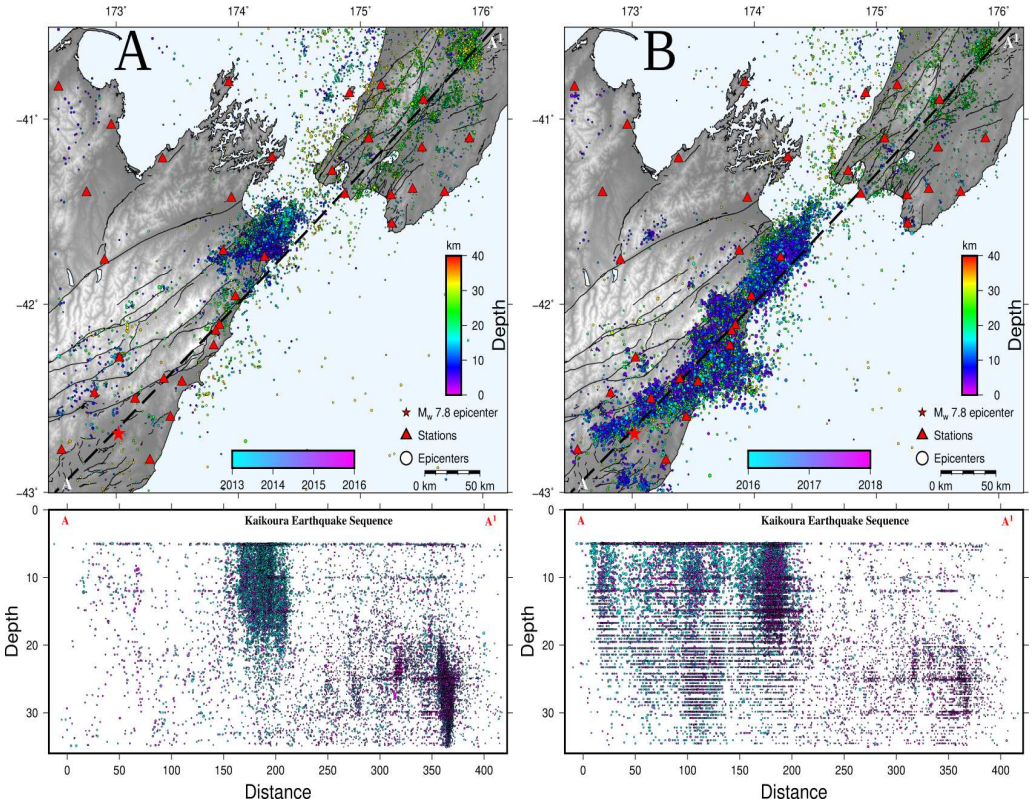

Figure S1. Map of events (A) before and (B) after the 2016 Kaikōura earthquake: Map view with epicenters of earthquakes before (left) and after (right) the M_w 7.8 Kaikōura Earthquake. Red star shows the M_w 7.8 epicenter with the red triangles showing the GeoNet stations in the region. Events are scaled according to their magnitude, and colour coded according to their depth. A cross-section from A to A^1 shows the depth distribution and colored by time (time scale on main Figure).

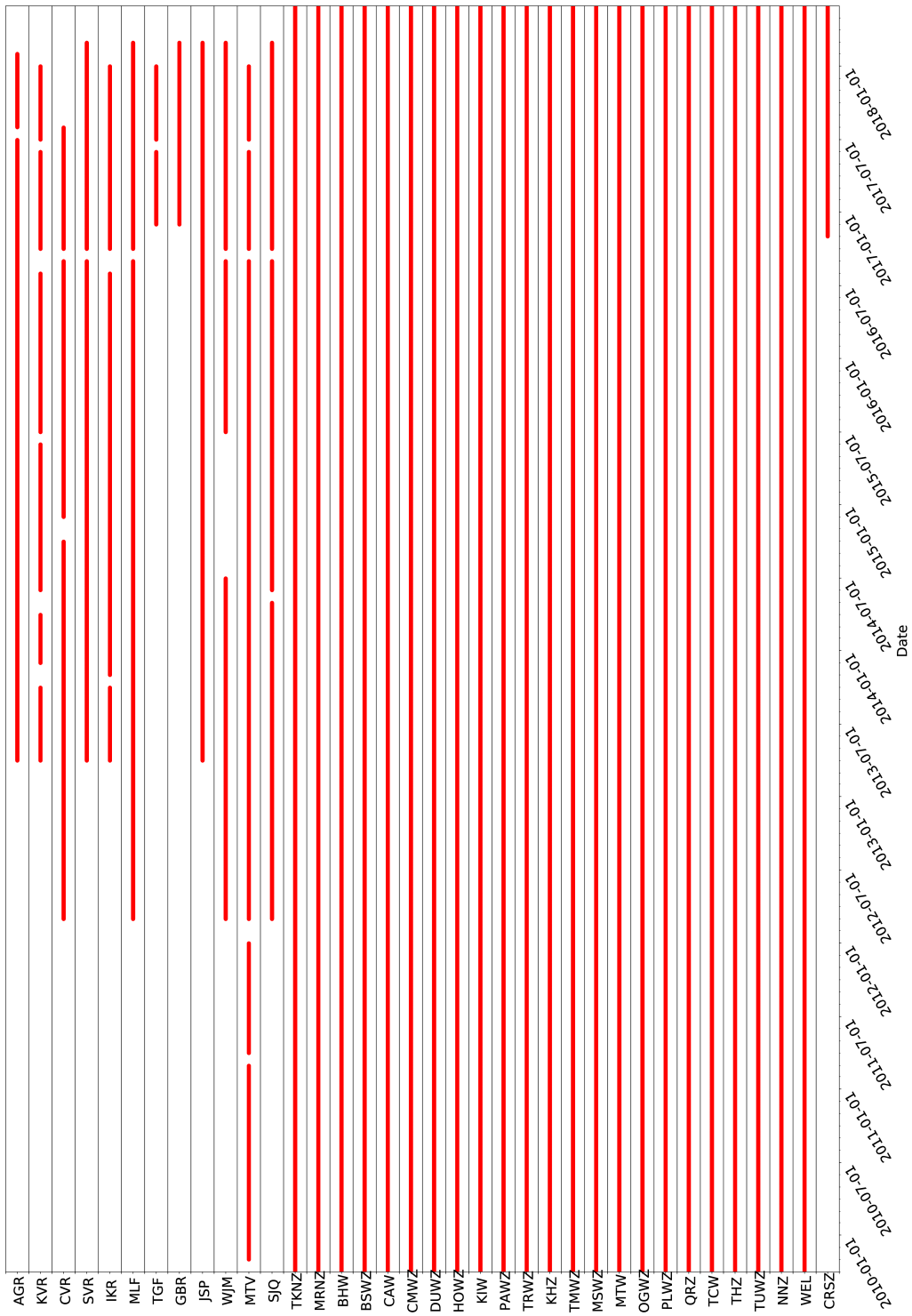

Figure S2. Plot of data continuity for all stations used for analysis over the five and half year period. Red bars show the period during which each station was operational.

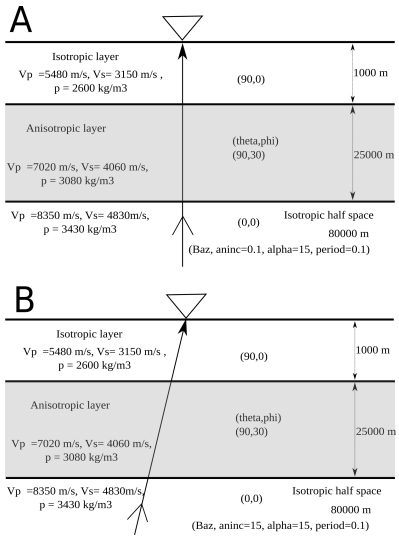

Figure S3. 1-D models used in the analysis. The model consists of an anisotropic layer atop isotropic layers. p = density, V_p and V_s are P and S velocity respectively. Theta and phi defines the axis of symmetry. Model A is the baseline model. In model B, we test the effect of incidence angle on splitting results. We used 1-D reflectivity codes Levin & Park (1997) for the waveform simulation in 1-D anisotropic media and MFAST was used to estimate SWS parameters.

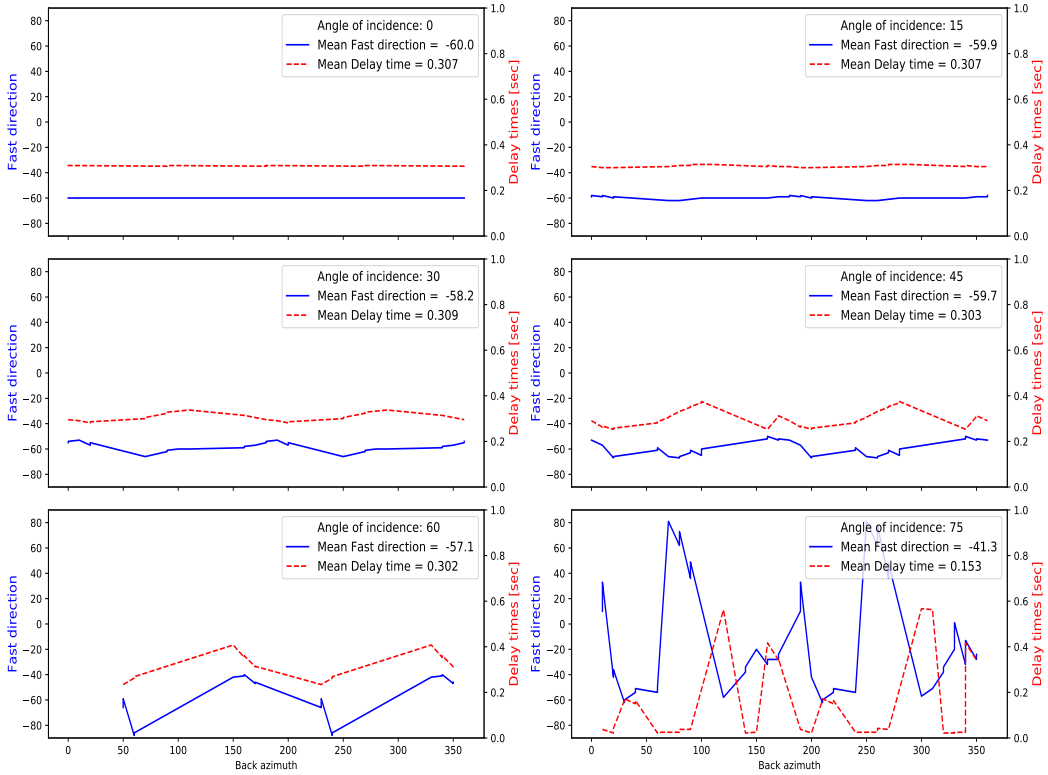

Figure S4. Comparison of apparent splitting parameters as a function of back-azimuth ranging from 0° to 360° with 5° increments. As angle of incidence is increased, there is more variation in δt and ϕ with varying back-azimuth. This is because phase conversion, at high angles, may interfere with SWS measurements.

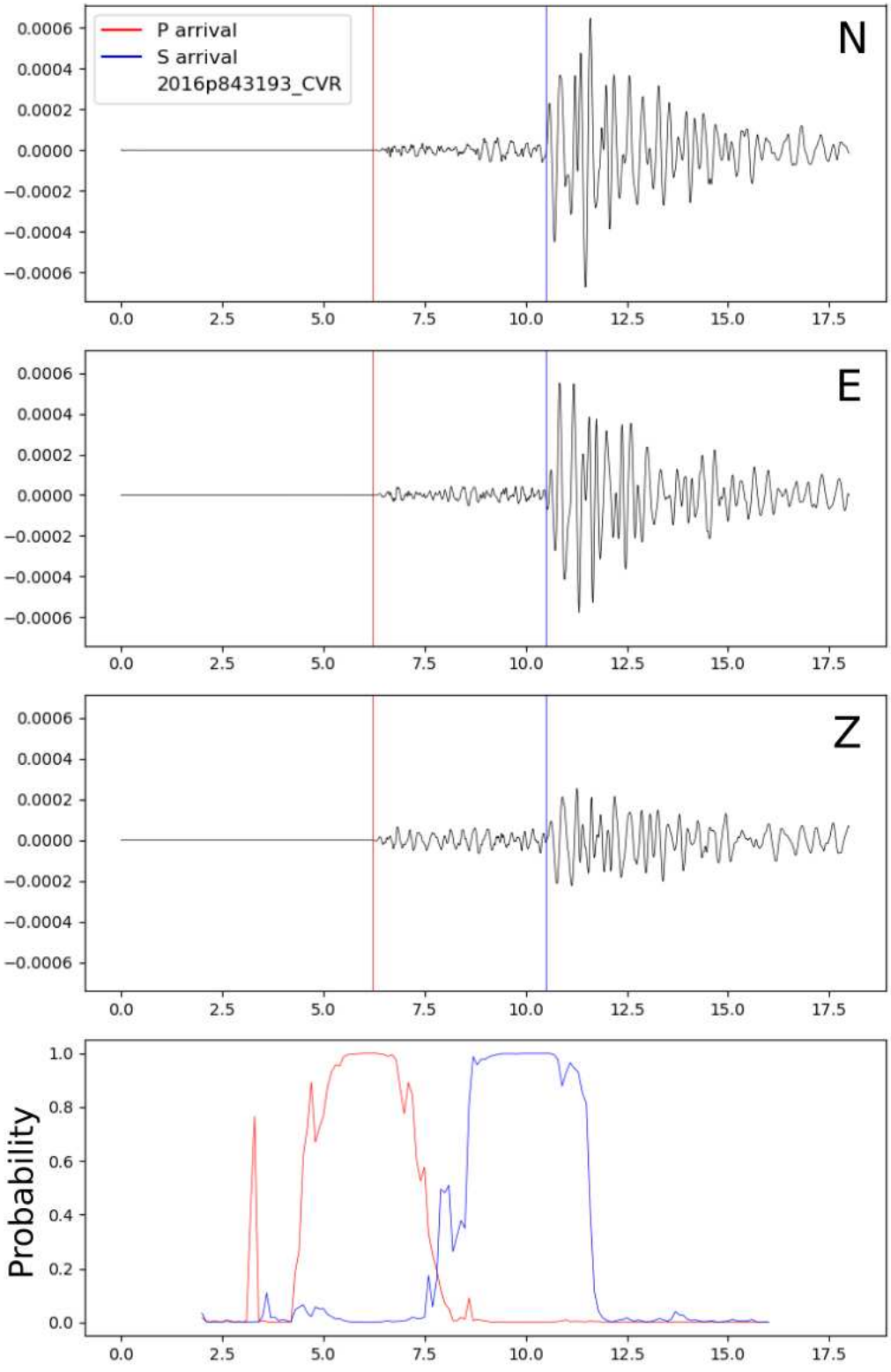

Figure S5. Example of generalized phase detection GPD pick. The red and blue colors indicate the probability of P and S waves, respectively. The vertical bars are estimated picks. This is an example of a reliable P- and S-pick for station CVR.

manuscript to be submitted to *Geophysical Journal International*

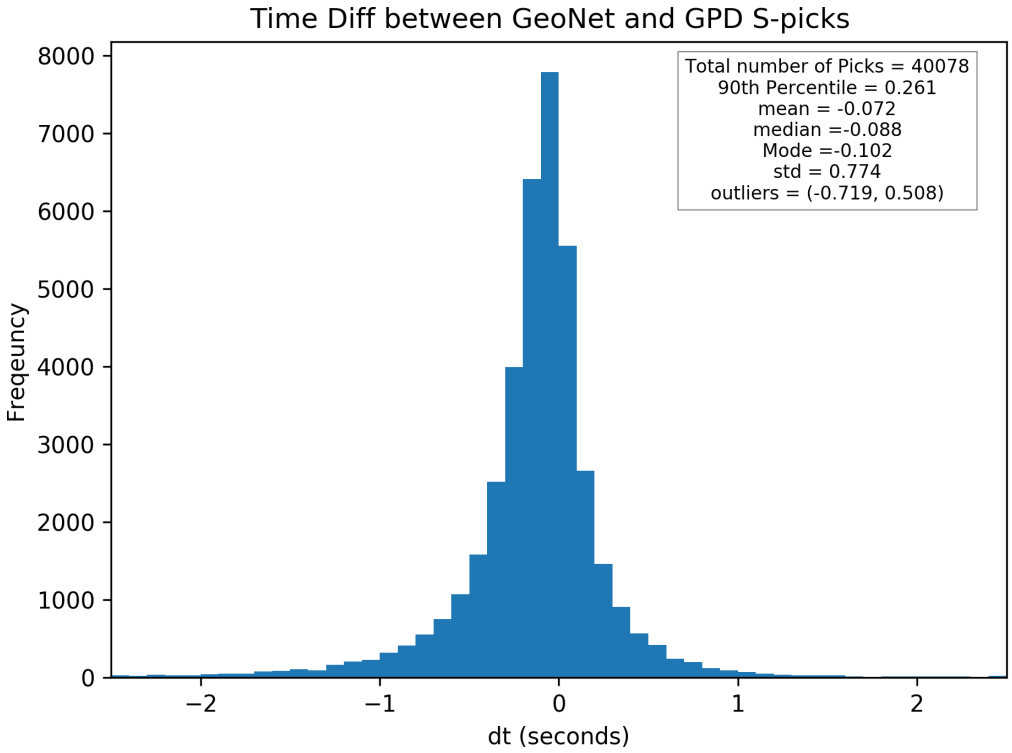

Figure S6. Distributions of time difference between GeoNet manual S-picks and GDP S-picks. The distribution in normally distributed with mean -0.072 and standard deviation 0.774

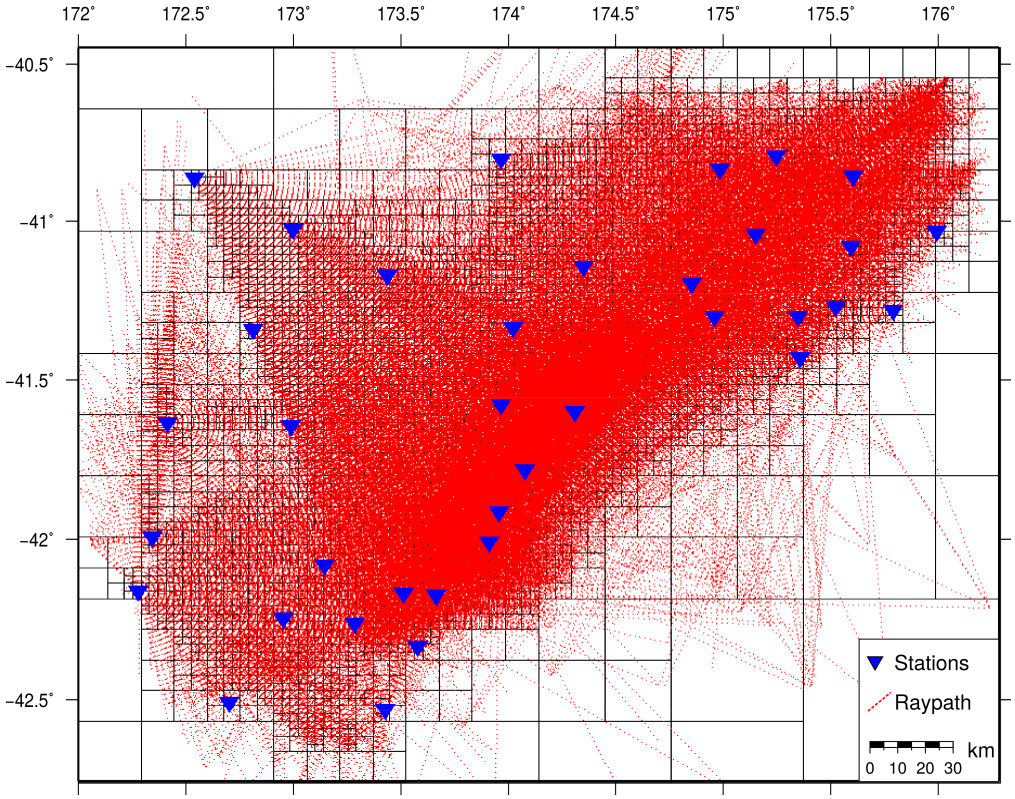

Figure S7. Study area is divided into grid cell using quadtree gridding. Red lines show raypaths, and blue triangles are seismic stations. For each grid, a minimum of 20 and maximum of 80 raypaths pass through each grid cell, with a minimum grid size of 5×5 km

manuscript to be submitted to *Geophysical Journal International*

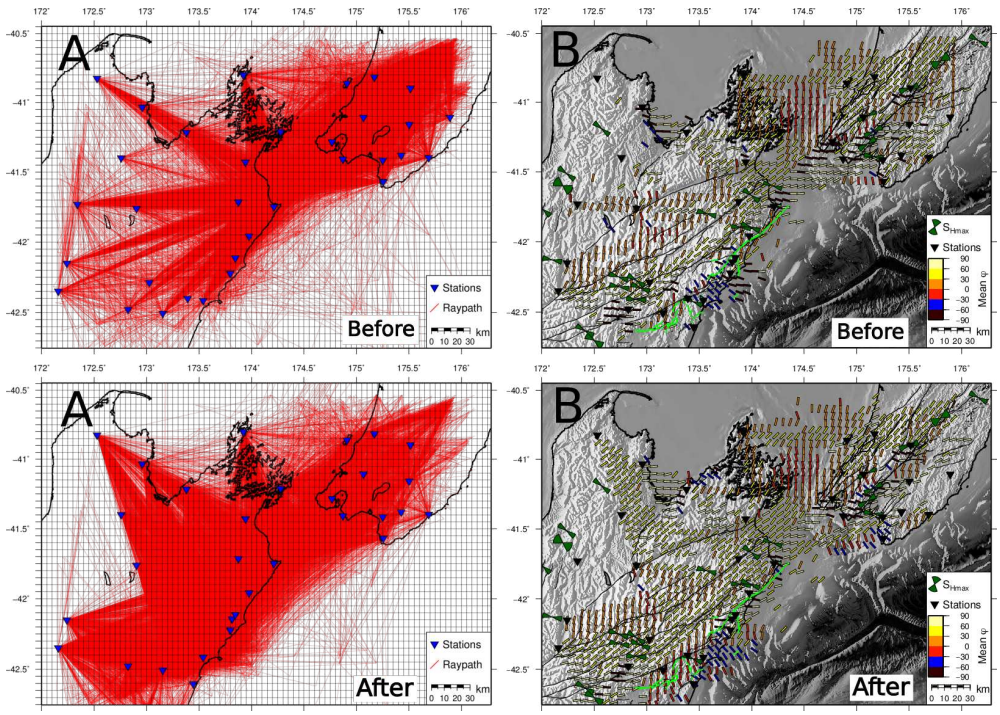

Figure S8. Spatial averaging results of ϕ for before (top row) and after (bottom row) measurements. A: Study area is divided into grid cell using quadtree gridding. Red lines show raypaths, and blue inverted triangles are seismic stations. A minimum of 20 and maximum of 80 raypaths passing through each block, with a minimum block size of 5 km are the criteria used for gridding. B: Spatial averages with weighting inversely proportional to the square of the distance from the station. The coloured bars show the mean in each grid. Green line are the fault lines that ruptured during the Kaikōura main-shock.

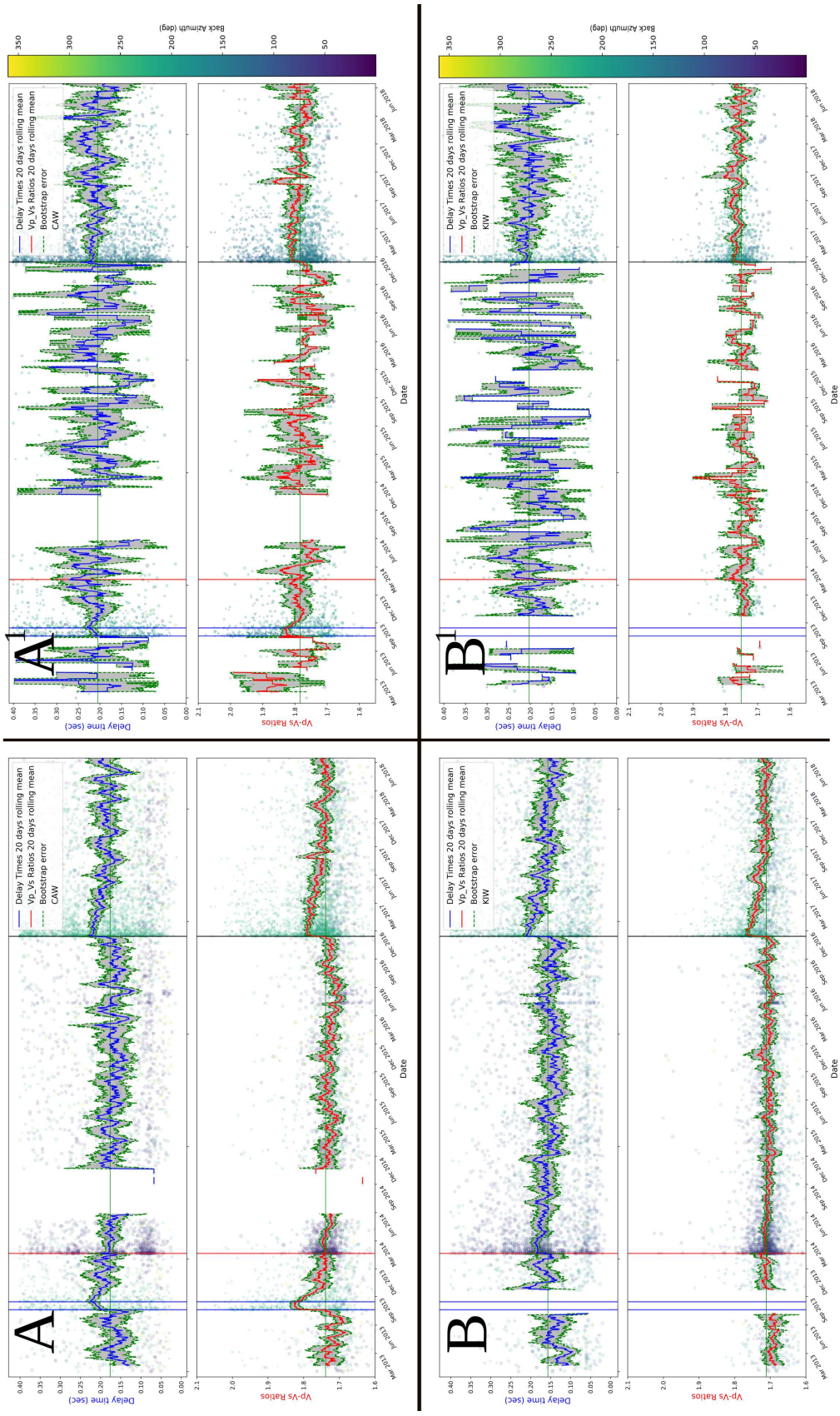

Figure S9. Time series of delay times, δt and V_p/V_s ratio for values from January, 2013 to June, 2018 is shown in each panel. A and A^1 are plots for all and clustered measurements for station CAW respectively. Similarly, B and B^1 are plots for station KIW. Blue, red and orange vertical bars represent the mainshock of Seddon, Eketahuna and Kaikōura earthquake, respectively. Green horizontal line shows the median value. Green dashed line represents the estimated error using bootstrap. Red and blue lines are the 20 day moving median of V_p/V_s ratio and δt, respectively.

manuscript to be submitted to *Geophysical Journal International*

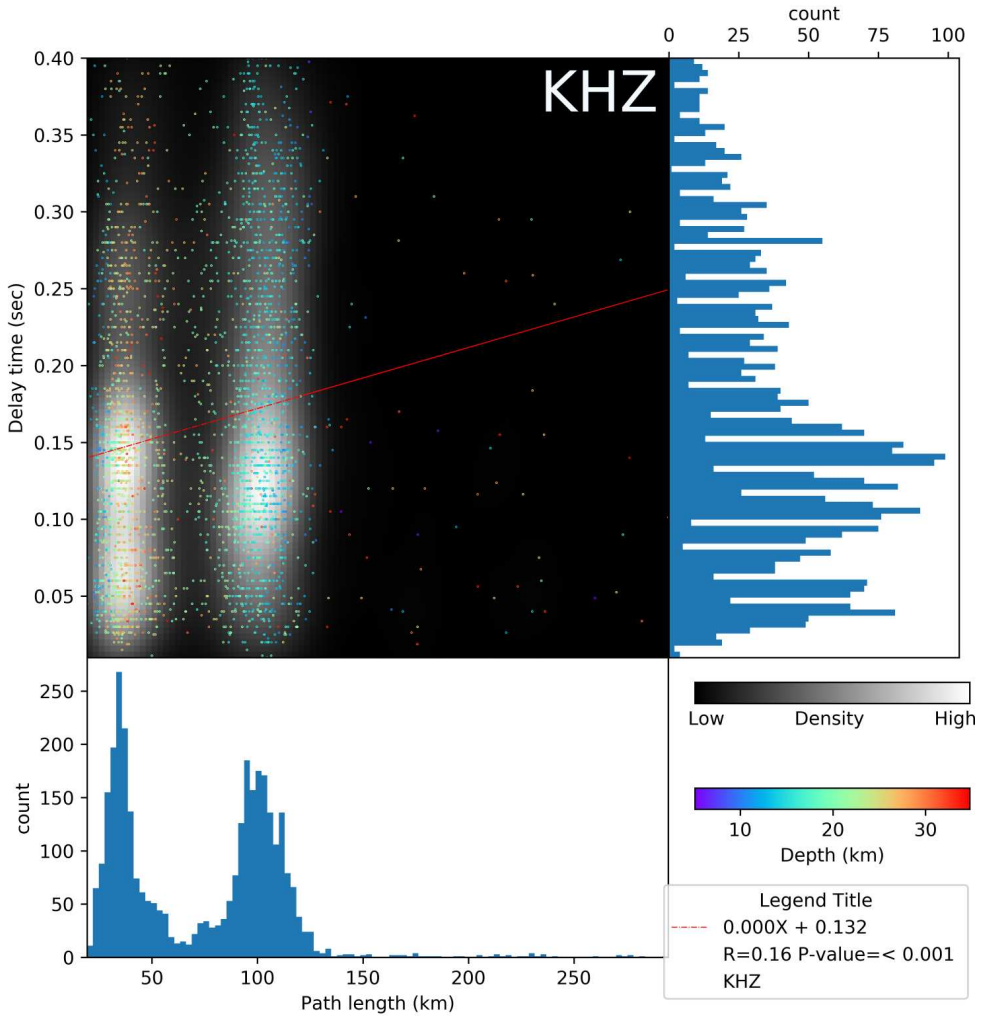

Figure S10. Delay times versus path length for station KHZ. Distribution of the delay time and path length are plotted on the right and bottom respectively. The scattered points are coloured by the depths and plotted on a basemap of the kernel density (effectively heatmap). High density regions are shaded white with low regions black. The red line is the least square regression line with the equation and p-value displayed on the lower right corner of each plot.

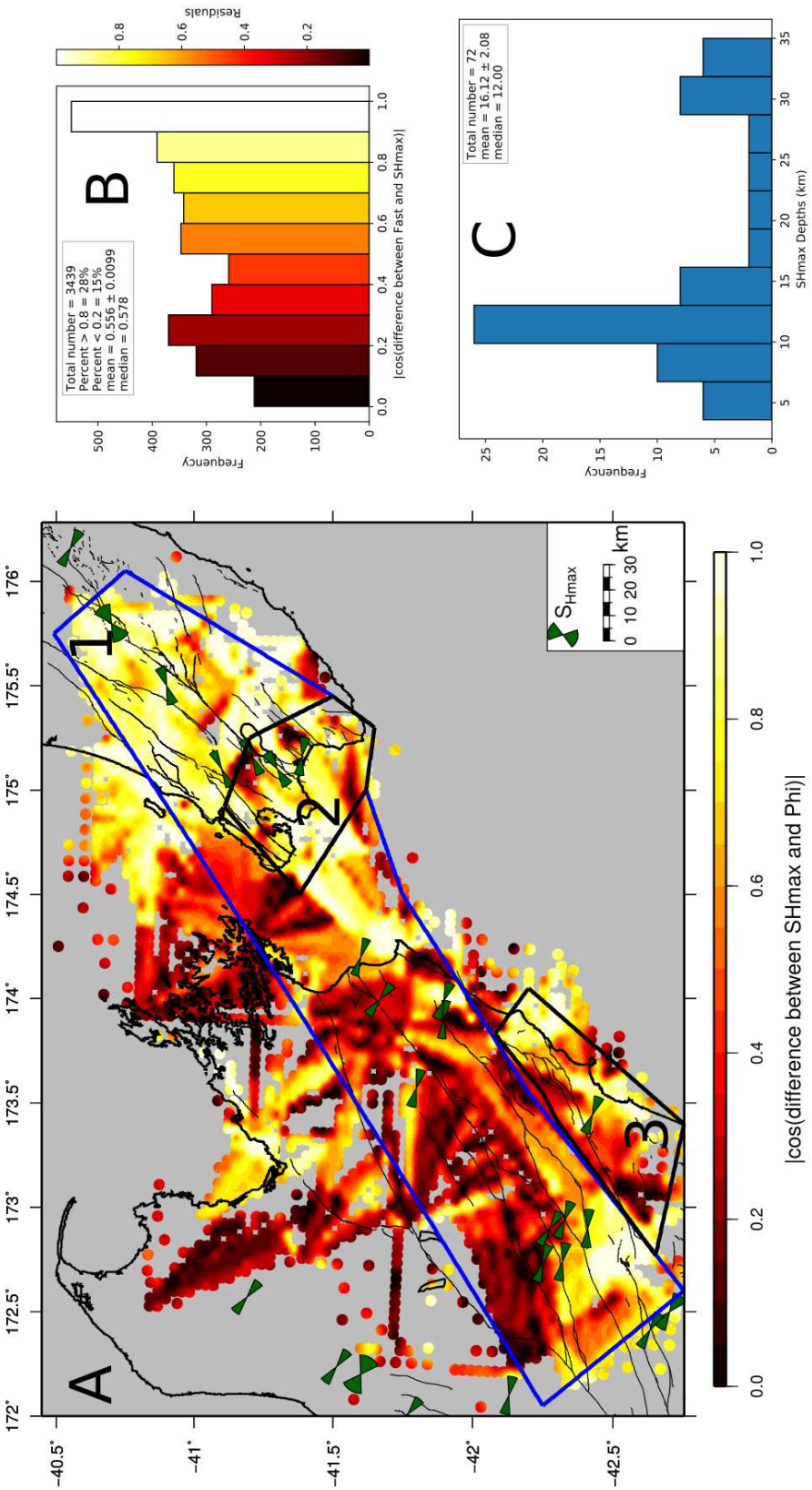

Figure S11. Quantitative comparison between spatially averaged ϕ measurements and the orientation of the closest (<30km) S_{Hmax}. The background colour is a contour of the absolute value of the cosine of the difference between the orientations, coloured by the scale at the bottom. Note that 1 represents no difference between the orientations. The descriptive statistics of the difference between orientations at the closest grid points is displayed on the histogram in B. S_{Hmax} are represented by dark green bow ties. The histogram of the S_{Hmax} depths used for analysis is shown in C.

References

Castellazzi, C., Savage, M., Walsh, E., & Arnold, R. (2015). Shear wave automatic picking and splitting measurements at Ruapehu volcano, New Zealand. *Journal of Geophysical Research: Solid Earth*, *120*, 3363–3384.

Diehl, T., Deichmann, N., Kissling, E., & Husen, S. (2009). Automatic S-Wave Picker for Local Earthquake Tomography. *Bulletin of the Seismological Society of America*, *99*(3), 1906–1920. doi: 10.1785/0120080019

Levin, V., & Park, J. (1997). P-SH conversions in a flat-layered medium with anisotropy of arbitrary orientation. *Geophysical Journal International*, 253–266.

manuscript to be submitted to *Geophysical Journal International*

Supporting Information for

"Spatio-temporal Analysis of Seismic Anisotropy Associated with the Cook Strait and Kaikōura Earthquake Sequences in New Zealand"

Kenny M. Graham[1], Martha K. Savage[1], Richard Arnold[2], Hubert J. Zal[1], Tomomi Okada[3], Yoshihisa Iio[4], Satoshi Matsumoto[5]

[1]Institute of Geophysics, SGEES, VUW, New Zealand
[2]School of Mathematics and Statistics, VUW, New Zealand
[3]Graduate School of Science, Tohoku University, Sendai, Japan
[4]Disaster Prevention Research Institute, Kyoto University, Uji, Japan
[5]Faculty of Sciences, Kyushu University, Shimabara, Japan

Contents

Table S1. Summary of adjusted parameters used for picking S-arrivals. Descriptions are after Castellazzi et al. (2015) and Diehl et al. (2009)

Parameter	Description	Value[1]	Value[2]
Common parameters			
Δ_{epi}^{max}	Maximum epicentral distance	250 km	150 km
Δ_{s_n}	Distance above which Sn is expected as first arrival	200 km	100 km
Δ_{V_p/V_s}	Expected V_p/V_s window (min, mean, max)	1.5, 1.8, 2.1	1.5, 1.73, 2.05
Filter	1: Wood-Anderson, 2: High-Pass 0.5 Hz, 3: 1&2	3	1
STA-LTA detector parameters			
Θ_{st}	Window length of short-term-average	0.15 (sec)	0.2 (sec)
Θ_{lt}	Window length of long-term-average	2 (sec)	2.5 (sec)
Θ_{thres}	Maximum post S-predicted time threshold	3 (sec)	4 (sec)
Parameters for AR–AIC Picker			
Δ_{AR-AIC}	Distance above which predicted S is used for configuration	150 km	100 km
Parameters for Quality Assessment			
$\Delta_{AIC_{pick}}$	Distance above which AR-AIC pick is considered quality	70 km	50 km
$SN_{min}^{0,0}$ (0)	Class 0 error classification (MaxErr, MinS2N, MaxS2N)	0.3, 3, 3	0.3, 3, 3
$SN_{min}^{1,1}$ (1)	Class 0 error classification (MaxErr, MinS2N, MaxS2N)	0.5, 3, 2	0.4, 3, 2

These Values[1] are calibrated parameters for Marlborough and Wellington regions that yielded more picks and small time differences between manual and Spicker picks. Value[2] are values used by Castellazzi et al. (2015) for Ruapehu region. S2N represents signal to noise ratio.

Corresponding author: Kenny M. Graham, Kenny.Graham@vuw.ac.nz

manuscript to be submitted to *Geophysical Journal International*

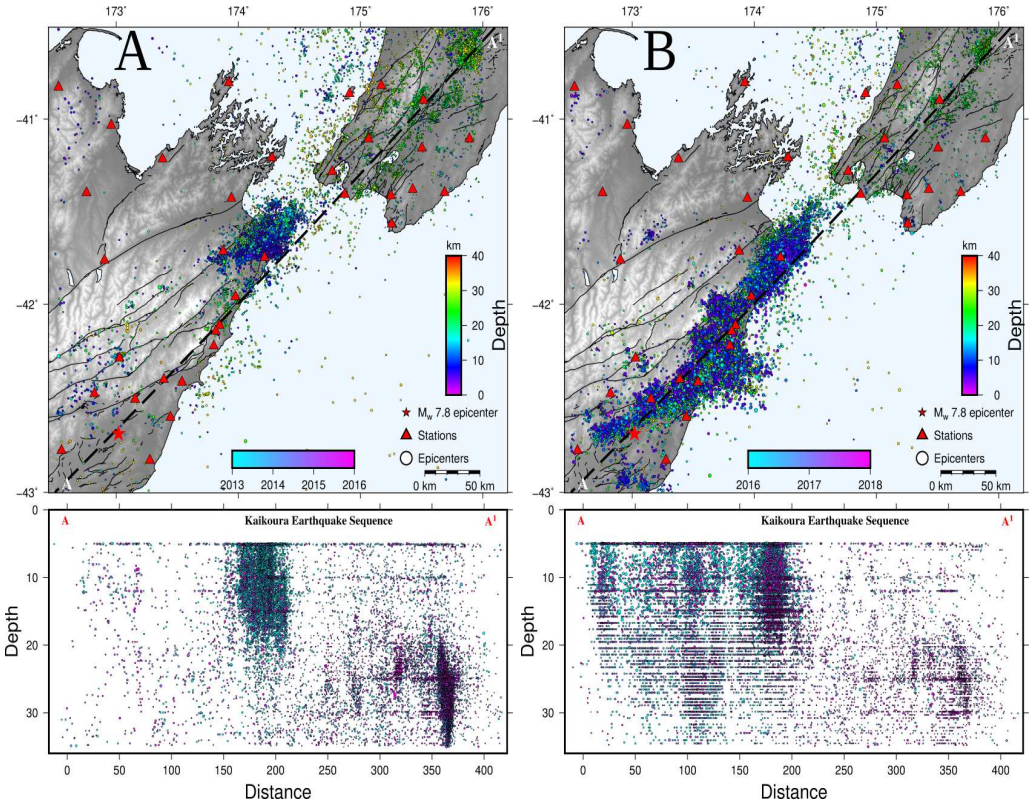

Figure S1. Map of events (A) before and (B) after the 2016 Kaikōura earthquake: Map view with epicenters of earthquakes before (left) and after (right) the M_w 7.8 Kaikōura Earthquake. Red star shows the M_w 7.8 epicenter with the red triangles showing the GeoNet stations in the region. Events are scaled according to their magnitude, and colour coded according to their depth. A cross-section from A to A^1 shows the depth distribution and colored by time (time scale on main Figure).

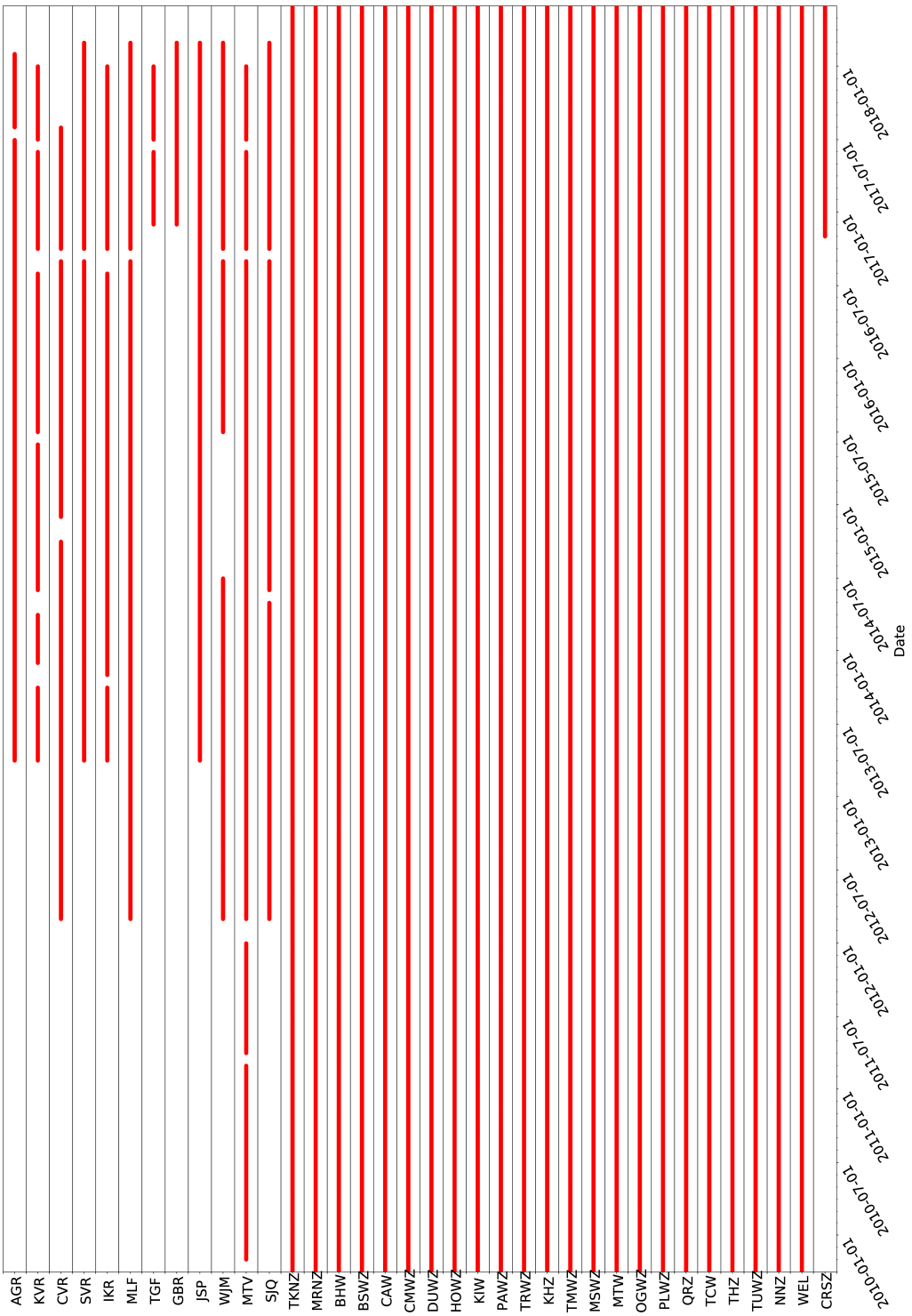

Figure S2. Plot of data continuity for all stations used for analysis over the five and half year period. Red bars show the period during which each station was operational.

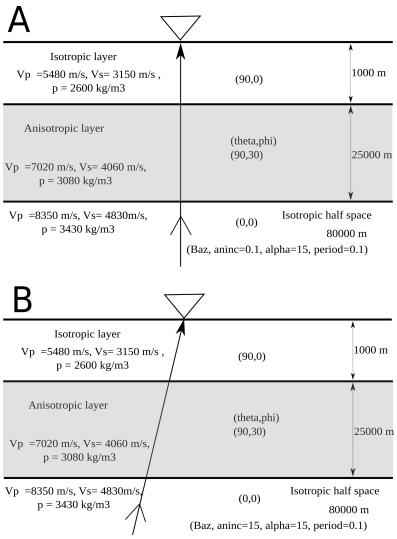

Figure S3. 1-D models used in the analysis. The model consists of an anisotropic layer atop isotropic layers. p = density, V_p and V_s are P and S velocity respectively. Theta and phi defines the axis of symmetry. Model A is the baseline model. In model B, we test the effect of incidence angle on splitting results. We used 1-D reflectivity codes Levin & Park (1997) for the waveform simulation in 1-D anisotropic media and MFAST was used to estimate SWS parameters.

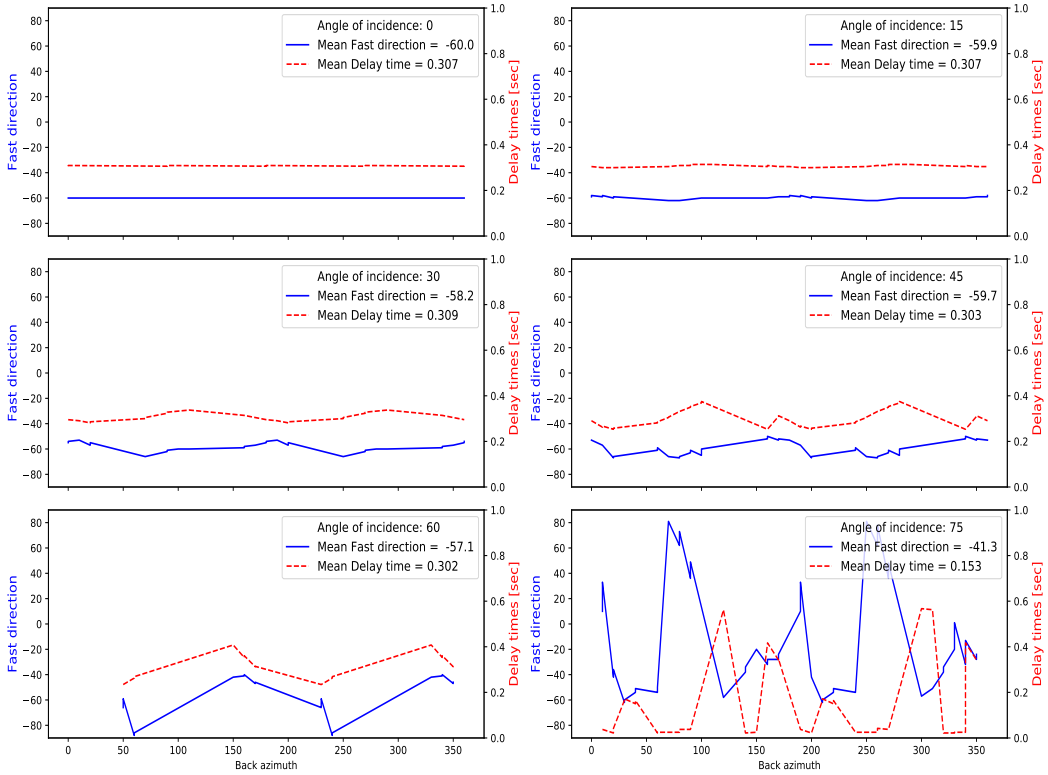

Figure S4. Comparison of apparent splitting parameters as a function of back-azimuth ranging from 0° to 360° with 5° increments. As angle of incidence is increased, there is more variation in δt and ϕ with varying back-azimuth. This is because phase conversion, at high angles, may interfere with SWS measurements.

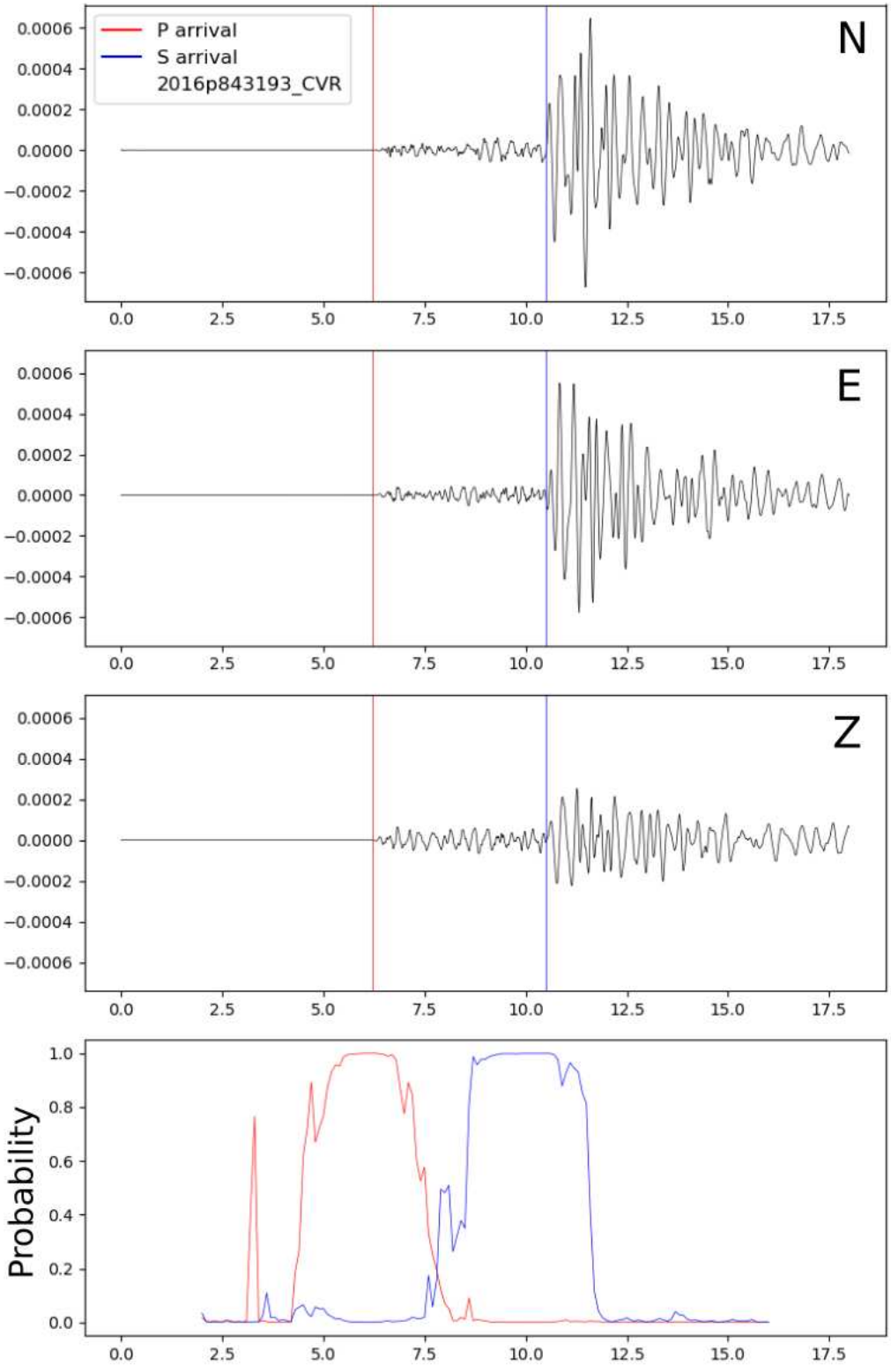

Figure S5. Example of generalized phase detection GPD pick. The red and blue colors indicate the probability of P and S waves, respectively. The vertical bars are estimated picks. This is an example of a reliable P- and S-pick for station CVR.

manuscript to be submitted to *Geophysical Journal International*

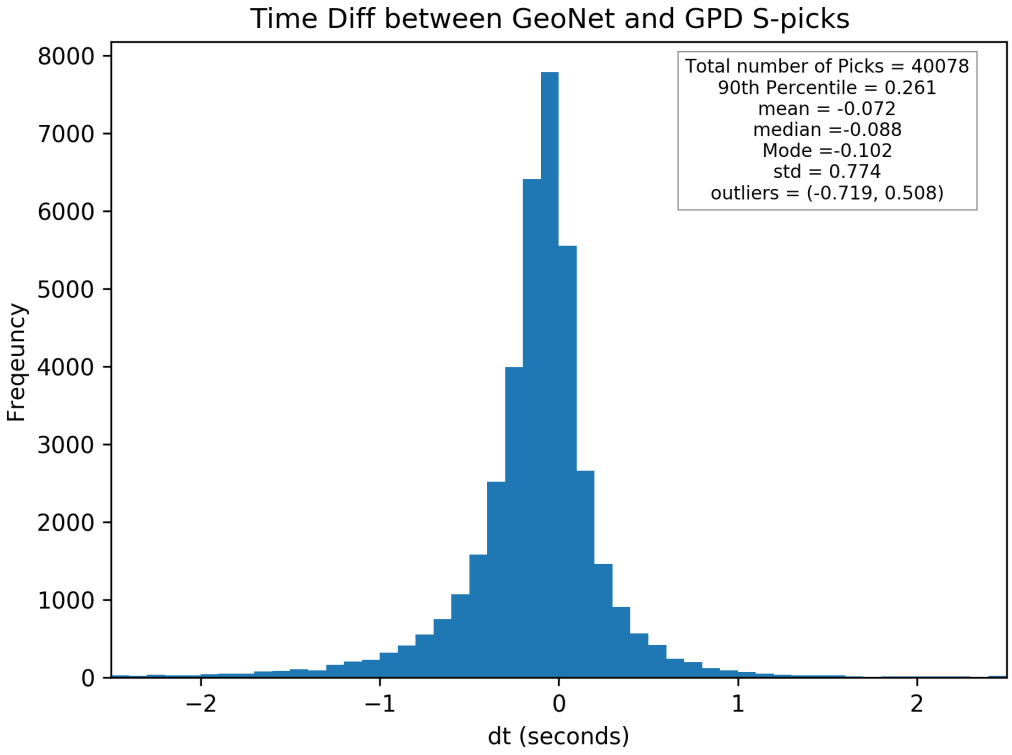

Figure S6. Distributions of time difference between GeoNet manual S-picks and GDP S-picks. The distribution in normally distributed with mean -0.072 and standard deviation 0.774

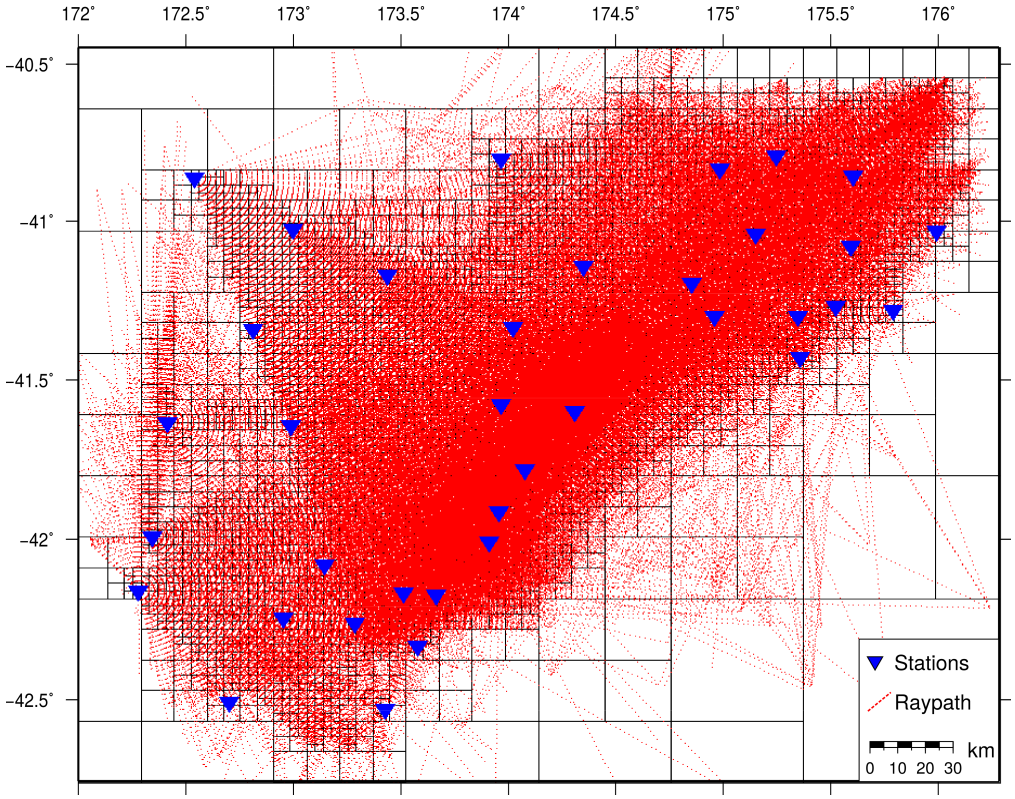

Figure S7. Study area is divided into grid cell using quadtree gridding. Red lines show raypaths, and blue triangles are seismic stations. For each grid, a minimum of 20 and maximum of 80 raypaths pass through each grid cell, with a minimum grid size of 5×5 km

manuscript to be submitted to *Geophysical Journal International*

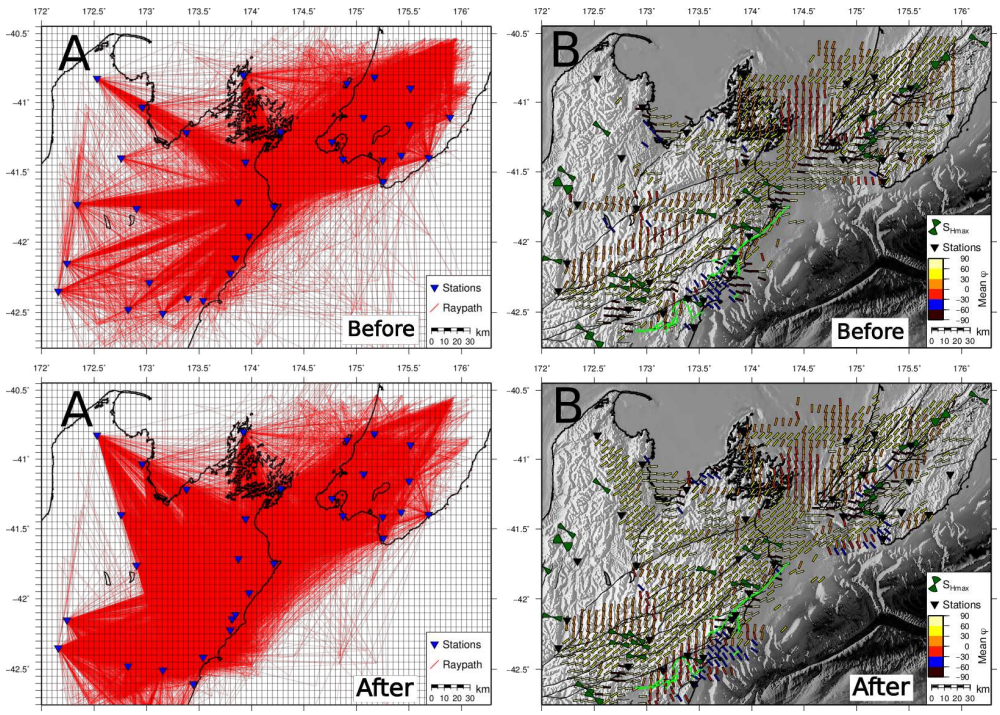

Figure S8. Spatial averaging results of ϕ for before (top row) and after (bottom row) measurements. A: Study area is divided into grid cell using quadtree gridding. Red lines show raypaths, and blue inverted triangles are seismic stations. A minimum of 20 and maximum of 80 raypaths passing through each block, with a minimum block size of 5 km are the criteria used for gridding. B: Spatial averages with weighting inversely proportional to the square of the distance from the station. The coloured bars show the mean in each grid. Green line are the fault lines that ruptured during the Kaikōura main-shock.

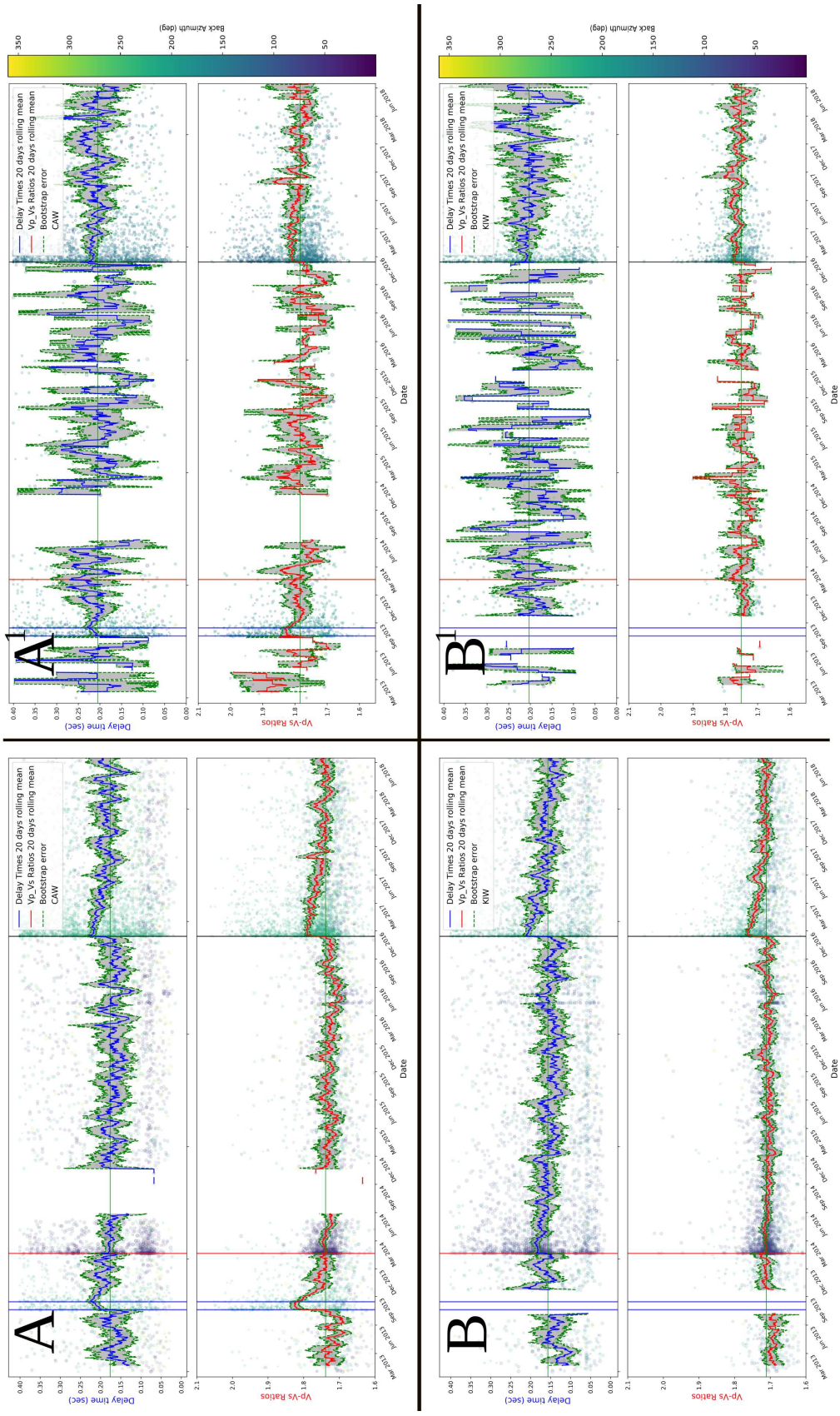

Figure S9. Time series of delay times, δt and V_p/V_s ratio for values from January, 2013 to June, 2018 is shown in each panel. A and A^1 are plots for all and clustered measurements for station CAW respectively. Similarly, B and B^1 are plots for station KIW. Blue, red and orange vertical bars represent the mainshock of Seddon, Eketahuna and Kaikōura earthquake, respectively. Green horizontal line shows the median value. Green dashed line represents the estimated error using bootstrap. Red and blue lines are the 20 day moving median of V_p/V_s ratio and δt, respectively.

manuscript to be submitted to *Geophysical Journal International*

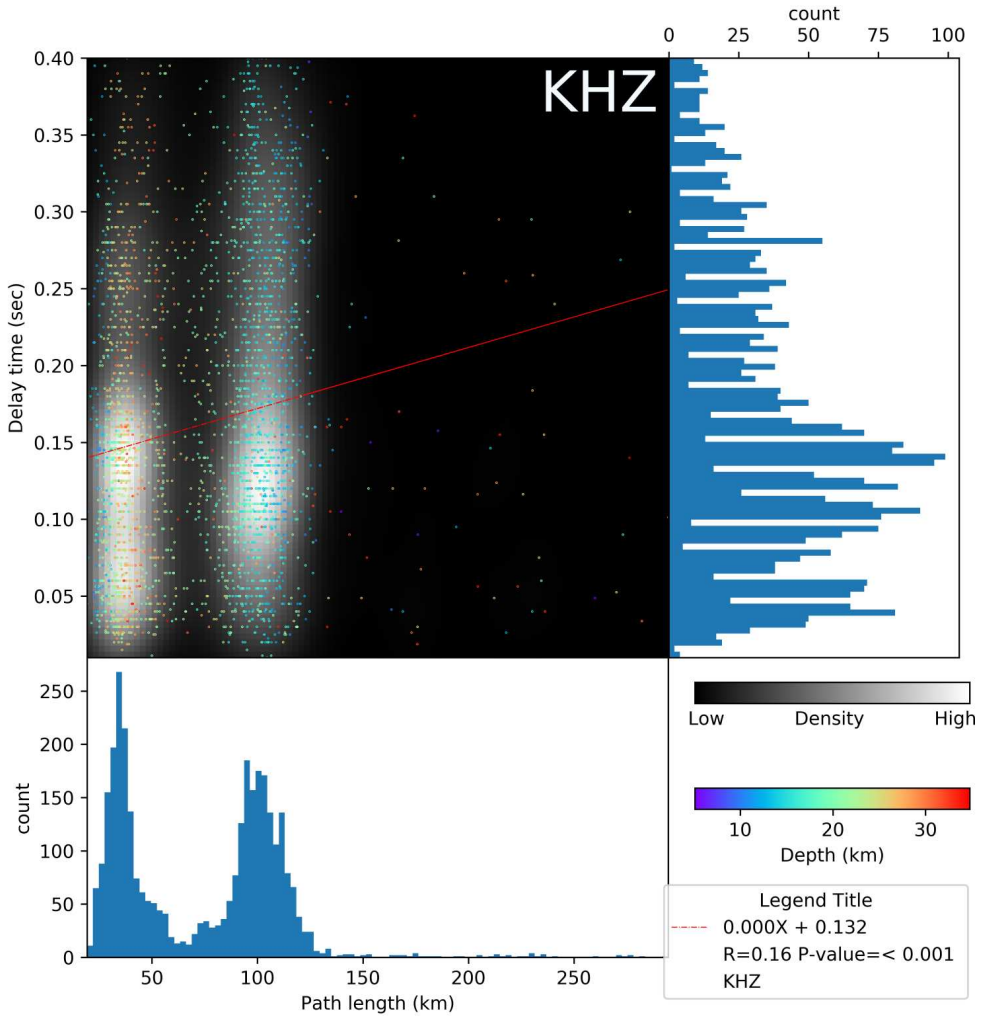

Figure S10. Delay times versus path length for station KHZ. Distribution of the delay time and path length are plotted on the right and bottom respectively. The scattered points are coloured by the depths and plotted on a basemap of the kernel density (effectively heatmap). High density regions are shaded white with low regions black. The red line is the least square regression line with the equation and p-value displayed on the lower right corner of each plot.

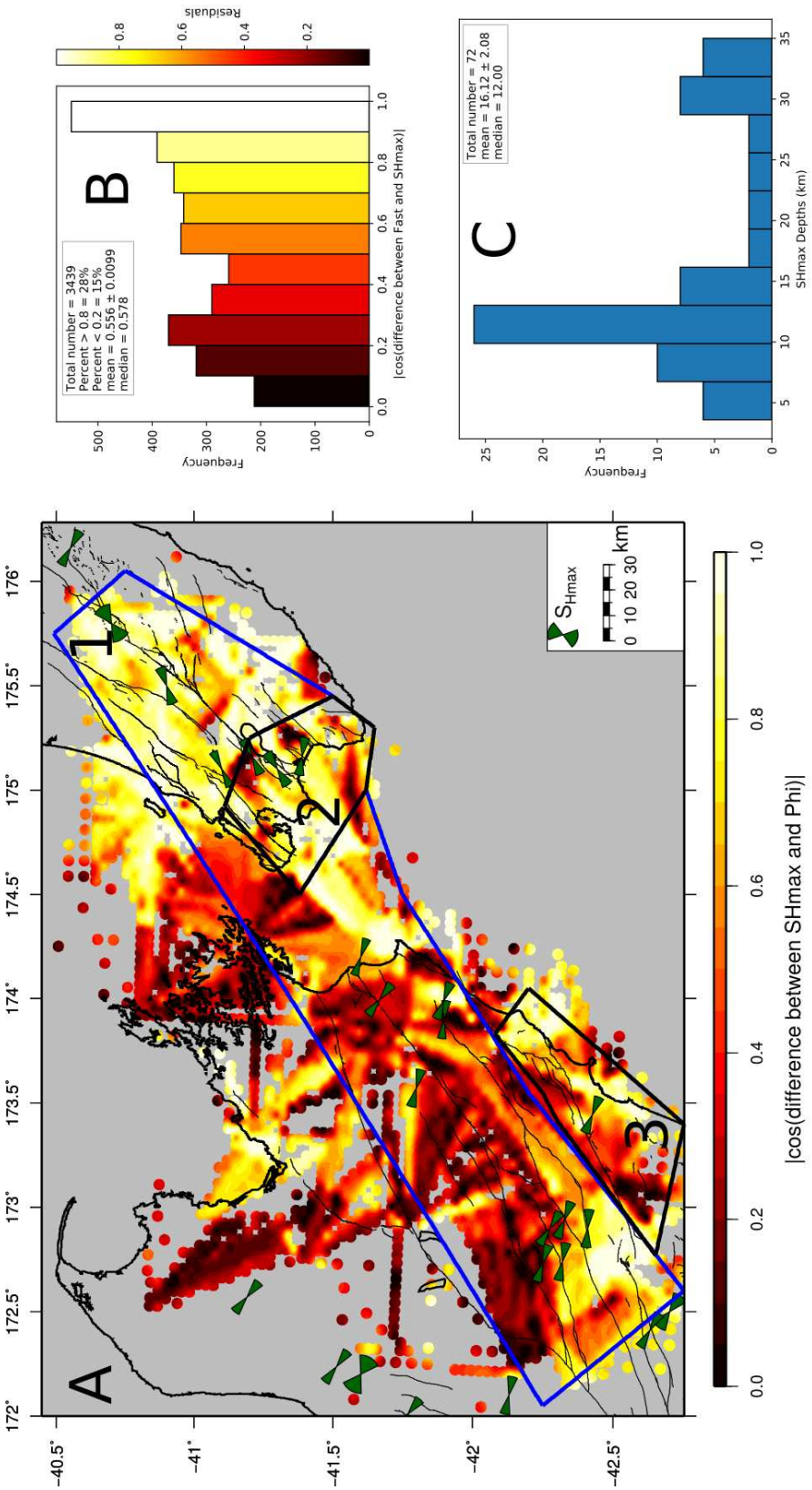

Figure S11. Quantitative comparison between spatially averaged ϕ measurements and the orientation of the closest (<30km) S_{Hmax}. The background colour is a contour of the absolute value of the cosine of the difference between the orientations, coloured by the scale at the bottom. Note that 1 represents no difference between the orientations. The descriptive statistics of the difference between orientations at the closest grid points is displayed on the histogram in B. S_{Hmax} are represented by dark green bow ties. The histogram of the S_{Hmax} depths used for analysis is shown in C.

References

Castellazzi, C., Savage, M., Walsh, E., & Arnold, R. (2015). Shear wave automatic picking and splitting measurements at Ruapehu volcano, New Zealand. *Journal of Geophysical Research: Solid Earth*, *120*, 3363–3384.

Diehl, T., Deichmann, N., Kissling, E., & Husen, S. (2009). Automatic S-Wave Picker for Local Earthquake Tomography. *Bulletin of the Seismological Society of America*, *99*(3), 1906–1920. doi: 10.1785/0120080019

Levin, V., & Park, J. (1997). P-SH conversions in a flat-layered medium with anisotropy of arbitrary orientation. *Geophysical Journal International*, 253–266.